Theory of Linear and Nonlinear Optical Susceptibilities of Semiconductor Quantum Wells

A Thesis Submitted to the

Faculty of Engineering of the University of Glasgow

for the Degree of Doctorate of Philosophy

by

Christine Kelaidis

ProQuest LLC.
789 East Eisenhower Parkway
P.O. Box 1346
Ann Arbor, MI 48106 – 1346

ΑΛΛΑ ΠΡΙΝ ακούσω αγέρα ή μουσική
που κινούσα σε ξάγναντο να βγώ
(μιάν απέραντη κόκκινη άμμο ανέβαινα
με την φτέρνα μου σβήνοντας την Ιστορία)
πάλευα τα σεντόνια Ήταν αυτό που γύρευα
και αθώο και ριγηλό σαν αμπελώνας
και βαθύ και αχάραγο σαν η άλλη όψη τ'ουρανού
Κάτι λίγο γυχής μέσα στην άργιλλο
Και τότε είπε και γεννήθηκεν η θάλασσα
Και είδα και θαύμασα
Και στη μέση της έσπειρε κόσμους μικρούς κατ' εικόνα και ομοίωση μου:
Ίπποι πέτρινοι με τη χαίτη ορθή
και γαλήνιοι αμφορείς
και λοξές δελφινιών ράχες
η Ίος η Σίκινος η Σέριφος η Μήλος
"Κάθε λέξη κι από'να χελιδόνι
γιά να σου φέρνει την άνοιξη μέσα στο θέρος" είπε
Και πολλά τα λιόδεντρα
που να κρησάρουν στά χέρια τους το φώς
κι ελαφρό ν'απλώνεται στον ύπνο σου
και πολλά τα τζιτζίκια
που να μην τα νιώθεις
όπως δεν νιώθεις το σφυγμό στο χέρι σου
αλλά λίγο το νερό
γιά να τό 'χεις Θεό και να κατέχεις τι σημαίνει ο λόγος του
και το δέντρο μονάχο του
χωρίς κοπάδι
γιά να το κάνεις φίλο σου
και να γνωρίζεις τ' ακριβό του τ'όνομα
φτενό στα πόδια σου το χώμα
γιά να μην έχεις που ν'απλώσεις ρίζα
και να τραβάς του βάθους ολοένα
και πλατύς επάνου ο ουρανός
γιά να διαβαζεις μόνος σου την απεραντοσύνη

ΑΥΤΟΣ
ο κόσμος ο μικρός, ο μέγας!

από το ΑΞΙΟΝ ΕΣΤΙ, Η ΓΕΝΕΣΙΣ
ΟΔΥΣΣΕΑ ΕΛΥΤΗ

But before hearing wind or music
as I set out to find a clearing
(ascending an endless red tract of sand
and erasing History with my heel)
I struggled with my bedsheets What I was looking for
was as innocent and tremulous as a vineyard
as deep and unmarked as the sky's other face
And a bit of soul within the clay
Then he spoke and the sea was born
And I saw and marvelled
And in its midst he sowed small worlds in my image and likeness:
Steeds of stone with manes erect
and amphorae serene
and the slanting backs of dolphins
Ios Sikinos Seriphos Mylos
"Every word a swallow
to fetch you spring in the midst of summer," he said
And ample the olive trees
to sift the light through their hands
as it spreads softly over your sleep
and ample the cicadas
that you may not feel them
as you do not feel the pulse in your hand
but sparse the water
that you may hold it a God
and understand the meaning of its speech
and alone the tree
without a flock of its own
that you may take it for friend
and know its precious name
sparse the earth beneath your feet
that you may have nowhere to spread root
but must reach for depth continually
and broad the sky above
that you may read the infinite yourself

THIS
small, this great world!

from AXION ESTI, GENESIS
by ODYSSEUS ELYTIS

Acknowledgements

Above all I would like to express my appreciation to the University of Glasgow for giving me the opportunity to work on this project.

I would like to thank my supervisor Prof. J.M. Arnold for without his continuous reassurance I wouldn't have managed to complete this thesis. His guidance and support were invaluable to me. I am also grateful to Dr. D.C. Hutchings for his useful advice and numerous discussions. I would also like to thank the lecturers of the Optoelectronic Group, my colleagues, technicians and secretaries of the Department of Electronics and Electrical Engineering.

Last, but not least, I would like to thank my family; my parents, Petros and Maria, my brother, Nicos, my grandparents, Nicos, Natalia, Stelios and Christina and my fiancee, Andreas for their support and for bearing with me throughout these years. Of course I couldn't leave out from this list all my friends in Glasgow for their continuous moral support.

This research was supported from the Science and Engineering Research Council (UK), the University of Glasgow and B.N.R. (UK).

Abstract

In this thesis the optical properties of semiconductor quantum well structures suitable for optical integration, particularly those based on the GaAs/GaAlAs material system, are studied. The linear optical properties due to interband transitions, absorption and refractive index change, of semiconductor square, disordered and asymmetric step quantum wells are studied theoretically. The model used for the calculations is the density matrix formalism with intraband relaxation taken into account. The electronic properties of the different quantum well structures are obtained from the envelope function approximation including the valence band mixing model.

The disordering of the quantum well structures results in an increase in the bandgap and is accompanied by changes in the optical properties. This effect is studied for the different models that describe the disordered potential profile, the error function and the hyperbolic secant function. The effect of the profile on the optical properties is evaluated. In addition to the linear optical properties, the second-order nonlinear susceptibility of asymmetric two-step GaAlAs quantum wells is investigated. It is demonstrated that a large $\chi_{zzz}^{(2)}$ (d_{33}) second-order susceptibility tensor exists, suitable for applications that employ the cascading second-order nonlinear effect.

Contents

1 Introduction

1.1 General

Semiconductor materials have been extensively investigated because of their optical and optoelectronic properties. With the development of sophisticated growth techniques for layered semiconductor structures a variety of devices have been developed. The ability to fabricate single and multiple quantum wells further enhanced the semiconductor material properties, but also provoked new optical devices as well as new physical phenomena [1]. A quantum well is a thin heterostructure of a low band-gap material (such as GaAs) enclosed between two layers of a high band-gap material (such as AlGaAs). For most of the work in this field the thickness of the low-gap material has been roughly between 30-100Å. Wells this thin display quantum mechanical effects and for this reason they have been named *quantum wells*. It is only natural that there is growing research interest striving to make use of these features in the optical technology applications. The application of quantum wells in semiconductor laser diodes is nowadays well established. Quantum well lasers display superior characteristics such as low threshold current density, low temperature dependence of threshold current, lasing wavelength tunability and excellent dynamic properties [2].

Optical communications currently use optical fibres as the transmission medium and semiconductor diodes for emission and detection. However it is only the transmission that is carried out in the optical domain. Any modulation, signal processing or switching is done electronically. With the increasing communication requirements it is increasingly more difficult to achieve the required modulation bandwidths. The way forward is expected to be optical integration. Integrated optics intend to do as much signal processing as possible directly on the optical signal itself. For this purpose a family of optical and electro-optical elements, suitable for switching and routing, which allow the assembly of a number of devices on a single substrate, have been proposed. These devices take advantage of the *linear and nonlinear* optical and electro-optical properties of various materials.

Semiconductor heterostructures, like GaAlAs/GaAs and InGaAsP/InP, are key materials in optical communication systems and favourable for future integration since for these materials high quality sophisticated laser structures already exist. Optical semiconductor integrated circuits are divided into *optoelectronic integrated circuits*, which integrate optical and electronic devices and *photonic integrated circuits* which integrate optical devices and components. Integrating optical and electronic devices yields new possibilities, like signal processing in addition to electric/light conversion. Integrating optical devices and components improves their performance considerably, apart from enabling the mass-production of small, highly reliable, low cost devices [3].

Speed and low switching power are the requirements for efficient optical signal processing devices. However, until now, it has been proved to be difficult to find materials that combine high enough nonlinearities (n_2) and low enough losses (α) to make picosecond all-optical switching devices [4]. A lot of effort has been concentrated in improving the nonlinear properties of the different materials and proposing new geometries that enhance the performance of the switching devices. Moreover the integration of semiconductor

nonlinear devices with semiconductor lasers will provide the nonlinear material with high power densities needed for fast and efficient operation.

The introduction of these devices into real systems is moving very slowly because of the difficulties being encountered in integrating optical devices into a complete system. The new semiconductor material structures that will efficiently overcome this problem are subject of intense research activity. Modelling is very useful in this context. The fabrication of elaborate devices is very costly and time consuming. Therefore in order to avoid working on the basis of experimental trial and error and in order to be able to predict new material properties it is preferable to use modelling tools, as far as possible, to make the best possible design. The optical properties of a semiconductor heterostructure are not easily understood by intuition and are not easily predicted quantitatively. Even simple structures cannot be described by simple formulae. There is a large variety of models available to analyse material structures. With the trend towards more complicated structures there is a need for simpler and more accurate models that can be used to predict the material performance.

1.2 Synopsis and objective of the thesis

The linear optical properties that characterise the device performance are the absorption (or gain) coefficient and the refractive index. In particular knowledge of the dispersion of the index of refraction is of significant importance in designing optoelectronic devices. Furthermore for the design of nonlinear devices, like modulators and switches, the nonlinear optical properties of the materials must be studied. The objective of the thesis is the calculation of the linear and second-order nonlinear optical properties of different semiconductor quantum well structures that are being actively investigated for possible future application in integrated optics.

In order to calculate the optical properties of semiconductor quantum well structures, the electronic dispersion relations of these structures have to be determined accurately. This problem is dealt with in Chapter 2. The method used for the band structure calculations of semiconductor heterostructures is the *envelope function approximation*, which is applied to different single GaAs/GaAlAs quantum wells. In Chapter 3 the interaction of light with matter is studied. This interaction can be expressed with the susceptibility tensors $\chi^{(n)}$. The first-order susceptibility tensor $\chi^{(1)}$ of a material is associated with the absorption coefficient and refractive index, while the higher order tensors describe the different nonlinear optical properties of the material. In this chapter expressions of the susceptibilities and in particular those of the first and second-order, are derived from the density matrix formalism. These expressions are used to calculate the linear optical properties of semiconductor square GaAs/GaAlAs quantum wells.

Chapter 4 concentrates on different quantum well structures, the *disordered quantum wells*. These structures have been investigated because of their potential applications in integrated optics. Different models that can be used to approximate the disordering process are presented and the band structure and the linear optical properties of the disordered quantum wells are calculated. Chapter 5 concentrates on asymmetric quantum wells. The advantages of these structures arise from the possibility of obtaining large second order nonlinearities $\chi^{(2)}$ by removing the inversion symmetry of square quantum wells. These large nonlinearities can be used in order to obtain nonlinear phase shifts with the consecutive application of $\chi^{(2)}(\omega,\omega):\chi^{(2)}(-\omega,2\omega)$. This process has been termed *cascaded* and can be used for nonlinear all-optical switching devices. Finally Chapter 6 reviews the results obtained from the previous chapters and suggests further improvements in the computations of the optical properties of semiconductor quantum well structures, for future research work.

References

[1] T.H. Wood, *Multiple quantum well (MQW) modulators*, in *Waveguide Optoelectronics*, edited by J.H. Marsh and R.M. De la Rue, NATO ASI Series, (Kluwer Academic Publishers, 1992), pp. 171-184

[2] Y. Arakawa and A. Yariv, *Quantum well lasers - Gain, spectra, dynamics*, IEEE J. of Quant. Elec., vol. **22**, pp. 1887-1899, 1986

[3] K. Wakao, *Optoelectronic and photonic integrated circuits*, in *Waveguide Optoelectronics*, edited by J.H. Marsh and R.M. De la Rue, NATO ASI Series, (Kluwer Academic Publishers, 1992), pp. 205-223

[4] Y. Silberberg and P.W. Smith, in *Nonlinear Photonics*, Vol.30 of *Springer Series in Electronics and Photonics*, edited by H.M. Gibbs, G. Khitrova, and N. Peyghambarian (Springer-Verlag, 1990) Chapter 6

2 Band Structure of Semiconductor Quantum Wells

2.1 Introduction

One of the major advances in the understanding of the physical properties of crystalline solids has been the development of techniques for the calculation of the allowed energy bands for electrons in crystals. The refinement of these energy band calculations and their extension to describe new materials, like the semiconductor quantum well, is being actively pursued. All of the methods available include individual approximations and each one has its own complications, since the large number of interacting particles which together compose a crystal forbids exact solutions. Two basic assumptions characterise most calculations of energy bands in real crystals; (i) a real crystal can be represented by a perfect periodic structure, (ii) each electron can be regarded as moving independently in a static potential field which takes into account its average interaction with the rest of the crystal. It is generally simpler to consider the implications of the crystal symmetry, rather than the actual precise details of a crystal potential. Semi-empirical schemes, employing known experimental quantities are also particularly appealing. Several well-known methods are available, the tight-binding method [1]-[3], the pseudopotential method [4]-[6] semi-empirical pseudopotential method and the $\mathbf{k}\cdot\mathbf{p}$ method [7]-[11].

These methods have been successfully used for the band calculation of semiconductor heterostructures. The tight-binding and the pseudopotential method are microscopic approaches and consequently have the advantage of being able to handle any heterostructure close or far from the high-symmetry points of the Brillouin zone. The method used in this thesis for the calculation of the energy band structure of semiconductor quantum wells is the *envelope function approximation* [12]-[18]. It is the expansion of the **k·p** method for the case of heterostructure materials and it is mainly restricted in the vicinity of the high-symmetry points of the Brillouin zone. This method uses knowledge of the band structure at one or more values of **k** to obtain a reasonable description of conduction and valence subbands near a specific high-symmetry point. It is an extremely powerful method and easy to apply and often leads to analytical results. In addition it is particularly suited to include external perturbations, like uniaxial stress, external fields (electric, magnetic), the Coulomb potential of impurities, exciton interactions etc. [19].

2.2 Crystalline and electronic properties of GaAs and GaAlAs semiconductors

A periodic potential gives rise to bands and allowed and forbidden energies for electrons in a solid. The exact form of the energy bands depends in some detail on the actual three-dimensional crystal structure. The III-V semiconductor compounds crystallise in the zinc-blende structure. This lattice consists of two interpenetrating face-centre cubic (f.c.c.) lattices, displaced from one another by a fourth of one of the cubic main diagonals (figure 2.1). The reciprocal lattice of a f.c.c. is a body centre cubic lattice. The first Brillouin zone is a truncated octahedron, with several high symmetry points or lines, the Γ, X or L points (figure 2.2).

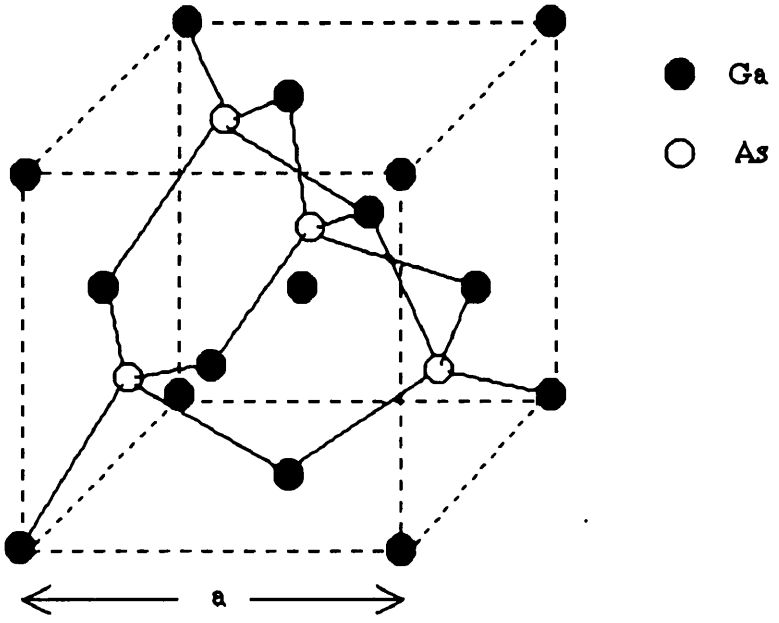

Figure 2.1. Crystal structure for GaAs, zinc-blende lattice (two interpenetrating face centred cubic lattices built by two different types of atoms).

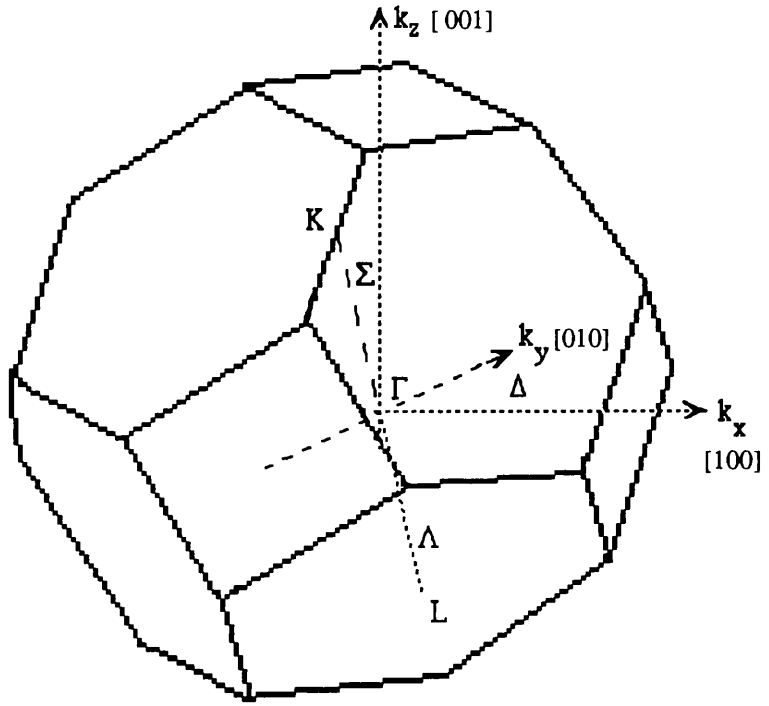

Figure 2.2. First Brillouin zone of the face centred cubic lattice.

In both elemental semiconductors and alloy semiconductors the binding is primarily covalent and each of the atoms has four nearest neighbours. The alloy zinc-blende structure displays the sp^3 hybrid bond orbitals which form tetrahedral bonds to the four nearest neighbour atoms. The 8 outer electrons per unit cell, which contribute to the chemical bonds, determine the semiconductor optical properties near the bandgap. In all the III-V materials the centre of the valence band occurs at the centre of the Brillouin zone (Γ point). In the absence of spin-orbit coupling the three valence bands which originate from the p orbitals are degenerate at Γ. The spin-orbit coupling lifts this sixfold degeneracy and gives rise to a quadruplet which corresponds to angular momentum J=3/2 and a doublet which corresponds to J=1/2. The conduction band edge is found either at the Γ point or near the L or the X point.

From the point of view of the electronic structure the ternary or quaternary solid solutions between III-V or II-VI binary compounds are not crystalline because the potential energy felt by the electrons has no translational symmetry due to the random distribution of the atoms at the sites of the zinc-blende lattice. However in many cases one may use the virtual crystal approximation to describe the alloy electronic states. In such a model the actual aperiodic potential is replaced by an average one which is assumed periodical. Using this procedure the translation invariance can be restored.

In order to determine the energy band structure of different semiconductor quantum wells the first step is to set the equations that describe the energy states of bulk semiconductors using the $\mathbf{k}\cdot\mathbf{p}$ method. The next step is to expand the method in order to incorporate semiconductor heterostructures in the envelope function approximation. In the following sections the envelope function approximation will be presented, following the treatment of References [15] and [17].

2.3 Electronic dispersion relations in the vicinity of the zone centre: $k \cdot p$ analysis

The one-electron Schrödinger equation of a crystal in the presence of some additional potential can be written as,

$$\left[\frac{p^2}{2m_o} + V_{per}(\mathbf{r}) + U(\mathbf{r}) + \frac{\hbar}{4m_o{}^2c^2}(\sigma \times \nabla V)\cdot \mathbf{p} + \delta H_r\right]\psi(\mathbf{r}) = E\psi(\mathbf{r}) \tag{2.1}$$

where m_o is the free electron mass, $V_{per}(\mathbf{r})$ is the periodic crystalline potential, $U(\mathbf{r})$ is any additional potential and the last two terms in the equation are relativistic corrections. The forth term is the spin orbit coupling term, where σ is the electron spin. The last term is only important in heavy atoms and we will not consider it in our analysis for simplicity.

If the additional potential is vanishing, $U(\mathbf{r})=0$, it is well known that the solution to the equation, for the eigenfunctions $\psi(\mathbf{r})$, are the Bloch functions $\psi_{n\mathbf{k}}(\mathbf{r})$ [20],

$$\psi_{n\mathbf{k}}(\mathbf{r}) = \Omega^{-1/2}\, e^{i\mathbf{k}\cdot\mathbf{r}}\, u_{n\mathbf{k}}(\mathbf{r}) \tag{2.2}$$

where the Bloch function is normalised over the whole crystal with volume Ω, $u_{n\mathbf{k}}(\mathbf{r})$ has the period of the crystal lattice and is normalised over the volume of a unit cell Ω_o ($\Omega = N\Omega_o$, N number of unit cells). The $\mathbf{k}$ vector is restricted in the first Brillouin zone. The dispersion relations for a small range of $\mathbf{k}$ around the band extrema, are calculated from the $\mathbf{k}\cdot\mathbf{p}$ method. The periodic parts of the Bloch functions are solutions of,

$$\left[\frac{p^2}{2m_o}+V_{per}(\mathbf{r})+\frac{\hbar}{4m_o{}^2c^2}(\sigma\times\nabla V)\cdot\mathbf{p}+\frac{\hbar^2k^2}{2m_o}+\right.$$
$$\left.+\frac{\hbar\mathbf{k}}{m_0}\left(\mathbf{p}+\frac{\hbar}{4m_oc^2}\sigma\times\nabla V\right)\right]u_{nk}=E_{nk}u_{nk}$$

(2.3)

obtained from (2.1) and (2.2). Equation (2.3) can be rewritten,

$$[H(\mathbf{k}=0)+W(\mathbf{k})]\,u_{nk}=E_{nk}u_{nk}$$

(2.4)

where $H(\mathbf{k}=0)$ is the crystal Hamiltonian at the symmetry point Γ ($\mathbf{k}=0$), whose eigenfunctions are ψ_{n0}, or equivalently u_{n0} and eigenvalues E_{n0}. The $\mathbf{k}$-dependent operator $W(\mathbf{k})$ vanishes at $\mathbf{k}=0$ and so the set of u_{n0} can be used as a basis for a representation. Group theory gives the symmetry properties of the functions u_{n0}. The functions corresponding to the conduction band are singly degenerate (doubly counting spin) and are denoted by $S\uparrow$ and $S\downarrow$. The symbol $\uparrow$ and $\downarrow$ means spin up and spin down respectively. The label S refers to the fact that the functions have the symmetry properties of the s functions under the operations of the tetrahedral group. The valence band functions are triply degenerate (sixfold with spin) and are denoted by $X\uparrow$, $Y\uparrow$, $Z\uparrow$, $X\downarrow$, $Y\downarrow$, $Z\downarrow$. The notation indicates that the functions have the symmetry properties of the atomic p-functions x, y, z under the operation of the tetrahedral group [10]. Therefore the periodic part of the Bloch function can be expressed as,

$$u_{nk}=\sum_m c_m(\mathbf{k})u_{m0}$$

(2.5)

By inserting equation (2.5) into equation (2.4), multiplying by u_{m0}^* and integrating over a unit cell the following expression can be obtained,

$$\sum_m \left\{ \left(E_{n0} - E_{nk} + \frac{\hbar^2 k^2}{2m_o} \right) \delta_{nm} + \frac{\hbar \mathbf{k}}{m_o} \langle n\mathbf{0}|\mathbf{p} + \frac{\hbar}{4m_o c^2}(\sigma \times \nabla V)|m\mathbf{0}\rangle \right\} c_m(\mathbf{k}) = 0 \tag{2.6}$$

where

$$\langle n\mathbf{0}|A|m\mathbf{0}\rangle = A_{nm} = \int_{\text{unit cell}} u_{n0}^* A u_{m0} d^3r \tag{2.7}$$

Equation (2.6) gives a complete description of energy bands throughout **k**-space in terms of the energies E_{n0} and the momentum matrix π, where π is defined as,

$$\pi = \mathbf{p} + \frac{\hbar}{4m_o c^2}(\sigma \times \nabla V) \tag{2.8}$$

Consider the case that the n^{th} band edge (energy E_{n0}) is non-degenerate and **k** is close to the minimum **k**=0 so that W(**k**) can be regarded as a perturbation. Non-degenerate bands can always be treated this way while sufficiently close to a minimum. After some mathematical calculations a second order correction to the energy E_{n0} can be obtained,

$$E_{nk} = E_{n0} + \frac{\hbar^2 k^2}{2m_o} + \frac{\hbar^2}{m_o{}^2} \sum_{m \neq n} \frac{|\mathbf{k} \cdot \pi_{nm}|^2}{E_{n0} - E_{m0}} \tag{2.9}$$

as well as a second order correction to the Bloch functions $u_{n0}(\mathbf{r})$,

$$u_{nk}(\mathbf{r}) = u_{n0}(\mathbf{r}) + \sum_{m \neq n} \frac{\mathbf{k} \cdot \pi_{nm}}{m_o[E_{n0} - E_{m0}]} u_{m0}(\mathbf{r}) \tag{2.10}$$

As long as E_{nk}–E_{n0} remains much smaller than all the band edge gaps (E_{n0}–E_{m0}) the dispersion relations of the non-degenerate bands are parabolic in **k** in the vicinity of the Γ point. Expression (2.9) can be rewritten as,

$$E_{nk} = E_{n0} + \frac{\hbar^2}{2}\sum_{\alpha\beta} k_\alpha \frac{1}{\mu_n^{\alpha\beta}} k_\beta \; ; \quad \alpha,\beta = x,y,z$$

(2.11)

where $\mu_n{}^{\alpha\beta}$ is the effective mass tensor which describes the carrier kinematics in the vicinity of the zone centre for energy close to the n^{th} band edge and is equal to,

$$\frac{1}{\mu_n^{\alpha\beta}} = \frac{1}{m_o}\delta_{\alpha\beta} + \frac{2}{m_o^2}\sum_{m\neq n} \frac{\pi_{mn}^{\alpha}\pi_{nm}^{\beta}}{E_{n0} - E_{m0}}$$

(2.12)

In many circumstances the spin-orbit coupling can be discarded from the calculations. In this case the term $\frac{\hbar}{4m_oc^2}(\sigma \times \nabla V)$ is assumed to be negligible and is set to zero. In this case the perturbation method is exactly the same and the results can be obtained by substituting π by **p**.

2.3.1 Beyond the quadratic dispersion relations: the Kane model

We have described the **k·p** approximation with the assumption that there is no band degeneracy or coupling between the bands. This assumption is violated for systems of interest. For all the cubic semiconductors it is known that there is a band degeneracy at the Γ point of the valence band in addition to coupling between the bands and in this case the theory must be modified to account for these effects. Since spin-orbit coupling is non-zero in III-V compounds, it is desirable to have a basis at **k**=0 in which the relevant term is diagonal. This can be achieved by forming a linear combination of the 8 Bloch functions described earlier, such that the total angular momentum **J**=**L**+σ and its projection J_z along the z-axis are diagonal in this new basis. For the S edge the addition of L=0 to σ=1/2 gives J=1/2 (Γ_6 symmetry). For the P edges adding L=1 to σ=1/2 gives either J=1/2 or J=3/2. In III-V the quadruplet J=3/2, that corresponds to the Γ_8 symmetry, is always higher than the

doublet J=1/2, that corresponds to the Γ_7 symmetry. Their energy separation is noted Δ (figure 2.3). The basis wavefunctions of the Γ_6, Γ_7 and Γ_8 edges are presented in Table 2.1.

TABLE 2.1. Γ_6, Γ_7, Γ_8 PERIODIC PART OF THE BLOCH FUNCTIONS

u_i	$\lvert J,m_J\rangle$	Ψ_{J,m_j}	$E_i(k=0)$
u_1	$\lvert\frac{1}{2},\frac{1}{2}\rangle$	$i\lvert S\uparrow\rangle$	0
u_3	$\lvert\frac{3}{2},\frac{1}{2}\rangle$	$-\sqrt{\frac{2}{3}}\lvert Z\uparrow\rangle+\frac{1}{\sqrt{6}}\lvert(X+iY)\downarrow\rangle$	$-E_o$
u_5	$\lvert\frac{3}{2},\frac{3}{2}\rangle$	$\frac{1}{\sqrt{2}}\lvert(X+iY)\uparrow\rangle$	$-E_o$
u_7	$\lvert\frac{1}{2},\frac{1}{2}\rangle$	$\frac{1}{\sqrt{3}}\lvert(X+iY)\downarrow\rangle+\frac{1}{\sqrt{3}}\lvert Z\uparrow\rangle$	$-E_o-\Delta$
u_2	$\lvert\frac{1}{2},-\frac{1}{2}\rangle$	$i\lvert S\downarrow\rangle$	0
u_4	$\lvert\frac{3}{2},-\frac{1}{2}\rangle$	$-\frac{1}{\sqrt{6}}\lvert(X-iY)\uparrow\rangle-\sqrt{\frac{2}{3}}\lvert Z\downarrow\rangle$	$-E_o$
u_6	$\lvert\frac{3}{2},-\frac{3}{2}\rangle$	$\frac{1}{\sqrt{2}}\lvert(X-iY)\downarrow\rangle$	$-E_o$
u_8	$\lvert\frac{1}{2},-\frac{1}{2}\rangle$	$-\frac{1}{\sqrt{3}}\lvert(X-iY)\uparrow\rangle+\frac{1}{\sqrt{3}}\lvert Z\downarrow\rangle$	$-E_o-\Delta$

Each edge is twice degenerate and corresponds to the two opposite values of m_J which are eigenvalues of J. Taking the matrix elements of $W(\mathbf{k})$ between these 8 Bloch functions and setting, $E_0 = E_{\Gamma 6}-E_{\Gamma 8}$, $\Delta = E_{\Gamma 8}-E_{\Gamma 7}$, $k_\pm = \frac{1}{\sqrt{2}}(k_x \pm k_y)$ and

$$P = \frac{-i\hbar}{m_o}\langle S|p_x|X\rangle = \frac{-i\hbar}{m_o}\langle S|p_y|Y\rangle = \frac{-i\hbar}{m_o}\langle S|p_z|Z\rangle \tag{2.13}$$

the interband matrix element of the velocity operator, then the energies $E_{n\mathbf{k}}$ are the eigenvalues of the following 8×8 matrix,

	$\left\|iS\uparrow\right\rangle$	$\left\|\frac{3}{2},\frac{1}{2}\right\rangle$	$\left\|\frac{3}{2},\frac{3}{2}\right\rangle$	$\left\|\frac{1}{2},\frac{1}{2}\right\rangle$	$\left\|iS\downarrow\right\rangle$	$\left\|\frac{3}{2},-\frac{1}{2}\right\rangle$	$\left\|\frac{3}{2},-\frac{3}{2}\right\rangle$	$\left\|\frac{1}{2},-\frac{1}{2}\right\rangle$
$\left\langle iS\uparrow\right\|$	$\frac{\hbar^2k^2}{2m_o}$	$-\sqrt{\frac{2}{3}}Pk_z$	Pk_+	$\frac{1}{\sqrt{3}}Pk_z$	0	$-\frac{1}{\sqrt{3}}Pk_-$	0	$-\sqrt{\frac{2}{3}}Pk_-$
$\left\langle\frac{3}{2},\frac{1}{2}\right\|$	$-\sqrt{\frac{2}{3}}Pk_z$	$-E_0+\frac{\hbar^2k^2}{2m_o}$	0	0	$\frac{1}{\sqrt{3}}Pk_-$	0	0	0
$\left\langle\frac{3}{2},\frac{3}{2}\right\|$	Pk_-	0	$-E_0+\frac{\hbar^2k^2}{2m_o}$	0	0	0	0	0
$\left\langle\frac{1}{2},\frac{1}{2}\right\|$	$\frac{1}{\sqrt{3}}Pk_z$	0	0	$-E_0-\Delta+\frac{\hbar^2k^2}{2m_o}$	$\sqrt{\frac{2}{3}}Pk_-$	0	0	0
$\left\langle iS\downarrow\right\|$	0	$\frac{1}{\sqrt{3}}Pk_+$	0	$\sqrt{\frac{2}{3}}Pk_+$	$\frac{\hbar^2k^2}{2m_o}$	$-\sqrt{\frac{2}{3}}Pk_z$	Pk_-	$\frac{1}{\sqrt{3}}Pk_z$
$\left\langle\frac{3}{2},-\frac{1}{2}\right\|$	$-\frac{1}{\sqrt{3}}Pk_+$	0	0	0	$-\sqrt{\frac{2}{3}}Pk_z$	$-E_0+\frac{\hbar^2k^2}{2m_o}$	0	0
$\left\langle\frac{3}{2},-\frac{3}{2}\right\|$	0	0	0	0	Pk_+	0	$-E_0+\frac{\hbar^2k^2}{2m_o}$	0
$\left\langle\frac{1}{2},-\frac{1}{2}\right\|$	$-\sqrt{\frac{2}{3}}Pk_+$	0	0	0	$\frac{1}{\sqrt{3}}Pk_z$	0	0	$-E_0-\Delta+\frac{\hbar^2k^2}{2m_o}$

(2.14)

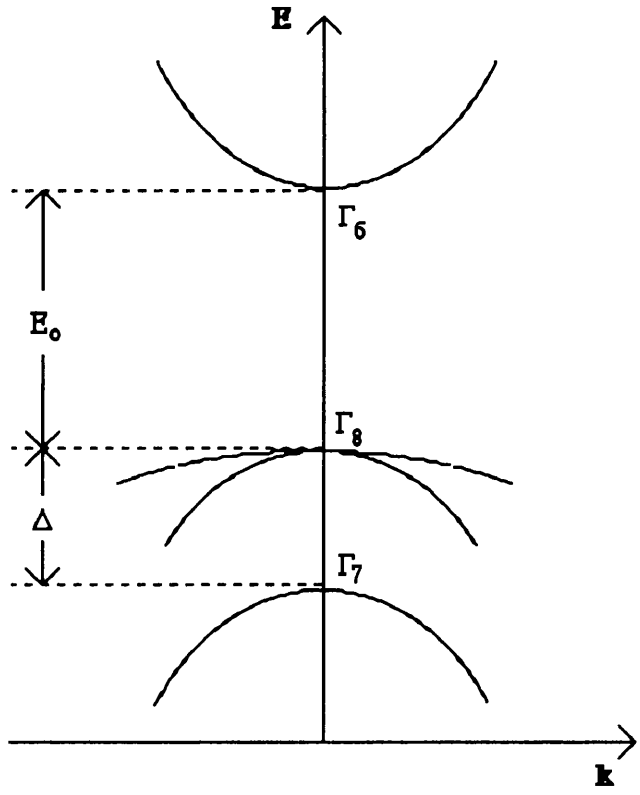

Figure 2.3. Band structure of a direct gap III-V in the vicinity of the zone centre of the Brillouin zone. Only the states Γ_6, Γ_7, Γ_8 for a perfect crystal are presented.

2.3.2 Motion of electrons and holes in slowly varying fields

Up to now we have concentrated on the energy spectra of perfect III-V compounds. When the crystal is imperfect the energy bands are solutions of the Schrödinger equation (2.1) with the potential $U(\mathbf{r})$ not vanishing. These solutions can be obtained by generalising the $\mathbf{k}\cdot\mathbf{p}$ approximation. For this case the solutions of (2.1) can be expanded in the form [17]:

$$\psi(\mathbf{r}) = \sum_{i=1}^{8} c_i f_i(\mathbf{r}) u_{i0}(\mathbf{r}) \tag{2.15}$$

where u_{i0}'s are the Γ point Bloch functions for the 8 band edges given in Table 2.1. The function $f_i(\mathbf{r})$ has a very important meaning, it is called the *envelope function* because it is a slow varying function on the scale of the unit cell Ω_0 that modulates the rapidly varying

Bloch part $u_{i0}(\mathbf{r})$. From expression (2.1), making use of (2.15), the following expression can be obtained,

$$\int_{\Omega} f_m^*(r)\, d^3r \sum_{i=0}^{8} c_i \left\{ \delta_{im} \left[E_i - E + \frac{p^2}{2m_o} + U(\mathbf{r}) \right] + \mathbf{p}_{mi} \cdot \mathbf{p} \right\} f_i(\mathbf{r}) = 0 \tag{2.16}$$

where,

$$\mathbf{p}_{mi} = \frac{1}{m_o \Omega_o} \int_{\Omega_o} u_{m0}^* \, \mathbf{p} \, u_{i0} d^3r \tag{2.17}$$

It is worth noting that the u_{i0}'s do not appear explicitly in the coupled system, but are contained into the matrix elements $\mathbf{p}_{mi}$. Equation (2.16) can be rewritten as

$$\langle \mathbf{f} | \, B + \{U(\mathbf{r}) - E\}\mathbf{I} \, | \mathbf{f} \rangle = 0 \tag{2.18}$$

where $| \mathbf{f} >$ is an (8×1) column vector, B is an (8×8) matrix and $\mathbf{I}$ is the (8×8) identity matrix. Non vanishing solutions exist if $\mathbf{f}$ is the eigensolution of,

$$[B + U(\mathbf{r})]\, \mathbf{f} = E\, \mathbf{I}\, \mathbf{f} \tag{2.19}$$

The differential operator B is simply the (8×8) matrix of equation (2.14) where $\hbar\mathbf{k}$ has been replaced by the differential operator $\mathbf{p}=-i\hbar\nabla$. For perfect crystals, with $U(\mathbf{r})=0$, it is always possible to obtain eigenstates of B which are also eigenstates of J_z and therefore do not display $S\uparrow$ and $S\downarrow$ mixing. For the envelope functions of the perturbed crystal it is in general impossible to achieve a simultaneous diagonalisation of $B+U(\mathbf{r})$ and J_z. Therefore the eigenstates of a perturbed semiconductor are in general a mixture of different m_J's.

2.4 Electronic states of semiconductor heterostructures

In the previous section the model of calculating the eigenstates of bulk III-V material in the vicinity of the zone centre with a slowly varying perturbing field was described. In this section the model will be put to use for the determination of the eigenstates of the semiconductor heterostructures and in particular for the semiconductor quantum wells. The development of the Kane model in bulk semiconductors to include heterostructures is widely named *envelope function approximation*. In this method the wave functions of the quantum wells are expanded with respect to the wave functions of both elemental materials around a symmetry point $\mathbf{k}_0$, like the $\mathbf{k}=0$ point. The allowed energy levels are obtained by matching the linear combinations of all allowed propagating and evanescent bulk states of the different layers at the interfaces and by imposing boundary conditions at infinity.

Consider a semiconductor quantum well (type I-figure 2.4) with growth direction along the z-axis and host materials W and B that are binary or ternary III-V (the method is valid also for II-VI). The B material is barrier-acting while the W material is well-acting. Each of the host materials has its own lattice constant, a band structure with dispersion relations $E_n^{(w)}(\mathbf{k}_w)$, $E_n^{(b)}(\mathbf{k}_b)$ and periodic part of the Bloch functions $u_{n\mathbf{k}_w}^{(w)}(\mathbf{r})$, $u_{n\mathbf{k}_b}^{(b)}(\mathbf{r})$. In the envelope function framework the W and B materials that compose the heterostructure are assumed to be perfectly lattice matched and crystallise with the same crystallographic structure. This approximation is relatively well justified for GaAs-GaAlAs semiconductor materials.

In the envelope function approximation the similarity found between the Kane matrix elements of the various III-V compounds that make up the B and W materials is exploited and certain important assumptions are made;

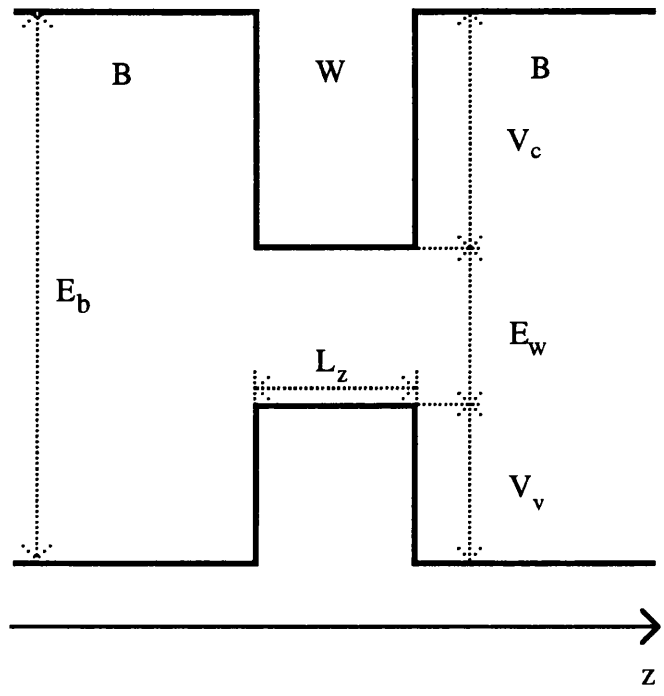

Figure 2.4. Band edge profile for a type I quantum well.

i) The electronic states of the heterostructures are often close to the band extrema of the hosts. Therefore only a small fraction of the Brillouin zone participates in the building of the heterostructure states. The wavefunctions inside each layer B and W are expanded with respect to the periodic parts of the Bloch functions of the edges under consideration,

$$\psi(\mathbf{r}) = \sum_i f_i^{(w)}(\mathbf{r}) u_{i,\mathbf{k}_w}^{(w)}(\mathbf{r}), \text{ if } \mathbf{r} \text{ corresponds to a W layer} \tag{2.20a}$$

$$\psi(\mathbf{r}) = \sum_i f_i^{(b)}(\mathbf{r}) u_{i,\mathbf{k}_b}^{(b)}(\mathbf{r}), \text{ if } \mathbf{r} \text{ corresponds to a B layer} \tag{2.20b}$$

where the wave vectors $\mathbf{k}_w$ and $\mathbf{k}_b$ are close to the same $\mathbf{k}_0$ point of the Brillouin zone around which the heterostructures are built. The summation over i runs over the edges included in the analysis.

ii) Most of the host materials display similar band structures. Furthermore the periodic part of the Bloch functions of the relevant band edges do not differ very much from one host material to the other and so it is fair to assume that,

$$u_{i,\mathbf{k}_o}^{(w)}(\mathbf{r}) \equiv u_{i,\mathbf{k}_o}^{(b)}(\mathbf{r}) \tag{2.21}$$

This assumption also implies that the interband matrix element $\langle S|p_x|X\rangle$, given in expression (2.13), is the same in the W and B layers.

Since the lattice constants of the host materials are assumed to be the same, the heterostructure becomes translationally invariant in each layer plane. Therefore the envelope functions can be factorised,

$$f_i^{(w)}(\mathbf{r}_{||}, z) = \frac{1}{\sqrt{S}} e^{i\mathbf{k}_{||}\cdot\mathbf{r}_{||}} \phi_i^{(w)}(z) \tag{2.22a}$$

$$f_i^{(b)}(\mathbf{r}_{||}, z) = \frac{1}{\sqrt{S}} e^{i\mathbf{k}_{||}\cdot\mathbf{r}_{||}} \phi_i^{(b)}(z) \tag{2.22b}$$

or in short,

$$f_i(\mathbf{r}_{||}, z) = \frac{1}{\sqrt{S}} e^{i\mathbf{k}_{||}\cdot\mathbf{r}_{||}} \phi_i(z) \tag{2.22c}$$

where S is the sample area, $\mathbf{k}_{||}=(k_x,k_y)$ is a bi-dimensional wave vector which is the same in the W and B layers in order to agree with the in-plane translational invariance and $\mathbf{r}_{||}=(r_x,r_y)$.

The problem of calculating of the eigenstates of the semiconductor heterostructures will be treated similarly to the Kane model described in the previous section, in the same way

Luttinger and Kohn treated the many bands effective mass equation for acceptor impurities [8]-[9]. In this model the bulk Hamiltonian in each host layer can be rewritten in the form of an 8×8 matrix,

$$H_{ij}(\mathbf{k}) = \sum_{\alpha} \frac{\hbar k_\alpha}{m_o} \langle i|p_\alpha|j\rangle + \sum_{\alpha,\beta} k_\alpha D_{ij}^{\alpha\beta} k_\beta \tag{2.23}$$

where the summation i,j is over the 8 band edges given in Table 2.1, α,β=x,y,z and

$$D_{ij}^{\alpha\beta} = \frac{\hbar^2}{2m_o}\delta_{ij}\delta_{\alpha\beta} + \frac{\hbar^2}{m_o^2}\sum_{m} \frac{\langle j|p_\alpha|m\rangle\langle m|p_\beta|j\rangle}{\hat{E} - E_m} \tag{2.24}$$

$\hat{E}$ is an average energy of the Γ_6,Γ_7 and Γ_8 edge and the summation m runs over all host band edges, except Γ_6,Γ_7 and Γ_8. Expression (2.23) is similar to (2.14) with the difference that the coupling between the 8 band edges is separated into direct and indirect. The indirect coupling through the remaining band edges is represented by the matrix $D^{\alpha\beta}$. By including a non vanishing potential $U(\mathbf{r})$ in the Hamiltonian (2.23) a system of differential equations can be obtained for the envelope functions $f_i(\mathbf{r})$,

$$\sum_{j=1}^{8}\left[H_{ij}(\mathbf{k}) + U(\mathbf{r})\delta_{ij}\right] f_j(\mathbf{r}) = E f_i(\mathbf{r}) \tag{2.25}$$

In order to apply equation (2.25) to the problem of calculating the eigenstates of the semiconductor heterostructures an important parameter must be considered, the *band-gap discontinuity*. This parameter represents the relative energy positions for the bands of the host materials. Even though the band gaps of the host materials are known, their relative position have not been accurately determined. In principle microscopic calculations should be able to predict this parameter, but the accuracy of these calculations does not exceed a few tenths of an eV. Moreover the experimental published values of the valence band

discontinuity range from 15% to 45% of the band gap because of the uncertainties involved in the experimental procedures. This inaccuracy is not sufficient for most practical purposes, since the hosts' band line-ups sensitively influence the energy levels in a heterostructure. In order to carry through the calculations it will be assumed that the energy offset is known. The 8×8 Hamiltonian of a semiconductor heterostructure can be obtained from expression (2.25) for bulk material;

i) By replacing k_z with $-i\hbar\partial/\partial z$

ii) By considering the parameters appearing in (2.25) position dependent with values in the W and B layer appropriate to the W and B materials.

iii) By adding functions $V_c(z)$, $V_v(z)$ and $V_\delta(z)$ on appropriate diagonal terms. These functions are zero in the B layer and V_c, V_v, V_δ in the W layers, where V_c, V_v, V_δ are the energy shifts of the Γ_6,Γ_8, Γ_7 edges of the W material with respect to the B material.

iv) By properly antisymmetrising any term which involves a product of a z-dependent function with the $\partial/\partial z$ operator

v) In addition if band bending takes place in the heterostructure, each diagonal term includes a contribution -eF(z), where F(z) is an electrostatic potential of external origin, e.g. electric field, or internal origin, e.g. charges [15].

Therefore the eigenvalue problem for a semiconductor heterostructure becomes,

$$\{\mathbf{H}(\gamma_i(z),-i\hbar\partial/\partial z, \mathbf{k}_{||})+V_c(z)\,\mathbf{I}_c+V_v(z)\,\mathbf{I}_{v+}V_\delta(z)\,\mathbf{I}_\delta-eF(z)\mathbf{I}\}\phi(z)=E\phi(z) \tag{2.26}$$

H is the 8×8 differential system involving the bulk effective parameters $\gamma_i(z)$ that describe the coupling between the bands, $\mathbf{I}_c$, $\mathbf{I}_v$, $\mathbf{I}_\delta$ are 2×2, 4×4, 2×2 identity matrices acting on the Γ_6,Γ_8 and Γ_7 edges respectively and **I** is an 8×8 identity matrix. For the solution of the differential system (2.26) *boundary conditions* must be applied to the wavefunctions at the interfaces between the host materials [21].These are;

i) ϕ must be continuous everywhere and in particular across the interfaces.

ii) $\mathbf{M}\phi$ must be continuous across the interfaces, where **M** is an 8×8 matrix obtained by integrating **D** across the interfaces. This boundary condition means that the average of the probability current is constant across the heterointerface.

iii) $\phi_i(z)$ should decay to zero at large z.

2.5 GaAs-$Ga_{1-x}Al_xAs$ quantum well structures

The method of evaluating the dispersion relations of a semiconductor quantum well described in the previous section can be implemented for a GaAs-$Ga_xAl_{1-x}As$ structure. It is important to note that the method is applicable only in systems with x value in the range $0<x<0.4$ [22], since in that range the heterostructure has a direct band gap at the Γ point. For values of x larger then 0.4 the method can be applied only for the valence band.

As already mentioned earlier for many III-V heterostructures the band edges relevant to optical and transport properties gave the Γ_6, Γ_7 and Γ_8 symmetries (figure 2.3). The light and heavy hole bands are degenerate at the Γ_8 point and the Γ_7 split-off band is separated due to spin-orbit coupling from the Γ_8 edge by $\Delta=E_{\Gamma_8}-E_{\Gamma_7}=0.341$ eV for GaAs, while the conduction band has a Γ_6 symmetry. Assuming that Δ is large enough, the summations over the eight bands can be simplified to summations over six bands by discarding the split-off band. A further simplification in the band model is to consider the conduction and the valence bands as being decoupled. This a relatively good approximation for wide-band-gap semiconductors like GaAs. For the conduction band a simple isotropic parabolic band can be used, while the valence band can be described by the 4x4 Luttinger-Kohn Hamiltonian.

2.5.1 Conduction band

The conduction band is decoupled from the valence band. Therefore in the envelope function approximation the conduction band wavefunction can be expressed as,

$$\psi_c^i(\mathbf{r}) = \sum_\eta f_i^\eta(\mathbf{r})\, u_{i0}^\eta(\mathbf{r})$$

$$f_i^\eta(\mathbf{r}) = \frac{1}{\sqrt{S}} e^{i\mathbf{k}_{||}\cdot\mathbf{r}_{||}} \phi_c^i(z)$$

(2.27)

where η denotes sum over spin states. The envelope functions $\phi_i(z)$ must satisfy the effective mass equation,

$$\left[-\frac{\hbar^2}{2m_c(z)}\frac{\partial^2}{\partial z^2} + V_c(z)\right]\phi_c^i(z) = E_c^i\phi_c^i(z)$$

(2.28)

where $m_c(z)$ is the conduction band effective mass, equal to m_{cw} and m_{cb} the effective masses of the conduction band in the W and B layers respectively and $V_c(z)$ is the quantum well potential for the conduction band. Each of the energy levels E_c^i of the i^{th} subband is twice degenerate (Kramers degeneracy). For the calculation of the energy levels the envelope functions must also satisfy the boundary conditions; $\phi_c^i(z)$ and $m_c(z)^{-1}\phi_c^i(z)$ continuous at the interfaces and $\phi_c^i(z)$ decay to zero at infinity. When the effective masses m_{cw} and m_{cb} do not differ substantially the in-plane dispersion relation is nearly parabolic in $\mathbf{k}_{||}$,

$$E_c^i(\mathbf{k}_{||}) = E_c^i(0) + \frac{\hbar^2 k_{||}^2}{2m_{ci}}$$

(2.29)

where the in plane mass m_{ci} of the i^{th} subband in the vicinity of $\mathbf{k}_{||}=0$ is obtained from the expression,

$$\frac{1}{m_{ci}} = \frac{1}{m_{cw}}(1-P_i) + \frac{1}{m_{cb}}P_i \tag{2.30}$$

and P_i is the integrated probability of finding the particle in the n^{th} state in the barrier.

2.5.2 Valence band

Having made the assumption that the Γ_6 conduction subband and the Γ_7 split-off subband are decoupled from the Γ_8 valence subbands, the in-plane dispersion relations of the Γ_8 subbands in GaAs-GaAlAs quantum wells can be described by the 4x4 Luttinger-Kohn Hamiltonian,

$$H_v = \begin{vmatrix} a_+ & c & b & 0 \\ c^* & a_- & 0 & -b \\ b^* & 0 & a_- & c \\ 0 & -b^* & c^* & a_+ \end{vmatrix} \tag{2.31}$$

where,

$$\begin{aligned} a_\pm &= V_v(z) - \frac{1}{2}(\gamma_1 \pm \gamma_2)(k_x^2 + k_y^2) - \frac{1}{2}(\gamma_1 \mp \gamma_2)k_z^2 \\ b &= \sqrt{3}\gamma_3(k_x - ik_y)k_z \\ c &= \sqrt{\frac{3}{2}}\left[\gamma_2(k_x^2 - k_y^2) - 2i\gamma_3 k_x k_y\right] \end{aligned} \tag{2.32}$$

$\gamma_1, \gamma_2, \gamma_3$ are the Luttinger parameters which describe the coupling between Γ_8 and all the hosts' edges including Γ_6. These parameters are position dependent and are related to the inverse zone centre heavy hole and light hole valence subband effective masses through the expressions;

$$\text{in the (001) direction } m_{hh}^* = (\gamma_1 - 2\gamma_2)^{-1}$$
$$m_{lh}^* = (\gamma_1 + 2\gamma_2)^{-1}$$
$$\text{in the (111) direction } m_{hh}^* = (\gamma_1 - 2\gamma_3)^{-1}$$
$$m_{lh}^* = (\gamma_1 + 2\gamma_3)^{-1}$$

(2.33)

For the calculation of the in-plane dispersion relations of the semiconductor quantum well, the three boundary conditions mentioned in the previous section must be applied to the four component envelope-function. The second condition can be expressed for the case of the four subband edges as,

$$\mathbf{M}\phi = \begin{vmatrix} i(\gamma_1 - 2\gamma_2)\frac{\partial}{\partial z} & 0 & \sqrt{3}\gamma_3(k_x - ik_y) & 0 \\ 0 & i(\gamma_1 + 2\gamma_2)\frac{\partial}{\partial z} & 0 & -\sqrt{3}\gamma_3(k_x - ik_y) \\ \sqrt{3}\gamma_3(k_x + ik_y) & 0 & i(\gamma_1 + 2\gamma_2)\frac{\partial}{\partial z} & 0 \\ 0 & -\sqrt{3}\gamma_3(k_x + ik_y) & 0 & i(\gamma_1 - 2\gamma_2)\frac{\partial}{\partial z} \end{vmatrix} \begin{vmatrix} \phi_{hh\uparrow}(z) \\ \phi_{lh\downarrow}(z) \\ \phi_{lh\uparrow}(z) \\ \phi_{hh\downarrow}(z) \end{vmatrix}$$

(2.34)

must be continuous across the interfaces. hh$\uparrow$ and hh$\downarrow$ are the heavy hole states with spin up and down respectively and lh$\uparrow$ and lh$\downarrow$ are the light hole states. At $\mathbf{k}_{||}$=0 the constants b and c given in expression (2.32) are equal to zero and consequently the off-diagonal terms of the Hamiltonian matrix (2.31) are also equal to zero. If these terms were always negligible, the Hamiltonian would split into two independent Ben Daniel-Duke Hamiltonians, one for the heavy holes and one for the light holes. This approximation is called the diagonal approximation.

Due to the band coupling the complexity of the problem of calculating the Γ_8 in-plane dispersion relations is such that analytical solutions cannot be obtained in the general case and must be pursued numerically for both the conduction and the valence bands. Analytical

calculations for the energy levels can be obtained for the conduction band of a square quantum well assuming parabolic band structure [23]. Valence subbands of uniaxially stressed square quantum wells have been found by solving exactly the multiband effective-mass equation for the envelope function [16], but these calculations are known not to be self-consistent. All the analytical calculations to date are restricted to symmetric square quantum wells. For asymmetric quantum wells the energy levels and the dispersion relations have to be sought numerically.

2.5.3 Numerical methods for the calculation of the band structure of semiconductor quantum wells

In order to calculate the energy levels and the dispersion relations in a semiconductor quantum well one of the most versatile numerical methods that can be implemented for any type of quantum well is the *finite difference method* [24]. Consider a GaAs-GaAlAs quantum well that has been grown in the z-direction. The well is confined inside a box and placed in such a distance that the envelope functions are assumed to vanish at the sides of the box. A reasonable approximation is to take the width of the barrier material to be double the width of the well. In order to implement the finite difference method the interval of the z-axis across the quantum well has to be divided into a finite number of points, the meshpoints (figure 2.5). The number of points depends on the accuracy required. It is important to note that the more the number of points the more the time the computer requires to solve the problem.

In the finite difference method the first and the second derivatives $\partial F/\partial z$, $\partial^2 F/\partial z^2$ are substituted by differences at the meshpoints, using Taylor's expanding polynomials,

$$\frac{\Delta F_i}{\Delta z} = \frac{F_{i+1} - F_{i-1}}{2\Delta z} \tag{2.35}$$

$$\frac{\Delta^2 F_i}{\Delta z^2} = \frac{F_{i-1} + F_{i+1} - 2F_i}{(\Delta z)^2} \tag{2.36}$$

where z_i, i=0,...,5n, are the meshpoints and Δz is the distance between two consecutive points. Therefore, instead of one differential equation for each envelope function of the conduction and valence band, a system of n equations for each envelope function has been obtained. In other words each differential equation has been substituted by a nxn matrix problem.

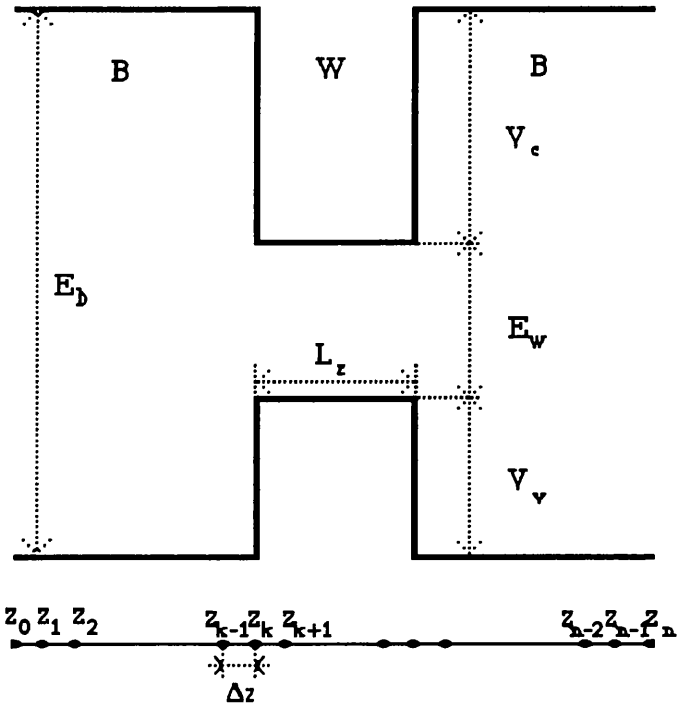

Figure 2.5. Finite difference method.

There are different methods available in order to calculate the eigenvalues and the eigenvectors of complex matrices. One is to reduce the complex matrix to upper Hessenberg form by elementary transformations and calculate the eigenvalues and the

eigenvectors using the LR algorithm and inverse iteration. An other is to use the property that the complex matrix is Hermitian and reduce it to a real tridiagonal matrix by unitary transformations. The eigenvalues and the eigenvectors are then derived using the QL algorithm. The first method gives very accurate results for the eigenvalues and it is suitable for multiple eigenvalue problems [25]-[26]. All the dispersion relations in the thesis have been calculated by using this method. The second method is not so accurate because when calculating doubly degenerate eigenvalues the values obtained are slightly different.

2.6 Numerical results and discussion

From the envelope function approximation described in the previous section the band-structure of different GaAs-$Ga_{1-x}Al_xAs$ square quantum wells can be calculated. The following parameters will be used in the numerical calculations; the Luttinger parameters for $Ga_{1-x}Al_xAs$ are equal to; $\gamma_1=6.85-3.4x$, $\gamma_2=2.1-1.42x$ and $\gamma_3=2.9-1.61x$, the effective mass for the conduction band is given by the expression $m_c^*=(0.067+0.058x)m_o$ [14], where $m_o=9.10956x10^{-31}kg$ is the free electron mass. These expressions were obtained by linear interpolation between the parameters of GaAs and AlAs. The energy gap of bulk GaAs at 0^oK is equal to 1.52eV and at 300^oK equal to 1.42eV [27]. The energy gap of $Ga_{1-x}Al_xAs$ depends on x and is given by the expression,

$$E_g(x) = E_g(GaAs)+1.04x+0.47x^2 \tag{2.37}$$

Consider a 10nm GaAs-$Ga_{0.75}Al_{0.25}As$ square quantum well. For x=0.25 the energy gap of the barrier material $Ga_{0.75}Al_{0.25}As$ is equal to $E_{gb}=1.71eV$. Assuming that the energy discontinuity for the conduction band is 57% of the difference in the energy gaps of the host materials [28], then the energy discontinuity in the conduction band is equal to 0.165eV and the energy discontinuity the valence band is equal to 0.124eV. The calculated

energy levels of the quantum well and their corresponding wavefunctions at $\mathbf{k}_{||}=0$ are shown in figure 2.6 for the conduction band and in figure 2.7 for the first three subbands of the valence band. Away from the zone centre the in-plane dispersion relations for the conduction band are assumed to be parabolic and can be described from expression (2.29). The valence band in-plane dispersion relations are calculated from the 4×4 Luttinger-Kohn Hamiltonian given in expression (2.31). For a 10nm GaAs-$Ga_{0.75}Al_{0.25}As$ square quantum well the valence band in-plane dispersion relations are shown in figure 2.8 and for a 12nm GaAs-$Ga_{0.75}Al_{0.25}As$ square quantum well in figure 2.9. It is important to mention that the subbands in figures 2.8 and 2.9 have been labelled according to their character at the zone centre. As the square quantum well displays centro-symmetry with respect to the centre of the well each of the subbands is twice degenerate. This degeneracy is the Kramers degeneracy and it is lifted for $\mathbf{k}_{||}\neq 0$ when the quantum well potential lacks inversion symmetry or when spin-orbit coupling is included in the calculations. Comparing the two square wells that are made up from the same barrier and well materials but differ in the width of the well, it can be observed that as the well width increases the number of bound states also increases. Moreover the energy separation between the states decreases and the states shift towards the bottom of the well.

It has been mentioned earlier that in the Luttinger-Kohn Hamiltonian the off-diagonal terms vanish at the zone centre and therefore there is no mixing of the light and heavy components. In this case it is possible to identify each subband as being light or heavy. If these terms were insignificant even when $\mathbf{k}_{||}\neq 0$ then the heavy and light hole bands would decouple and the in-plane dispersion would be parabolic. This is the diagonal approximation. Figure 2.10 displays the in-plane dispersion relations for the 10nm GaAs-$Ga_{0.75}Al_{0.25}As$ quantum well calculated from the diagonal approximation. It can be observed that the heavy hole (hh) and light hole (lh) subbands cross. This crossing is due to the mass reversal effect, where the heavy hole effective mass is heavy along the growth direction (**z**) but light in the layer plane (**xy**) and the light hole effective mass is light along

z but heavy in **xy**. The off-diagonal terms of the 4×4 Hamiltonian replace this crossing by an anticrossing (figure 2.11). The hh and lh subbands strongly mix away from $\mathbf{k}_{||}=0$ and it is not possible to identify each subband as light or heavy any longer. The exact position of the levels depends on the off-diagonal terms b and c. The term b mixes a given heavy hole subband with light hole subbands of the same parity, while the term c mixes it with light holes subbands of different parity. The valence band in-plane relations become highly non-parabolic and this is particularly prominent in the lh_1 subband which displays an electron-like curvature in the vicinity of $\mathbf{k}_{||}=0$. The notation hh and lh has very little significance at $\mathbf{k}_{||}\neq 0$ but will be kept to mark the subbands.

The valence bands are anisotropic and it is expected that for quantum wells the band dispersion will be different for different directions in the k_x, k_y plane. The valence band in-plane dispersion relations calculated in figures 2.8 and 2.9 were for **k** in the <110> direction. Figure 2.12 displays the dispersion relations calculated for **k** in the <010> direction for the 10nm GaAs-$Ga_{0.75}Al_{0.25}As$ quantum well. This warping of the bands is small but not negligible. If the parameters γ_2 and γ_3 of the Hamiltonian, in the c and c^* matrix elements, are replaced by an average parameter $\gamma=1/2(\gamma_2+\gamma_3)$, the Hamiltonian acquires cylindrical symmetry about the z-axis and the bands are isotropic in the k_x and k_y plane. This approximation which neglects the warping between the bands is called the *axial approximation*. It effects only the dispersion relations and not the $\mathbf{k}_{||}=0$ confinement energies.

The effect of an external applied electric field perpendicular to the quantum well interface can be incorporated into the theoretical calculations in a very straightforward fashion. For the valence band this is accomplished by including in each diagonal term of the Hamiltonian matrix a contribution -|e|Fz, where F is the magnitude of the applied field

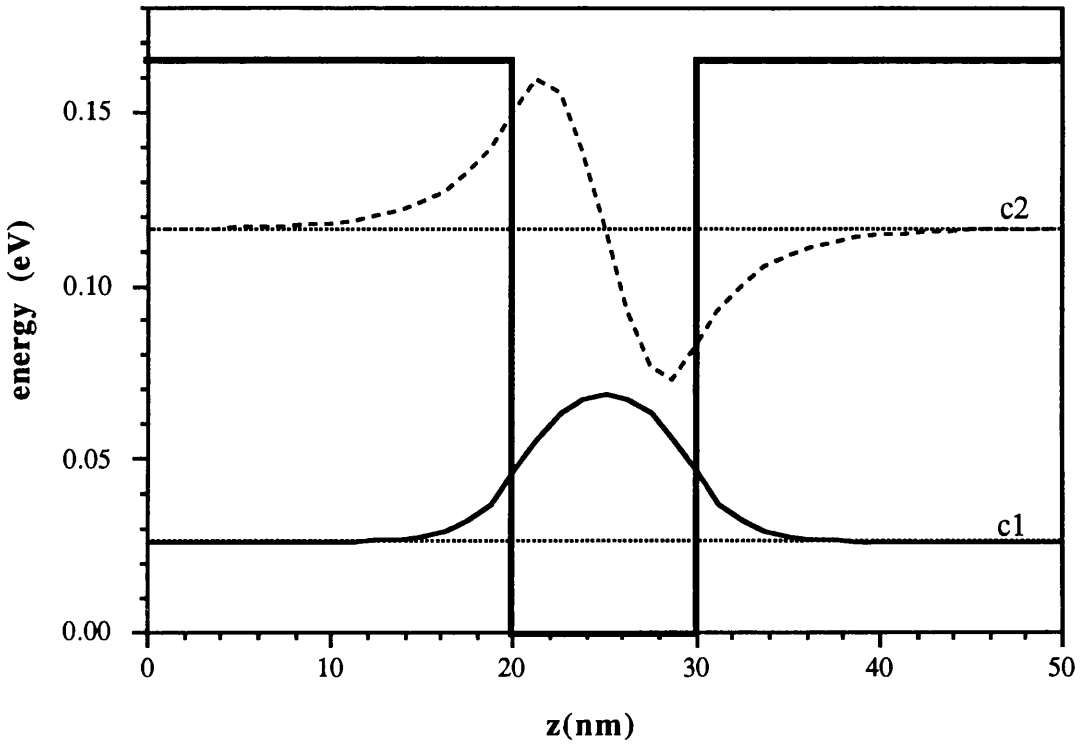

Figure 2.6. Conduction subband energy levels and wavefunctions for a 10nm GaAs-$Ga_{0.75}Al_{0.25}As$ square quantum well.

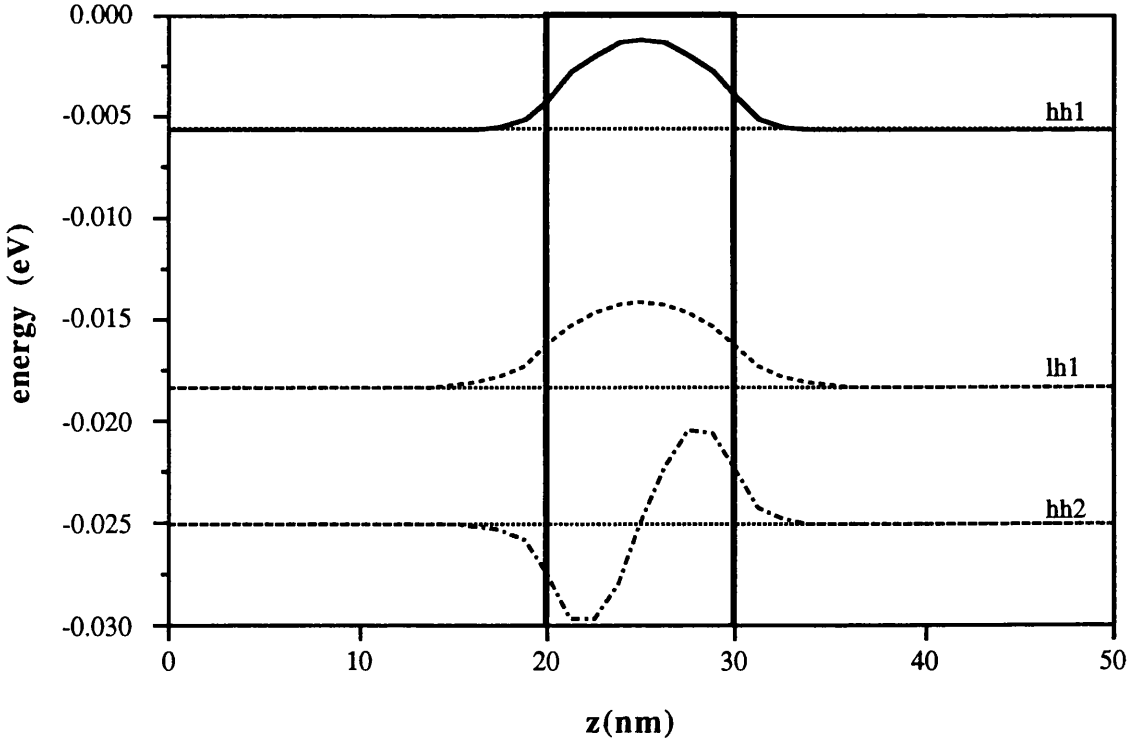

Figure 2.7. Valence subband energy levels and wavefunctions for a 10nm GaAs-$Ga_{0.75}Al_{0.25}As$ square quantum well.

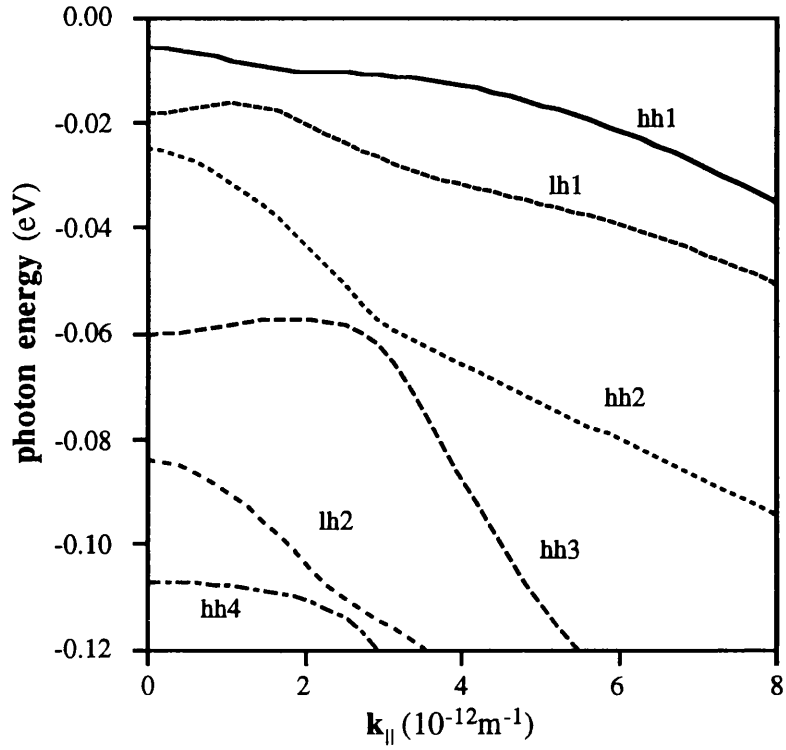

Figure 2.8. In-plane dispersion relations of the valence subbands of 10nm GaAs-$Ga_{0.75}Al_{0.25}As$ quantum well.

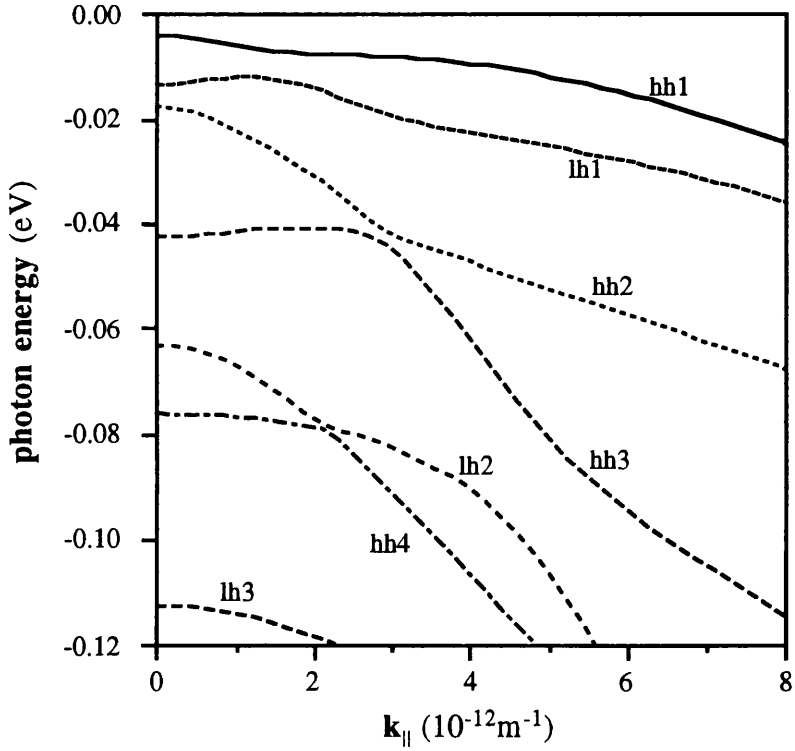

Figure 2.9. In-plane dispersion relations of the valence subbands of 12nm GaAs-$Ga_{0.75}Al_{0.25}As$ quantum well.

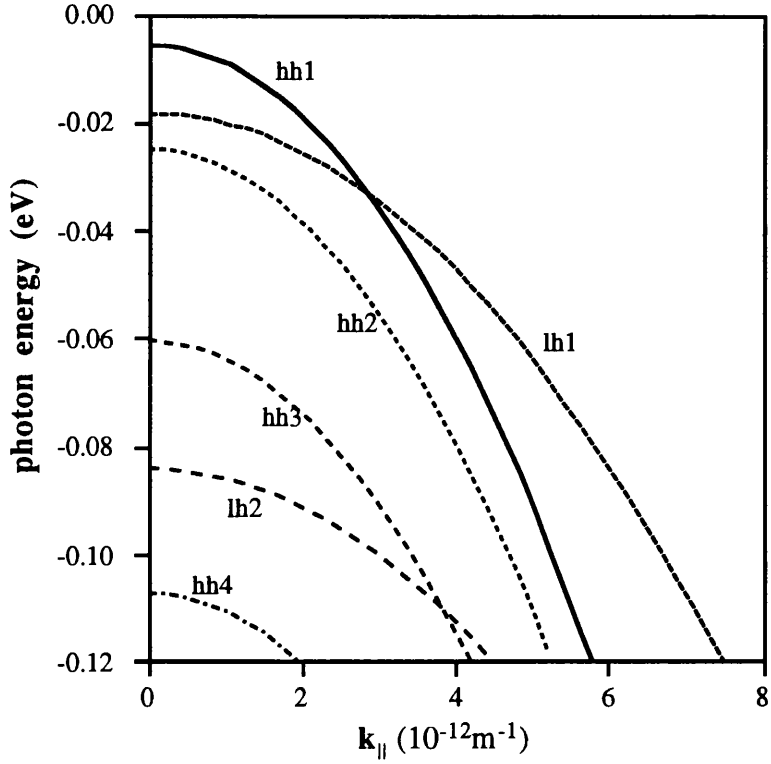

Figure 2.10. In-plane dispersion relations of the valence subbands of 10nm GaAs-$Ga_{0.75}Al_{0.25}As$ quantum well in the diagonal approximation.

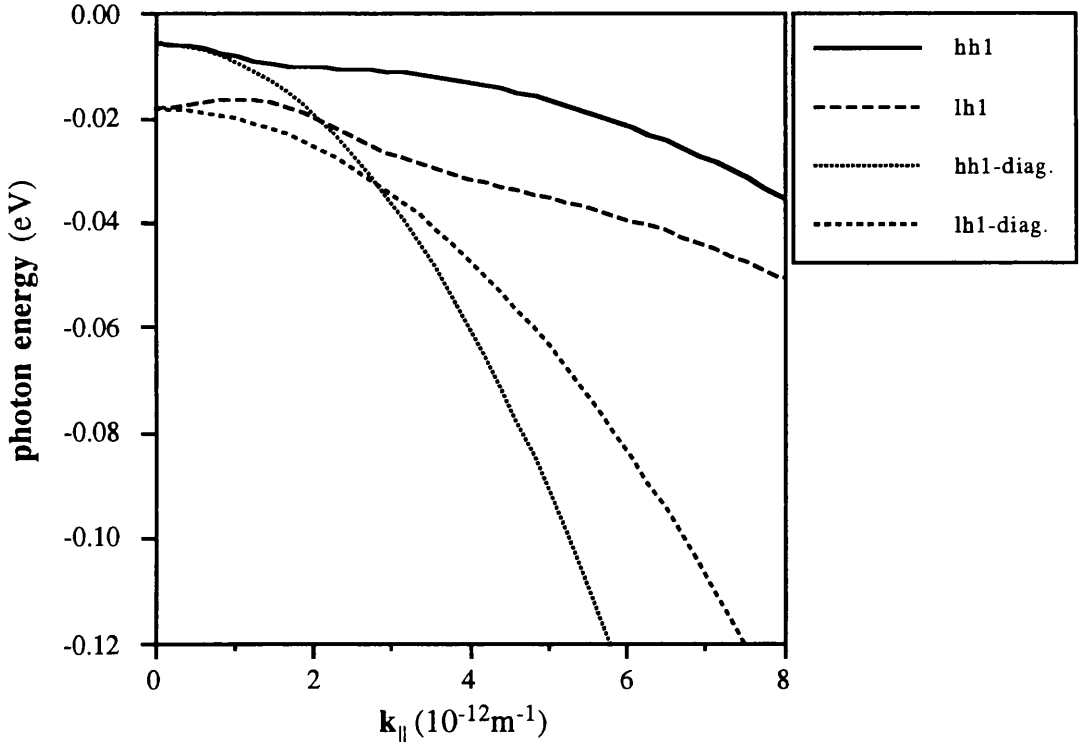

Figure 2.11. Comparison of the in-plane dispersion relations of the hh1 and lh1 valence subbands of 10nm GaAs-$Ga_{0.75}Al_{0.25}As$ quantum well obtained from the diagonal approximation and the valence band-mixing model.

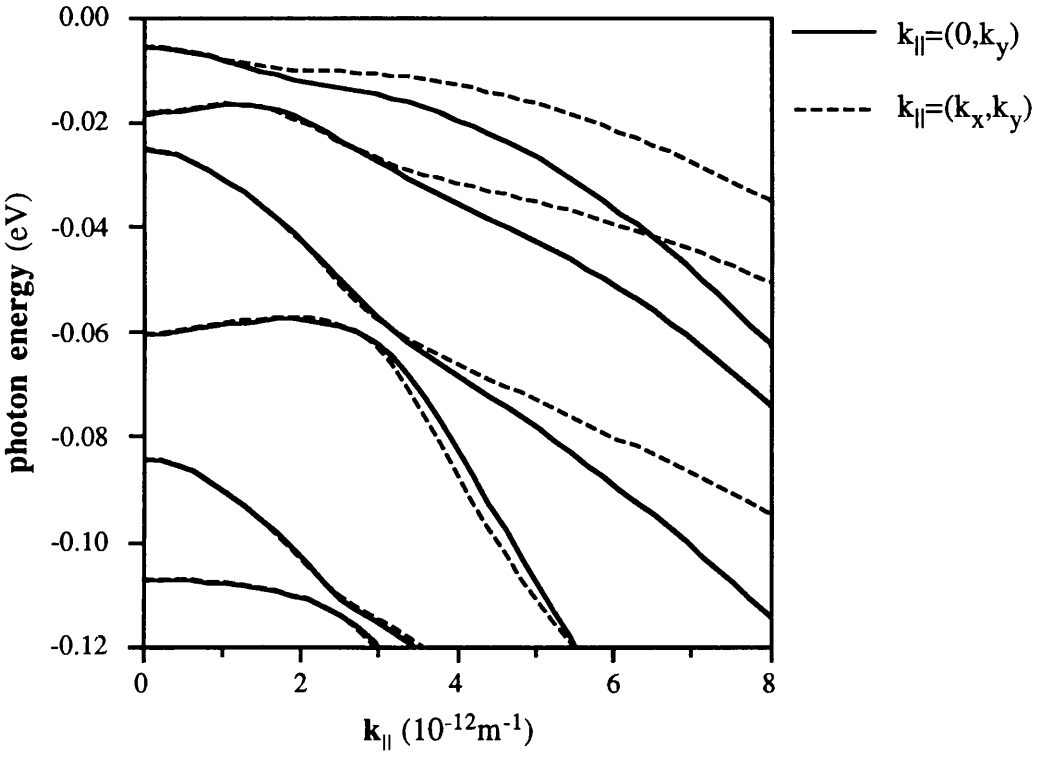

Figure 2.12. Comparison of the in-plane dispersion relations of the valence subbands of 10nm GaAs-$Ga_{0.75}Al_{0.25}As$ quantum well for the <110> and <010> directions.

and |e| is the magnitude of the electron charge. Similarly for the conduction band the external field can be incorporated by adding |e|Fz in the effective mass equation (2.28). Figures 2.13-2.16 show the effect of an electric field along the growth direction on the conduction band potential profile for four field values F=0,25,50,75 kV/cm. The energy levels and envelope functions displayed are the c1 and c2 at $\mathbf{k}_{||}=0$ for the 10nm GaAs-$Ga_{0.75}Al_{0.25}As$ quantum well. The wavefunctions shift with respect to the centre of the well with increasing electric field. This shift effects the overlap integral between the bound states. For those states with similar parity the integral decreases with increasing field, while for those with different parity it increases from zero (for F=0) to a finite value. With increasing electric field the ground state energies of the c1, hh1 and lh1 at $\mathbf{k}_{||}=0$ show upward shifts (figure 2.17). In contrast the upper states show downward shifts. This is the quantum-confined Stark effect. With the application of the field the inversion symmetry of the quantum well is broken and this lifts the two-fold spin degeneracy (figure 2.18).

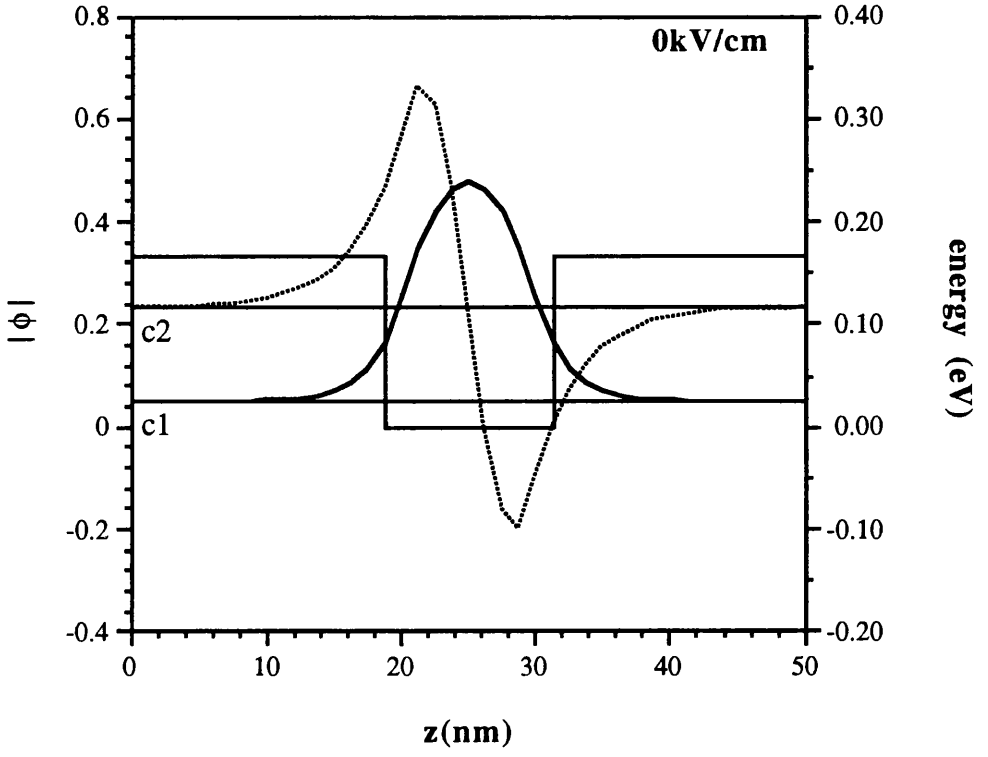

Figure 2.13. Conduction band confinement profile, energy levels and wavefunctions at $\mathbf{k}_{\|}=0$ with no external applied electric field (F=0).

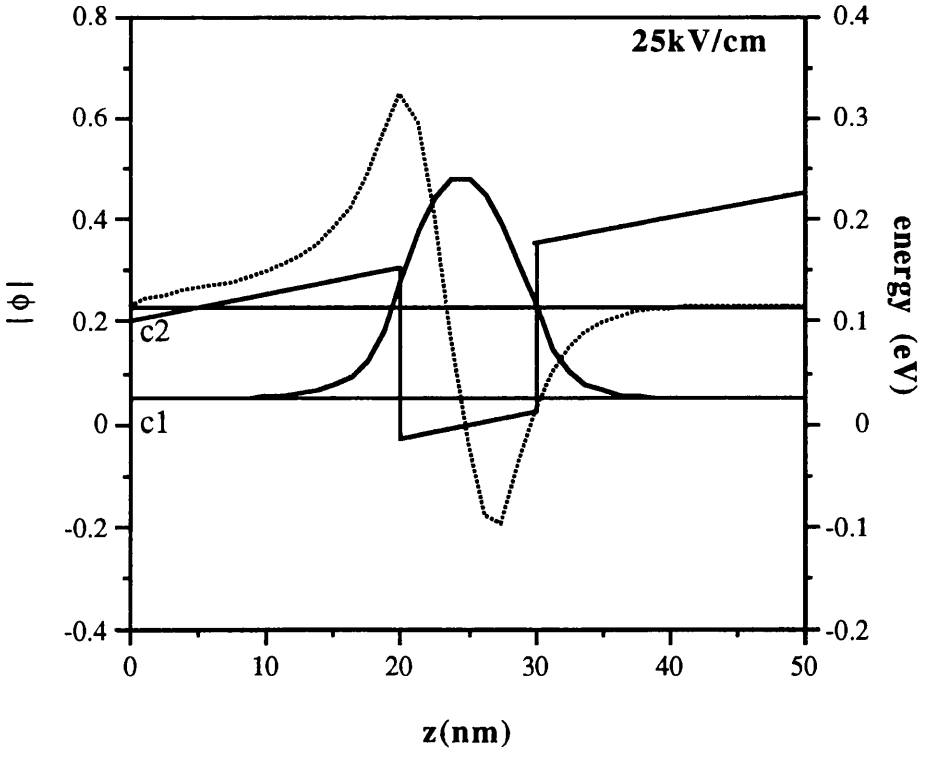

Figure 2.14. Conduction band confinement profile, energy levels and wavefunctions at $\mathbf{k}_{\|}=0$ with an external applied electric field equal to F=25kV/cm.

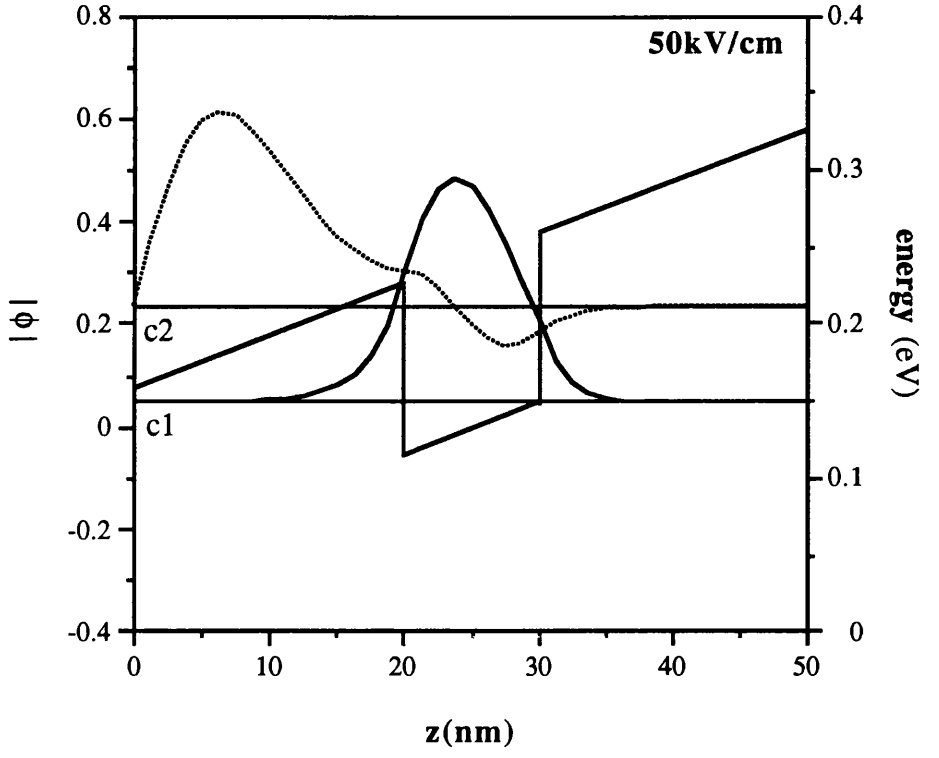

Figure 2.15. Conduction band confinement profile, energy levels and wavefunctions at $\mathbf{k}_{\|}=0$ with an external applied electric field equal to F=50kV/cm.

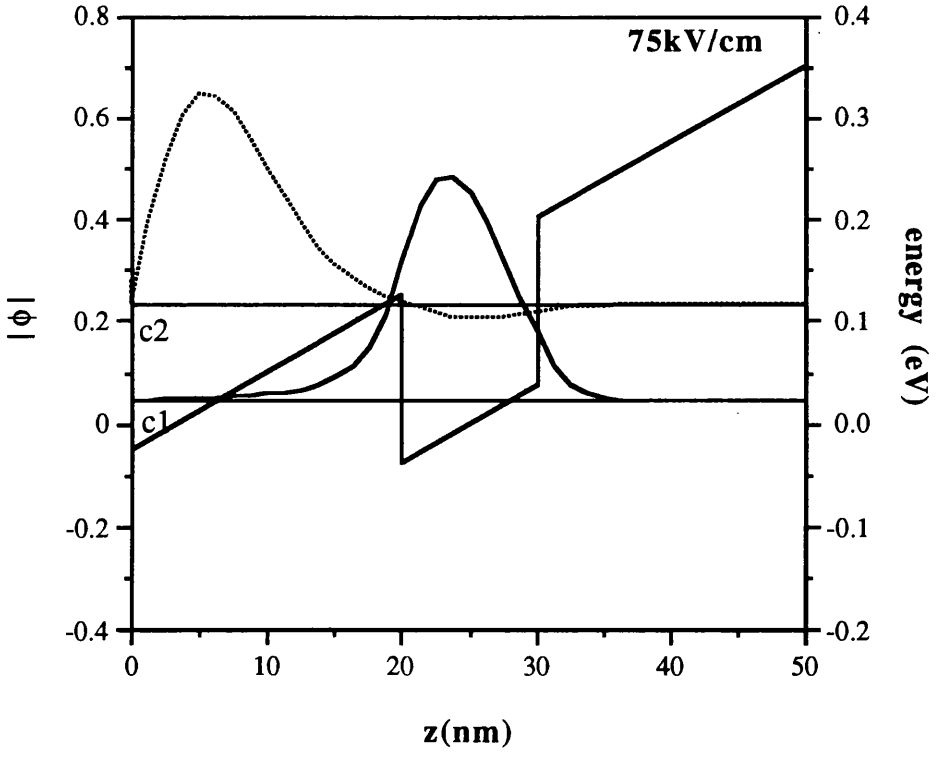

Figure 2.16. Conduction band confinement profile, energy levels and wavefunctions at $\mathbf{k}_{\|}=0$ with an external applied electric field equal to F=75kV/cm.

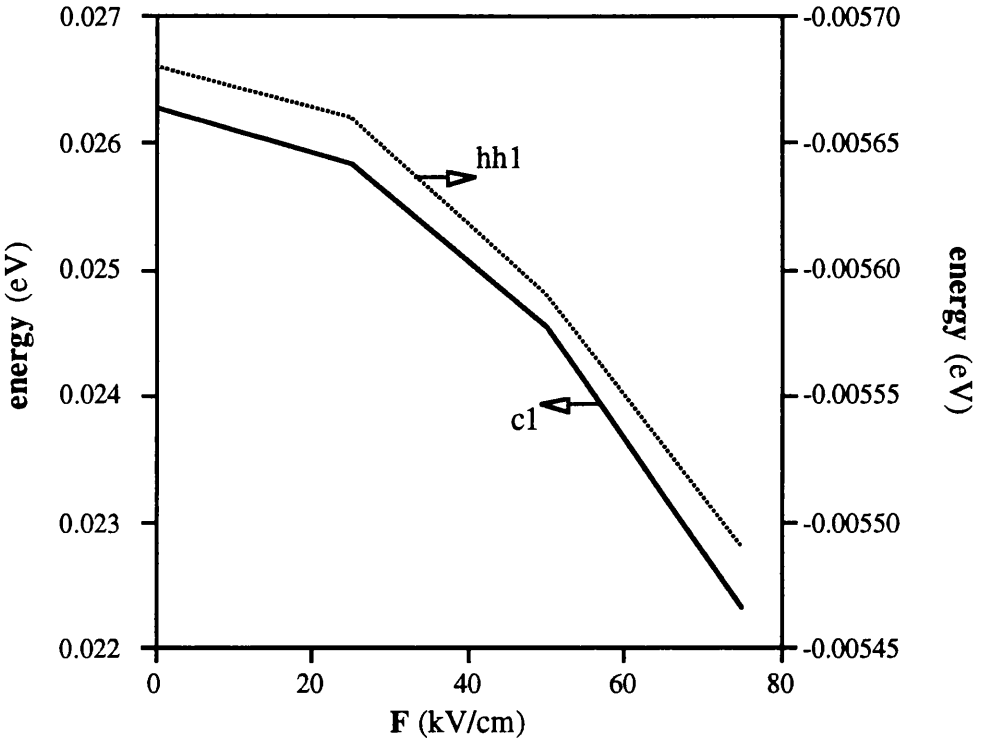

Figure 2.17. Shift of the c1 and hh1 subband energies with respect to an applied electric field.

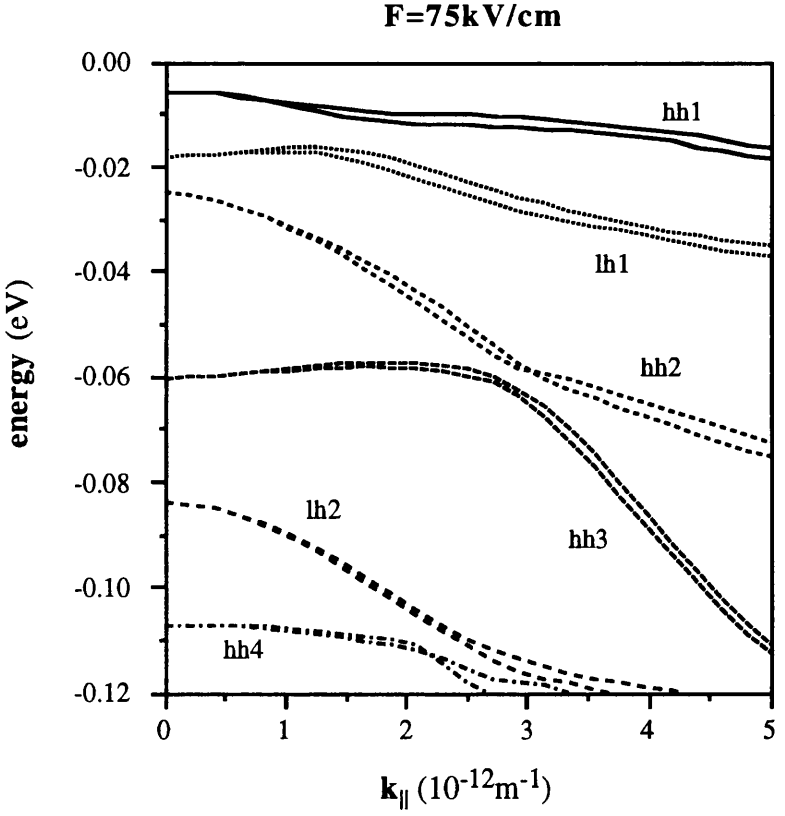

Figure 2.18. Valence band structure for a 10nm GaAs-$Ga_{0.27}Al_{0.25}As$ with an applied electric field F=75kV/cm.

The numerical results obtained for the conduction and valence band with the use of the finite difference method have been compared with analytical [13] and variational calculations [14], [28] and were found to be in very close agreement. Furthermore the accuracy of the results can be verified by comparing them with analytical calculations obtained from the Ben-Daniel Duke model [17]. This model works for the conduction, heavy hole and the light hole subbands at the zone centre $\mathbf{k}_{||}=0$. According to this model the energy levels must satisfy,

$$\cos\phi_w - \frac{m_b^* k_w}{m_w^* \kappa_b}\sin\phi_w = 0 \text{ for even states}$$

$$\cos\phi_w + \frac{m_w \kappa_b}{m_b k_w}\sin\phi_w = 0 \text{ for odd states} \tag{2.38}$$

(2.39)

where, $k_w = \sqrt{\frac{2m_w^*}{\hbar^2}(V_p - |E|)}$, $\kappa_b = \sqrt{\frac{2m_b^*}{\hbar^2}|E|}$ and $\phi_w = \frac{1}{2}k_w L_z$. The parameters m_w^*, m_b^*, V_p and E are the effective mass of the well and barrier material, the potential step and the energy levels at $\mathbf{k}_{||}=0$ respectively. These parameters take the values of the conduction, heavy hole and light hole bands when calculating the conduction, heavy hole and light hole energy levels respectively. Equations (2.38) and (2.39) can be solved graphically. In figures 2.19-2.21 the energy levels are calculated by the Ben-Daniel Duke model for a 10nm GaAs-$Ga_{0.75}Al_{0.25}As$ quantum well. The intersection points of the $\cos(\phi_w L_z)$ line and the lines termed as odd and even give the energy levels E. The subbands are equal to $(V_p - E)$, because in the Ben-Daniel Duke model the square well is assumed to have zero potential energy at the top of the well and $-V_p$ at the bottom of the well. The energy levels calculated (absolute values) from the finite difference method and the analytical model for the conduction, heavy hole and light hole subbands at $\mathbf{k}_{||}=0$ are compared in Table 2.2.

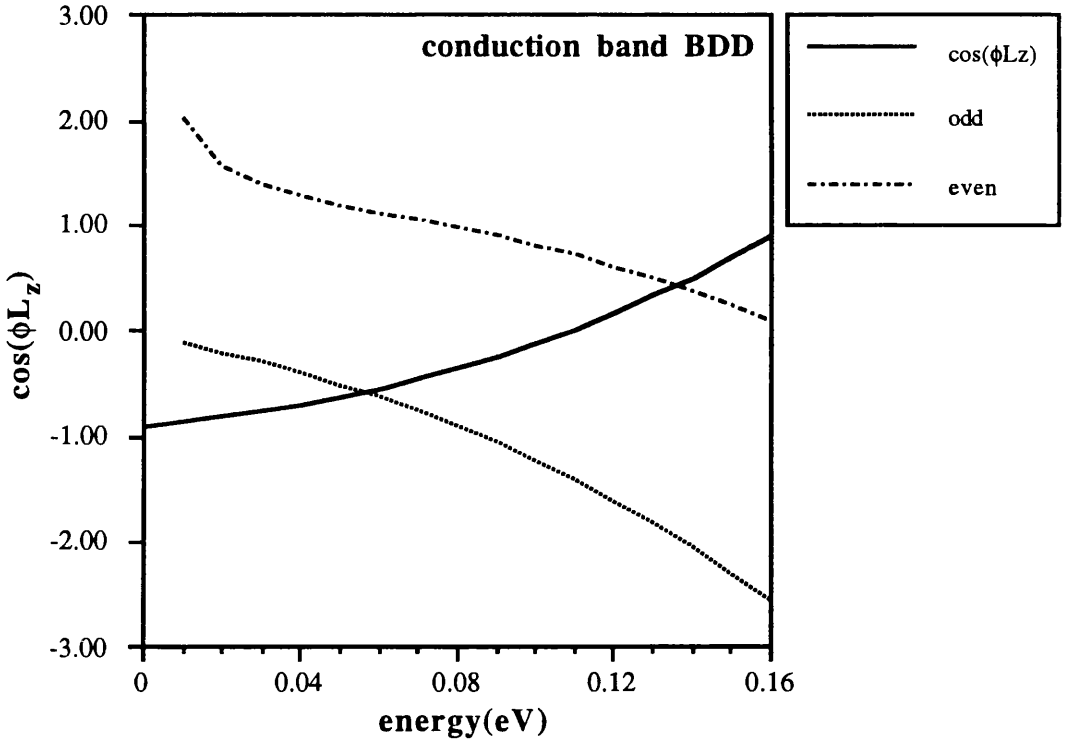

Figure 2.19. Ben Daniel-Duke model for the calculation of the conduction energy subbands.

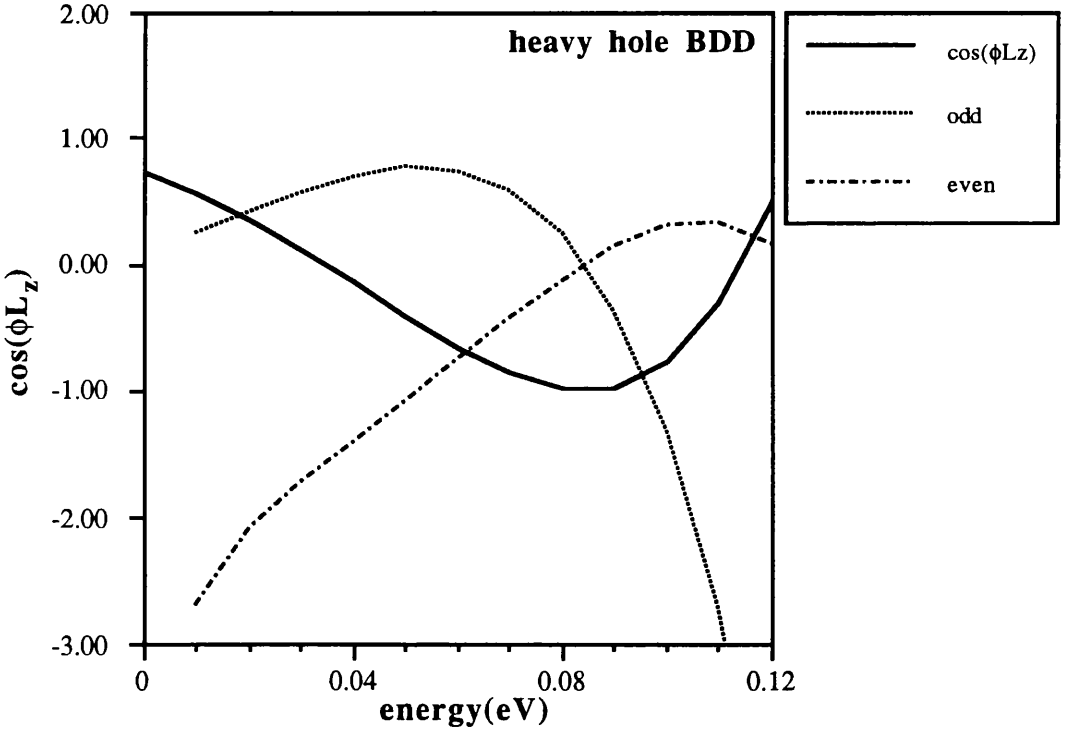

Figure 2.20. Ben Daniel-Duke model for the calculation of the heavy hole energy subbands.

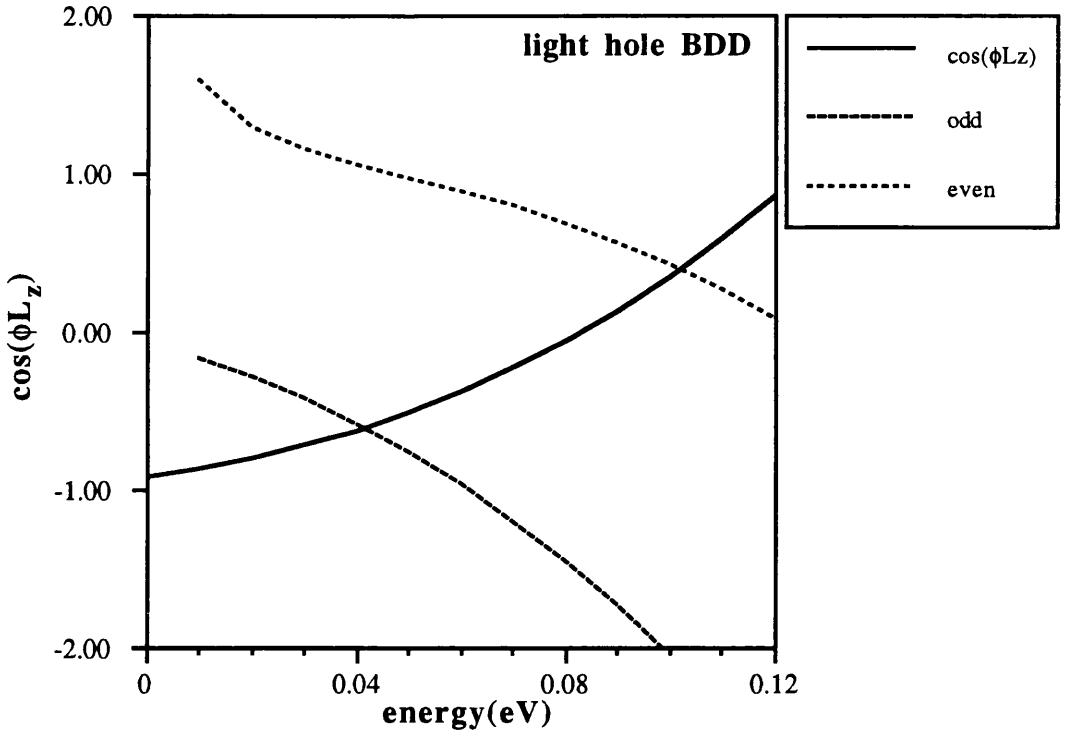

Figure 2.21. Ben Daniel-Duke model for the calculation of the light hole energy subbands.

TABLE 2.2. COMPARISON OF NUMERICAL AND ANALYTICAL SUBBAND CALCULATIONS

	conduction		heavy hole				light hole	
FDM	0.026	0.11	0.0057	0.025	0.061	0.107	0.019	0.084
BDD	0.024	0.108	0.0074	0.029	0.064	0.105	0.024	0.084

*FDM: Finite difference method
*BDD: Ben-Daniel Duke model
*All the numbers in the table are expressed in eV

From the table it can be observed that the results obtained from the numerical calculations are in close agreement to the analytical. The small differences originate from the assumption made in the finite difference method that the width of the barrier material is finite, while for the analytical calculations infinite. Moreover it is due to the error

introduced by the finite difference method with the substitution of the derivatives with differences and depends on the number of mesh points n and the distance between two consecutive mesh points Δz. It is of interest to see the change of the energy levels while the number of points of the mesh across the well is increased. Figure 2.22 displays the change of the calculated conduction subband energy levels with n.

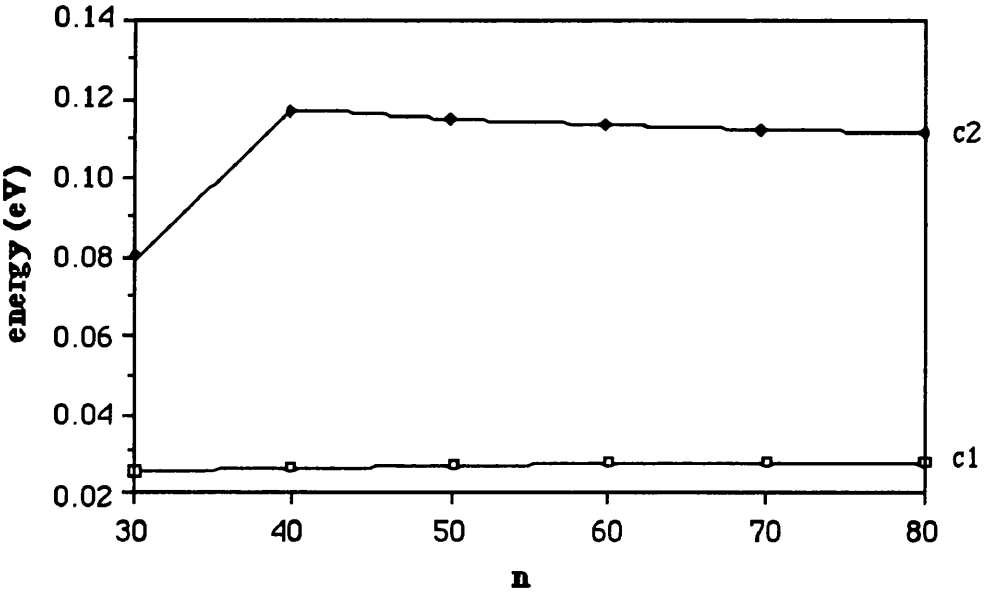

Figure 2.22. Change of energy levels in the conduction band with the number of mesh points.

It can be observed that the finite difference method converges as the number of points in the mesh increases. It is important to notice that if the number n is small then there are not enough points inside the well to satisfy the boundary conditions at both the interfaces and the solution is not correct. This is demonstrated in figure 2.22 for n=30 points where the 2nd order solution c2 differs significantly from the solutions obtained for $n \geq 40$. When the number of mesh points increases to more then 80 points, for the particular example, the errors in the numerical calculations increase and the solutions for the eigenvalues and the eigenvectors display an irregular behaviour.

2.7 Conclusions

In this chapter the envelope function approximation, based on the theory of the Luttinger-Kohn Hamiltonian, was presented as a method of calculating the band-structure of semiconductor quantum wells. One of the most important predictions obtained from this approximation is the significant valence band mixing for in-plane wave vectors away from the zone centre $\mathbf{k}_{||}=0$. Other important effects analysed by the envelope function approximation are the band-warping and the effect of an external applied electric field. The numerical results for the conduction and the heavy hole and light hole valence subbands were obtained using the finite difference method and were found to be in close agreement with the previously published data.

References

[1] M. Jaros, *Physics and applications of semiconductor microstructures*, (Series on Semiconductor Science and Technology, Clarendon Press, Oxford, 1989) Chapter 3

[2] N.G. Anderson and S.D. Jones, *Optimised tight-binding valence bands and heterojunction offsets in strained III-V semiconductors*, J. Appl. Phys., vol. **70**, pp. 4342-4356, 1991

[3] M. Sugara, *Tight-binding model including cation d orbitals to predict valence-band offset in zinc-blende semiconductor heterojunctions*, Phys. Rev. B, vol. **47**, pp. 7588-7593, 1993

[4] S. Brand and D.T. Hughes, *Calculations of bound states in the valence band of AlAs/GaAs/AlAs and AlGaAs/GaAs/AlGaAs quantum wells*, Semicond. Sci. Technol., vol. **2**, pp. 607-614, 1987

[5] G. Edwards and J.C. Inkson, *A pseudopotential calculation of the subband structure over the two-dimensional Brillouin zone in a GaAs quantum well*, Semicond. Sci. Technol., vol. **5**, pp. 1023-1029, 1990

[6] J.P. Cuypers and W. van Haeringen, *Matching of electronic wavefunctions and envelope functions at GaAs/AlAs interfaces*, J. Phys.:Condens. Matter, Phys. Rev. B, vol. **4**, pp. 2587-2608, 1992

[7] E.O. Kane, *The k.p method*, in *Semiconductors and Semimetals*, Volume 1, Physics of III-V Compounds, edited by R.K. Willardson and A.C. Beer

[8] J.M. Luttinger and W. Kohn, *Motion of electrons and holes in perturbed periodic fields*, Phys. Rev. B, vol. **97**, pp. 869-883, 1955

[9] J.M. Luttinger, *Quantum theory of cyclotron resonance in semiconductors: General theory*, Phys. Rev. B, vol. **102**, pp.1030-1041, 1956

[10] E.O. Kane, *Band structure of indium antimonide*, J. Phys. Chem. Solids, vol. **1**, pp.249-261, 1956

[11] E.O Kane, *Band structure of narrow gap semiconductors*, in *Narrow Gap Semiconductors Physics and Applications*, Proceedings of the International Summer School, Nîmes, France, edited by W. Zawadzki (Springer-Verlag 1980), pp. 13-31

[12] G. Bastard, *Superlattice band structure in the envelope function approximation*, Phys. Rev. B, vol. **24**, pp. 5693-5697, 1981

[13] D.A. Broido and L.J. Sham, *Effective masses of holes at GaAs-AlGaAs heterojunctions*, Phys. Rev. B, vol. **31**, pp. 888-892, 1985

[14] M. Altarelli, *Band structure, impurites and excitons in superlattices*, in *Proceedings of Les Houches Winterschool Semiconductor Superlattices and Heterojunctions*, edited by G. Allan, G. Bastard, N. Boccara, M. Lanoo and M. Voos (Springer, Berlin, 1986), pp. 12-37

[15] G. Bastard and J.A. Brum, *Electronic states in semiconductor heterostructures*, IEEE J. of Quant. Elec., vol. **22**, pp.1625-1644, 1986

[16] L.C. Andreani, A. Pasquarello and F. Bassani, *Hole subbands in strained GaAs -$Ga_{1-x}Al_xAs$ quantum wells: Exact solution of the effective-mass equation*, Phys. Rev. B, vol. **36**, pp. 5887-5894, 1987

[17] G. Bastard, *Wave mechanics applied to semiconductor heterostructures*, (Les édition de physique, 1988), Chapters 2 and 3

[18] A.M. Meney, *Orientation dependence of subband structure and optical properties in GaAs-AlGaAs quantum wells: [001], [111], [110] and [310] growth directions*, Superlattices and Microstructures, vol. **11**, pp. 31-40, 1992

[19] M. Altarelli, *Theoretical calculations of the electronic structure of superlattices*, Gallium Arsenide and Related Compounds 1987, Inst. Phys. Conf. Ser. No 91, Chapter 1, pp.15-19

[20] C. Kittel, *Quantum theory of solids*, (John Wiley, 1963), Chapter 9

[21] R.I. Taylor and M.G. Burt, *Continuity conditions for envelope functions at semiconductor interfaces derived from the Bastard model*, Semicond. Sci. Technol., vol. **2**, pp. 485-490, 1987

[22] D. Mukherji and B.R. Nag, *Band structure of semiconductor superlattices*, Phys. Rev. B, vol. **12**, pp. 4338-4345, 1975

[23] B.H. Bransden and C.J. Joachain, *Introduction to quantum mechanics*, (Longmand Scientific and Technical, 1989) Chapter 4

[24] R.L. Burden, J.D. Faires, A.C. Reynolds, *Numerical analysis*, (Wadsworth International Student Edition, 1981) Chapter 10

[25] J. Stoer and R. Buliasch, *Introduction to numerical analysis*, (Springer-Verlag 1980)

[26] W.H. Press, B.P. Flannery, S.A. Teukolsky, W.T. Vetterling, *Numerical recipes, The art of scientific computing*, (Cambridge University Press, 1988) Chapter 11

[27] C. Kittel, *Introduction to solid state physics*, (John Wiley, 1986), Chapter 8

[28] D. Ahn and S.L. Chuang, *Valence-band mixing effects on the gain and the refractive index change of quantum-well lasers*, J. Appl. Phys., vol. **64**, pp. 4056-4064, 1988

3 Optical Susceptibilities

3.1 Introduction

In optics we are concerned with the interaction of light with matter. This interaction can be expressed with the polarisation **P**, the effect induced by the optical field on a dielectric medium. The material properties can be described by expanding the polarisation **P** as a power series in the field **E**,

$$\mathbf{P} = \varepsilon_0\left(\chi^{(1)} \cdot \mathbf{E} + \chi^{(2)}:\mathbf{EE} + \chi^{(3)}:\mathbf{EEE} + \ldots\right) \tag{3.1}$$

where $\chi^{(1)}$ is the linear susceptibility and $\chi^{(2)}$, $\chi^{(3)}$,... are the nonlinear susceptibilities of the medium. In order to be able to describe the response of semiconductor heterostructures when applying an electric field, expressions for the linear and nonlinear susceptibilities associated with the crystalline properties of the heterostructure need to be derived. The method widely used for this purpose is the *density matrix formalism* [1]-[8] and it will be presented in this chapter. Based on this method expressions for the linear susceptibility and the second-order nonlinear susceptibility will be derived and the optical properties of semiconductor quantum wells will be evaluated.

3.2 Density matrix formalism

The density matrix formalism is a perturbation method of computing expectation values of operators, representing dynamical values of a system, in cases where only statistical information about the state of the system is known. In general there is not enough information to say that a system is characterised by a specific state function ψ. Therefore, when it is necessary to describe a system with the probability that the system is in the state ψ_n, where n labels the different possible states, the expectation value of an operator is given by,

$$\langle A \rangle = Tr(\rho A) \tag{3.2}$$

The density operator ρ contains all the physically significant information that can be known about the system. Each diagonal element of the density matrix ρ_{nn} is equal to the probability that the system is in particular state ψ_n. The off-diagonal elements do not have a simple explanation. They are a measure of the coherence of the superposition of states formed when an external perturbation is applied on the system. When the system is in thermal equilibrium these terms are zero.

In order to calculate the expectation values of the operators of the system, the properties of the density matrix need to be determined by solving the equation of motion of the density operator. For the optical phenomena examined, the system is initially in thermal equilibrium and is perturbed by applying a periodic electromagnetic field. The macroscopic response of the system to the external field can be obtained by calculating the average value of the appropriate tensor operator of the system.

3.2.1 Equation of motion of the density operator

In the absence of an external field, the energy of the system is represented with a Hamiltonian H_0,

$$H_0\psi_n=E_n\psi_n \tag{3.3}$$

where E_n are the allowed energy levels of the unperturbed system and ψ_n are the corresponding wavefunctions. The thermal equilibrium density operator $\rho^{(0)}$ represents the probability of finding the system initially with a certain energy. The probability is given by an appropriate distribution function, for example the Boltzmann distribution function,

$$\rho^{(0)}=\eta \exp(-H_0/kT) \tag{3.4}$$

η is a normalisation constant. The perturbation introduced by the external field $\mathbf{E}(t)$ is represented by the interaction Hamiltonian $H_I(t) = -\mathbf{M}\cdot\mathbf{E}(t)$, where $\mathbf{M}$ is the dipole operator. The Hamiltonian H of the perturbed system is given by,

$$H = H_0 + H_I(t) + H_R(t) \tag{3.5}$$

$H_R(t)$ represents the various relaxation processes. We assume that the external forces vanish in the remote past $H_I(-\infty)=0$ and the system is then in thermal equilibrium $\rho(-\infty)=\rho^{(0)}$. The equation of motion of the density operator $\rho(t)$ of the perturbed system is [2],

$$\begin{aligned} i\hbar\frac{d\{\rho(t)\}}{dt} &= [H,\rho(t)] \\ &= [H_0 + H_I(t),\rho(t)] + [H_R(t),\rho(t)] \\ &= [H_0 - \mathbf{M}\cdot\mathbf{E}(t),\rho(t)] - \frac{i\hbar}{2}[\Gamma\rho + \rho\Gamma] \end{aligned} \tag{3.6}$$

Γ is a diagonal matrix describing phenomenologically the relaxation of the system. This differential equation can be solved by applying the boundary conditions and expressing $\rho(t)$ in form of a perturbation series,

$$\rho(t) = \rho^{(0)} + \rho^{(1)}(t) + \rho^{(2)}(t) + \ldots + \rho^{(m)}(t) + \ldots = \sum_{m=0}^{\infty} \rho^{(m)}(t) \tag{3.7}$$

where $\rho^{(1)}(t)$ is linear in $\mathbf{E}(t)$, $\rho^{(2)}(t)$ is quadratic in $\mathbf{E}(t)$ and so on. From the boundary condition $\rho(-\infty)=\rho^{(0)}$ we notice that each term after $\rho^{(0)}$ must be set to zero in the distant past, $\rho^{(r)}(-\infty)=0$; r=1,2,...,∞. By equating terms involving same power of $H_I(t)$ we obtain a chain of equations,

$$\begin{aligned}
i\hbar\frac{d\rho^{(0)}}{dt} &= [H_0,\rho^{(0)}] \\
i\hbar\frac{d\rho^{(1)}(t)}{dt} &= [H_0,\rho^{(1)}(t)] - \frac{i\hbar}{2}[\Gamma\rho^{(1)} + \rho^{(1)}\Gamma] + [-\mathbf{M}\cdot\mathbf{E}(t),\rho^{(0)}(t)] \\
i\hbar\frac{d\rho^{(2)}(t)}{dt} &= [H_0,\rho^{(2)}(t)] - \frac{i\hbar}{2}[\Gamma\rho^{(2)} + \rho^{(2)}\Gamma] + [-\mathbf{M}\cdot\mathbf{E}(t),\rho^{(1)}(t)] \\
&\cdots\cdots\cdots \\
i\hbar\frac{d\rho^{(n)}(t)}{dt} &= [H_0,\rho^{(n)}(t)] - \frac{i\hbar}{2}[\Gamma\rho^{(n)} + \rho^{(n)}\Gamma] + [-\mathbf{M}\cdot\mathbf{E}(t),\rho^{(n-1)}(t)]
\end{aligned} \tag{3.8}$$

$\cdots\cdots\cdots$

These equations can be solved in stages. $\rho^{(0)}$ is already known and so we can solve the second equation to obtain $\rho^{(1)}$, then the third to obtain $\rho^{(2)}$ and so on.

In many practical applications the frequencies of the external electric field are in close resonance with the transition frequencies of the medium. So in order to obtain an expression for the linear and nonlinear susceptibilities of the medium we can treat it as a

multi-level system with energy levels in the conduction and valence band. The monochromatic incident field is defined as,

$$\mathbf{E}(t) = \mathbf{e}_\alpha E^\alpha(t) = \frac{1}{2}\mathbf{e}_\alpha(E_0^\alpha\, e^{-i\omega t} + E_0^{\alpha *} e^{i\omega t}) = \mathbf{e}_\alpha(\tilde{E}^\alpha\, e^{-i\omega t} + \tilde{E}^{\alpha *} e^{i\omega t})$$

(3.9)

$\mathbf{e}_\alpha$ is a unit vector in the direction of the electric field. The diagonal matrix elements of the dipole operator are equal to zero, which means physically that the atom does not possess a permanent electric dipole moment. The off-diagonal terms, between two levels l and m, are defined as $\mathbf{M}_{lm}=e\mathbf{r}_{lm}$. The interaction Hamiltonian is given by the product of the dipole moment matrix element and the electric field and so has only off-diagonal elements,

$$\langle m|H_I|l\rangle = -M_{lm}^\alpha E^\alpha$$

(3.10)

where M_{lm}^α is the matrix element of the dipole operator in the direction of the electric field. Using these assumptions, expression (3.8) can be written in a matrix form,

$$i\hbar\frac{d\rho_{lm}^{(n)}(t)}{dt} = (E_l - E_m)\rho_{lm}^{(n)} - i\hbar\gamma_{lm}\rho_{lm}^{(n)} - \sum_k\left\{E^\alpha(t)M_{lk}^\alpha\rho_{km}^{(n-1)} - \rho_{lk}^{(n-1)}M_{km}^\alpha E^\alpha(t)\right\}$$

(3.11a)

$$i\hbar\frac{d\rho_{mm}^{(n)}(t)}{dt} = -i\hbar\gamma_{mm}\rho_{mm}^{(n)} - \sum_k\left\{E^\alpha(t)M_{mk}^\alpha\rho_{km}^{(n-1)} - \rho_{mk}^{(n-1)}M_{km}^\alpha E^\alpha(t)\right\}$$

(3.11b)

where $\langle m|\Gamma|m\rangle = \gamma_{mm}$, $\langle l|\Gamma|l\rangle = \gamma_{ll}$ are the diagonal terms of the damping operator Γ and $\gamma_{lm} = \gamma_{ml} = \frac{1}{2}(\gamma_{ll} + \gamma_{mm})$. These damping terms have a physical meaning and represent dephasing processes that are due to interactions between the molecules of the material. The smallest value that γ_{lm} can take is $\gamma_{lm}=1/\tau_{sp}$, where τ_{sp} is the natural lifetime determined by the spontaneous emission, but usually there could be several simultaneous broadening

processes, such as collisions and lattice vibrations. In this case these are combined to one empirically determined value of $\gamma_{lm}=1/\tau_d$, where τ_d is the dephasing time.

The macroscopic polarisation **P** defined in a small volume V of the medium, to which an electric field is applied, is the expectation value of the dipole moment per unit volume,

$$P = \frac{1}{V}Tr(\rho M) \tag{3.12}$$

The polarisation can be written in the form of a perturbation series

$$\mathbf{P}=\mathbf{P}^{(1)}+\mathbf{P}^{(2)}+...+\mathbf{P}^{(n)}+... \tag{3.13}$$

where $P^{(1)}$ is linear to the electric field, $P^{(2)}$ quadratic etc.

3.3 Linear susceptibility

From (3.12) and (3.13) the linear polarisation can be expressed as,

$$P^{(1)} = \frac{1}{V}Tr(\rho^{(1)}M) \tag{3.14}$$

For the case of linear susceptibilities the medium can be described as an ensemble of two-level atoms. A two-level system consists of a single isolated atom with only two energy eigenstates, of energy E_a and E_b. If N is the number of systems in the states a and b per unit volume then the polarisation in the direction μ is given by,

$$P_{\mu}^{(1)} = N\sum_{a,b}(\rho_{ba}^{(1)}M_{ab}^{\mu} + \rho_{ab}^{(1)}M_{ba}^{\mu})$$

(3.15)

Equation (3.11) for $\rho^{(1)}$ can be solved by removing the rapid time variation, transforming the density matrix elements as sums of terms proportional to $\exp(\pm i\omega t)$ and equating those terms on both sides having the same time dependence [9]. So for,

$$\rho^{(1)} = \tilde{\rho}^{(1)}(\omega)\, e^{-i\omega t} + \tilde{\rho}^{(1)}(-\omega)\, e^{i\omega t}\}$$

(3.16)

expression (3.15) can be written as,

$$\begin{aligned} P_{\mu}^{(1)} &= N\sum_{a,b}(\rho_{ba}^{(1)}M_{ab}^{\mu} + \rho_{ab}^{(1)}M_{ba}^{\mu}) \\ &= N\sum_{a,b}\{[\tilde{\rho}_{ba}^{(1)}(\omega)M_{ab}^{\mu} + \tilde{\rho}_{ab}^{(1)}(\omega)M_{ba}^{\mu}]\, e^{-i\omega t} + [\tilde{\rho}_{ba}^{(1)}(-\omega)M_{ab}^{\mu} + \tilde{\rho}_{ab}^{(1)}(-\omega)M_{ba}^{\mu}]\, e^{i\omega t}\} \end{aligned}$$

(3.17)

Similarly equation (3.11a) is reduced to,

$$\hbar\omega\tilde{\rho}_{ab}^{(1)}(\omega) = \{(E_a - E_b) - i\hbar\gamma_{ab}\}\tilde{\rho}_{ab}^{(1)}(\omega) - (\rho_{bb}^{(0)} - \rho_{aa}^{(0)})M_{ab}^{\alpha}\tilde{E}^{\alpha}$$

(3.18)

from which we can obtain an expression for the first-order matrix element of the density operator between the states a and b,

$$\tilde{\rho}_{ab}^{(1)}(\omega) = -\frac{(\rho_{bb}^{(0)} - \rho_{aa}^{(0)})M_{ab}^{\alpha}\tilde{E}^{\alpha}}{\{\hbar\omega - (E_a - E_b) + i\hbar\gamma_{ab}\}} = \frac{(\rho_{bb}^{(0)} - \rho_{aa}^{(0)})M_{ab}^{\alpha}\tilde{E}^{\alpha}}{\{\hbar\omega_{ab} - \hbar\omega - i\hbar\gamma_{ab}\}}$$

(3.19)

where $\gamma_{ab} = \gamma_{ba} = \frac{1}{2}\left(\frac{1}{\tau_a} + \frac{1}{\tau_b}\right)$. The linear polarisation $P_{\mu}^{(1)}$ can be expressed with respect to the linear susceptibility $\chi_{\mu\alpha}^{(1)}(\omega)$,

$$P_\mu^{(1)} = \varepsilon_0\, \chi_{\mu\alpha}^{(1)}(\omega)\, \tilde{E}^\alpha\, e^{-i\omega t} + \varepsilon_0\, \chi_{\mu\alpha}^{(1)}(-\omega)\, \tilde{E}^{\alpha *}\, e^{i\omega t}$$

(3.20)

Substituting expression (3.19) for $\tilde{\rho}_{ab}^{(1)}$ into (3.18) and equating with (3.20), an expression for the linear optical susceptibility $\chi_{\mu\alpha}{}^{(1)}(\omega)$ can be obtained,

$$\chi_{\mu\alpha}^{(1)}(\omega) = \frac{N}{\varepsilon_0} \sum_{a,b} (\rho_{aa}^{(0)} - \rho_{bb}^{(0)}) \left\{ \frac{M_{ab}^\mu M_{ba}^\alpha}{\{\hbar\omega_{ba} - \hbar\omega - i\hbar\gamma_{ba}\}} + \frac{M_{ab}^\alpha M_{ba}^\mu}{\{\hbar\omega_{ba} + \hbar\omega + i\hbar\gamma_{ab}\}} \right\}$$

(3.21)

If the relaxation processes were negligible, $\gamma_{ab} = 0$, then (3.21) could be rewritten in a more compact form,

$$\boxed{\chi_{\mu\alpha}^{(1)}(\omega) = \frac{N}{\varepsilon_0 \hbar} \mathbf{S}_T \sum_{ab} (\rho_{aa}^{(0)} - \rho_{bb}^{(0)}) \left\{ \frac{M_{ab}^\mu M_{ba}^\alpha}{\omega_{ba} - \omega} \right\}}$$

(3.22)

where $\mathbf{S}_T$ is the *total symmetrisation operator* and it implies that the expression must be summed over the two permutations of the pairs $(\mu,-\omega_\sigma)$ and (α,ω), $\omega_\sigma=\omega$. The terms created by $\mathbf{S}_T$ can be depicted by the Feynman diagrams (figure 3.1). This expression is the same as that obtained from small-perturbation analysis and is used as a compact way of representing the $\chi_{\mu\alpha}{}^{(1)}(\omega)$ susceptibility tensor. In this expression the relaxation terms $\pm\gamma_{ab}$ can be introduced phenomenologically, the sign being predetermined by the principle of causality,

$$\chi_{\mu\alpha}^{(1)}(\omega) = \frac{N}{\varepsilon_0 \hbar} \mathbf{S}_T \sum_{ab} (\rho_{aa}^{(0)} - \rho_{bb}^{(0)}) \left\{ \frac{M_{ab}^\mu M_{ba}^\alpha}{\omega_{ba} - \omega \pm i\gamma_{ab}} \right\}$$

(3.23)

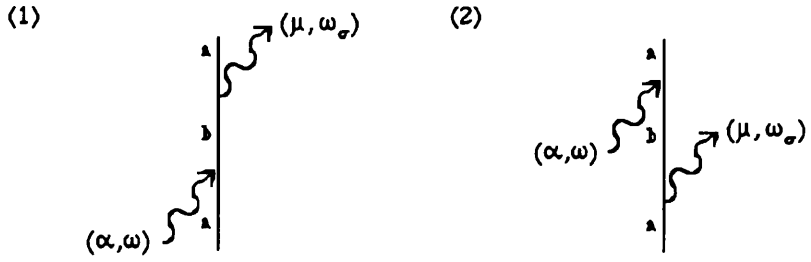

Figure 3.1. Feynman diagrams illustrating the 2 permutations involved in the determination of $\chi^{(1)}$

3.4 Second-order nonlinear susceptibility

The higher order susceptibilities can be calculated in a similar way [2], [10]-[11]. When two fields with frequencies ω_1 and ω_2 interact or one field interacts with itself, nonlinear polarisation terms with frequencies $\omega_\sigma=\omega_1+\omega_2$ or $\omega_\sigma=\omega_1-\omega_2$ are formulated due to mixing of the fields (for the case of one field interacting with itself $\omega_\sigma=2\omega_1$ or $\omega_\sigma=0$). These different terms are retrieved by taking the product of the two applied fields,

$$\mathbf{E}_i(t)\mathbf{E}_j(t) = \mathbf{e}_\alpha E_i^\alpha(t)\cdot\mathbf{e}_\beta E_j^\beta(t) = \mathbf{e}_\alpha\cdot\mathbf{e}_\beta(\tilde{E}_i^\alpha\, e^{-i\omega_i t}+\tilde{E}_i^{\alpha*}e^{i\omega_i t})(\tilde{E}_j^\beta\, e^{-i\omega_j t}+\tilde{E}_j^{\beta*}e^{i\omega_j t}) =$$

$$= \mathbf{e}_\alpha\cdot\mathbf{e}_\beta(\tilde{E}_i^\alpha\tilde{E}_j^\beta e^{-i(\omega_i+\omega_2)t}+\tilde{E}_i^\alpha\tilde{E}_j^{\beta*}e^{-i(\omega_i-\omega_2)t}+\tilde{E}_i^{\alpha*}\tilde{E}_j^\beta e^{-i(-\omega_i+\omega_2)t}+\tilde{E}_i^{\alpha*}\tilde{E}_j^{\beta*}e^{i(\omega_i+\omega_2)t}) \tag{3.24}$$

The method of obtaining an expression for the second-order nonlinear susceptibility is equivalent to that described in the previous section, but with some alterations. The system considered in this case is a three-level system, in order to account for the atomic transitions taking place. From equation (3.11a) the second-order density matrix element $\rho_{ab}^{(2)}$ can be evaluated (Appendix A),

$$\tilde{\rho}_{ab}^{(2)}(\omega_1+\omega_2)=\sum_c\left\{\frac{M_{ac}^{\beta}(\rho_{bb}^{(0)}-\rho_{cc}^{(0)})M_{cb}^{\alpha}\tilde{E}_i^{\alpha}\tilde{E}_j^{\beta}}{\{\hbar\omega_{ba}-\hbar(\omega_1+\omega_2)-i\hbar\gamma_{ab}\}\{\hbar\omega_{cb}-\hbar\omega_1-i\hbar\gamma_{cb}\}}\right.$$
$$\left.-\frac{M_{ac}^{\alpha}(\rho_{cc}^{(0)}-\rho_{aa}^{(0)})M_{cb}^{\beta}\tilde{E}_i^{\alpha}\tilde{E}_j^{\beta}}{\{\hbar\omega_{ba}-\hbar(\omega_1+\omega_2)-i\hbar\gamma_{ab}\}\{\hbar\omega_{ac}-\hbar\omega_2-i\hbar\gamma_{ac}\}}\right\}$$

(3.25)

where $\sum_c$ sums over all intermediate states c. The second-order polarisation can be expressed in the same way as $P^{(1)}$ in (3.17),

$$P_{\mu}^{(2)}=N\sum_{a,b}(\rho_{ba}^{(2)}M_{ab}^{\mu}+\rho_{ab}^{(2)}M_{ba}^{\mu})$$

(3.26)

and so from (A.2),

$$P_{\mu}^{(2)}=N\sum_{a,b}\{[\tilde{\rho}_{ba}^{(2)}((\omega_1+\omega_2))M_{ab}^{\mu}+\tilde{\rho}_{ab}^{(2)}((\omega_1+\omega_2))M_{ba}^{\mu}]\,e^{-i(\omega_1+\omega_2)t}+$$
$$+[\tilde{\rho}_{ba}^{(2)}(\omega_1-\omega_2)M_{ab}^{\mu}+\tilde{\rho}_{ab}^{(2)}(\omega_1-\omega_2)M_{ba}^{\mu}]\,e^{-i(\omega_1-\omega_2)t}+$$
$$+[\tilde{\rho}_{ba}^{(2)}(-\omega_1+\omega_2)M_{ab}^{\mu}+\tilde{\rho}_{ab}^{(2)}(-\omega_1+\omega_2)M_{ba}^{\mu}]\,e^{-i(-\omega_1+\omega_2)t}+$$
$$+[\tilde{\rho}_{ba}^{(2)}(-\omega_1-\omega_2)M_{ab}^{\mu}+\tilde{\rho}_{ab}^{(2)}(-\omega_1-\omega_2)M_{ba}^{\mu}]\,e^{i(\omega_1+\omega_2)t}\}$$

(3.27)

and with respect to the second-order nonlinear susceptibility,

$$P_{\mu}^{(2)}=\varepsilon_0\{\chi_{\mu\alpha\beta}^{(2)}(\omega_1+\omega_2)\,E_i^{\alpha}E_j^{\beta}e^{-i(\omega_1+\omega_2)t}+\chi_{\mu\alpha\beta}^{(2)}(\omega_1-\omega_2)E_i^{\alpha}E_j^{\beta*}\,e^{-i(\omega_1-\omega_2)t}+$$
$$+\chi_{\mu\alpha\beta}^{(2)}(-\omega_1+\omega_2)E_i^{\alpha*}E_j^{\beta}\,e^{-i(-\omega_1+\omega_2)t}+\chi_{\mu\alpha\beta}^{(2)}(-\omega_1-\omega_2)E_i^{\alpha*}E_j^{\beta*}\,e^{i(\omega_1+\omega_2)t}\}$$

(3.28)

By equating the expressions for the second-order polarisation an expression for $\chi_{\mu\alpha\beta}^{(2)}$ is acquired. However it is of importance to note that the susceptibility tensors in equation (3.27) should possess intrinsic permutation symmetry which means that they should be

invariant under the interchange of the pairs (α,ω_1) and (β,ω_2). In order to ensure this property the polarisation is expressed with respect to $\chi_{\mu\beta\alpha}^{(2)}$ as well as $\chi_{\mu\alpha\beta}^{(2)}$,

$$P_\mu^{(2)} = \varepsilon_0\Big\{\chi_{\mu\beta\alpha}^{(2)}(\omega_2+\omega_1)\,E_j^\beta E_i^\alpha e^{-i(\omega_2+\omega_1)t} + \chi_{\mu\beta\alpha}^{(2)}(\omega_2-\omega_1)E_j^\beta E_i^{\alpha*}\, e^{-i(\omega_2-\omega_1)t} + \\ + \chi_{\mu\beta\alpha}^{(2)}(-\omega_2+\omega_1)E_j^{\beta*}E_i^\alpha\, e^{-i(-\omega_2+\omega_1)t} + \chi_{\mu\beta\alpha}^{(2)}(-\omega_2-\omega_1)E_j^{\beta*}E_i^{\alpha*}\, e^{i(\omega_2+\omega_1)t}\Big\}$$

(3.29)

Adding together (3.28) and (3.29), dividing by 2 and setting,

$$\chi_{\mu\alpha\beta}^{(2)} = \tfrac{1}{2}(\chi_{\mu\alpha\beta}^{(2)} + \chi_{\mu\beta\alpha}^{(2)})$$

(3.30)

the susceptibility tensor $\chi_{\mu\alpha\beta}^{(2)}$ can be ensured to possess intrinsic permutation symmetry and can be expressed as,

$$\chi_{\mu\alpha\beta}^{(2)}(\omega_1+\omega_2) = \frac{N}{\varepsilon_0 2\hbar^2}\mathbf{S}\sum_{a\neq b}\sum_{c}\Bigg\{(\rho_{bb}^{(0)}-\rho_{cc}^{(0)})\frac{M_{ac}^\beta M_{cb}^\alpha M_{ba}^\mu}{\{\omega_{ba}-(\omega_1+\omega_2)-i\gamma_{ab}\}\{\omega_{cb}-\omega_1-i\gamma_{cb}\}} \\ -(\rho_{cc}^{(0)}-\rho_{aa}^{(0)})\frac{M_{ac}^\alpha M_{cb}^\beta M_{ba}^\mu}{\{\omega_{ba}-(\omega_1+\omega_2)-i\gamma_{ab}\}\{\omega_{ac}-\omega_2-i\gamma_{ac}\}}\Bigg\}$$

(3.31)

where **S** denotes summation over the terms obtained by interchanging (α,ω_1), (β,ω_2). As with the first order susceptibility tensor, $\chi_{\mu\alpha\beta}^{(2)}$ can be rewritten in a more compact way. By setting $\gamma_{ab} = \gamma_{ac} = 0$ and using the identity,

$$\frac{1}{\{\omega_{ba}-(\omega_1+\omega_2)\}}\frac{1}{\{\omega_{ac}-\omega_2\}} + \frac{1}{\{\omega_{ba}-(\omega_1+\omega_2)\}\{\omega_{cb}-\omega_1\}} = \frac{1}{\{\omega_{ac}-\omega_2\}\{\omega_{cb}-\omega_1\}}$$

(3.32)

as well as rearranging the subscripts a,b,c we finally obtain,

$$\chi^{(2)}_{\mu\alpha\beta}(\omega_1+\omega_2)=\frac{N}{\varepsilon_0 2\hbar^2}\mathbf{S}_T\sum_{a,b,c}\left[\rho^{(0)}_{aa}\frac{M^{\mu}_{ab}M^{\alpha}_{bc}M^{\beta}_{ca}}{\{\omega_{ba}-(\omega_1+\omega_2)\}\{\omega_{ca}-\omega_1\}}\right]$$

(3.33)

where $\mathbf{S_T}$ is the total symmetrisation operator and it implies that the expression must be summed over the six permutations of the pairs $(\mu,-\omega_\sigma)$ and (α,ω_1), (β,ω_2), $\omega_\sigma=\omega_1+\omega_2$. The 6 terms created by $\mathbf{S_T}$ can be depicted by the Feynman diagrams (figure 5.7). This expression is the same as that obtained from small-perturbation analysis and is used as a compact way of representing the $\chi_{\mu\alpha\beta}{}^{(2)}(\omega_1+\omega_2)$ susceptibility tensor. Similarly to the linear susceptibility the relaxation terms $\pm\gamma_{ab}$, $\pm\gamma_{ac}$ can be introduced phenomenologically,

$$\chi^{(2)}_{\mu\alpha\beta}(\omega_1+\omega_2)=\frac{N}{\varepsilon_0 2\hbar^2}\mathbf{S}_T\sum_{a,b,c}\left[\rho^{(0)}_{aa}\frac{M^{\mu}_{ab}M^{\alpha}_{bc}M^{\beta}_{ca}}{\{\omega_{ba}-(\omega_1+\omega_2)\pm i\gamma_{ab}\}\{\omega_{ca}-\omega_1\pm i\gamma_{ac}\}}\right]$$

(3.34)

3.5 Density of states

In order to calculate the magnitude of the susceptibilities for a semiconductor heterostructure we need to estimate $N(\rho_{aa}{}^{(0)}-\rho_{bb}{}^{(0)}) \equiv (N_1-N_2)$, the average density of the population difference between two levels of the semiconductor material. Electrons are Fermi particles and their distribution among the available states of a dynamical system is given by the Fermi-Dirac distribution [12],

$$f(E)=\left\{1+\exp\left[(E-E_f)/kT\right]\right\}^{-1}$$

(3.35)

The distribution gives the fraction f(E) of available states at the energy E actually occupied by electrons under the condition of thermal equilibrium. T is the temperature and E_f is the

Fermi energy. When the electron density is low, f(E) can be approximated by the Boltzmann distribution,

$$f(E) = \{\exp[-(E - E_f) / kT]\}^{-1}$$

(3.36)

In the event of the thermal equilibrium of the heterostructure being disturbed, separate Fermi levels E_{fc} and E_{fv}, called *quasi-Fermi* levels, are used for the conduction and the valence band,

$$f_c(E_{cn}) = \left\{1 + \exp\left[(E_{cn} - E_{fc}) / kT\right]\right\}^{-1}$$
$$f_v(E_{v\ell}) = \left\{1 + \exp\left[(E_{v\ell} - E_{fv}) / kT\right]\right\}^{-1}$$

(3.37)

The Fermi levels are related to the density of electrons n and holes p in the quantum well [13] and can be calculated from,

$$n \approx \frac{kT}{\pi\hbar^2 L_z} \sum_n m^*_{cn} \ln\left\{1 + \exp\left[(E_{fc} - E_{cn}) / kT\right]\right\}$$
$$p \approx \frac{kT}{\pi\hbar^2 L_z} \sum_\ell m^*_{p\ell} \ln\left\{1 + \exp\left[(-E_{fv} - E_{p\ell}) / kT\right]\right\}$$

(3.38)

m_{cn}^* is the conduction band effective mass and $m_{p\ell}^*$ is the valence band effective mass. For the semiconductor materials analysed here, there are three valence bands, heavy hole, light hole and split-off bands with different effective masses. For the calculation of the quasi-Fermi level in the valence band the heavy hole band is used, assuming that it makes the most significant contribution.

The allowed optical transitions between two states can be split into two categories, the *intraband* and the *interband* transitions. The intraband transitions occur between subbands

within the same band, while interband transitions occur between subbands from different bands. Restricting the calculations of the susceptilities to those originating from interband transitions, between the conduction and the valence band of a semiconductor material, the subset of electrons with value k within a range dk contributing to the inversion density is given by,

$$d(N_1 - N_2) \rightarrow \frac{\rho_{ds}(k)dk}{V}\{f_c(E_b)[1 - f_v(E_a)] - f_v(E_a)[1 - f_c(E_b)]\} \tag{3.39}$$

which is reduced to,

$$d(N_1 - N_2) \rightarrow \frac{\rho_{ds}(k)dk}{V}\{f_c(E_b) - f_v(E_a)\} \tag{3.40}$$

where $V=L_xL_yL_z$, L_i length of the crystal in the i direction, i=x,y,z, $\rho_{ds}(k)$ is the density of states in **k**-space. $\rho_{ds}(k)dk$ is the number of states within dk, while the Fermi factors ensure that only occupied states are counted as initial states of a transition and only empty states for final states. The number of states within dk for bulk semiconductor materials, $\rho_b(k)dk$, is given by the volume of a spherical shell of radius k and thickness dk divided by the volume per state in **k**-space $8\pi^3/V$,

$$\rho_b(k)\, dk = \frac{k^2 V}{2\pi^2} dk \tag{3.41}$$

Electrons in quantum wells are restricted in two-dimensions and so the number of states between *k* and d*k* for a semiconductor quantum well $\rho_{qw}(k)dk$ is equal to,

$$\rho_{qw}(k)\, dk = \frac{k\, S}{2\pi} dk \tag{3.42}$$

where $k=|\mathbf{k}_{||}|$, $\mathbf{k}_{||}=(k_x,k_y)$ the in-plane **k**-vector and $S=L_xL_y$. For a quantum well with well width L_z the average density of the population difference between the two levels a and b, $d(N_1-N_2)$, in the range dk is equal to,

$$d(N_1 - N_2) \rightarrow \frac{k\ dk}{2\pi L_z}\{f_c(E_b) - f_v(E_a)\} \tag{3.43}$$

Substituting equation (3.43) into the expressions for the linear susceptibility and the nonlinear second-order susceptibility and setting $E_{ba}(k)=\hbar\omega_{ba}$, we obtain the following expressions for $\chi_{\mu\alpha}^{(1)}(\omega)$,

$$\chi_{\mu\alpha}^{(1)}(\omega) = \frac{1}{\varepsilon_0 2\pi L_z} \int_{\substack{0 \\ (\mathbf{k}_{||} \in 1^{st}\,B.Z).}}^{k_{max}} dk\ k \sum_{a,b} \{f_c(E_b) - f_v(E_a)\} \left\{ \frac{M_{ab}^{\mu} M_{ba}^{\alpha}}{\{E_{ba}(k) - \hbar\omega - i\hbar\gamma_{ba}\}} + \frac{M_{ab}^{\alpha} M_{ba}^{\mu}}{\{E_{ba}(k) + \hbar\omega + i\hbar\gamma_{ab}\}} \right\} \tag{3.44}$$

where the sum is over all valence band states a and conduction band states b and the two spin states associated with them. Similarly for $\chi_{\mu\alpha\beta}^{(2)}(\omega_1+\omega_2)$,

$$\chi_{\mu\alpha\beta}^{(2)}(\omega_1 + \omega_2) = \frac{1}{4\pi\varepsilon_0 L_z} \mathbf{S}_T \int_{\substack{0 \\ (\mathbf{k}_{||} \in 1^{st}\,B.Z)}}^{k_{max}} dk\ k \sum_{a,b,c} \{f_v(E_a)[1 - f_c(E_b)]\} \left[\frac{M_{ab}^{\mu} M_{bc}^{\alpha} M_{ca}^{\beta}}{\{E_{ba}(k) - \hbar\omega_1 - \hbar\omega_2 \pm i\hbar\gamma_{ab}\}\{E_{ca}(k) - \hbar\omega_1 \pm \hbar i\gamma_{ac}\}} \right] \tag{3.45}$$

3.6 Dipole moment matrix elements

The optical dipole operator element for the transition between two states i and j, $\mathbf{M_{ij}}$, is equivalent to the integral [5],

$$\mathbf{M_{ij}} = \langle \psi_i | \, e\mathbf{r} \, | \psi_j \rangle = e \int_V \psi_i^*(\mathbf{r}) \, \mathbf{r} \, \psi_j(\mathbf{r}) dV \tag{3.46}$$

ψ_i is the wavefunction of the state i. It has been shown that every wavefunction ψ_i of a semiconductor heterostructure can be expressed as the product of an envelope function and the periodic part of the Bloch function of the band edge the state i is originating from,

$$\psi_i(\mathbf{r}) = f_i(\mathbf{r}) \, u_{i0}(\mathbf{r}) = \frac{1}{\sqrt{S}} e^{i\mathbf{k}_{\parallel} \cdot \mathbf{r}_{\parallel}} \phi_i(z) u_{i0}(\mathbf{r}) \tag{3.47}$$

Substituting expression (3.47) into (3.46), the expression for the optical dipole elements can be simplified (Appendix B),

$$\langle \psi_i | \, e\mathbf{r} \, | \psi_j \rangle \approx \langle u_{i0} | e\mathbf{r} | u_{j0} \rangle \langle \phi_i^* | \phi_j \rangle + e\delta_{ij} \langle \phi_i^* | \mathbf{r} | \phi_j \rangle \tag{3.48}$$

For the interband transition between a valence subband ℓ and a conduction subband m the dipole moment matrix element is approximately equal to (Appendix B),

$$\langle \psi_v^{\ell} | \, e\mathbf{r} \, | \psi_c^m \rangle \approx \langle u_v | \, e\mathbf{r} \, | u_c \rangle \langle \phi_v^{\ell} | \phi_c^m \rangle = \langle u_v | \, e\mathbf{r} \, | u_c \rangle \int_{-\infty}^{+\infty} \phi_v^{\ell *}(z) \phi_c^m(z) dz \tag{3.49}$$

where u_c and u_v are the periodic parts of the Bloch functions at the zone centre $\mathbf{k}$=0, for the conduction and valence bands. Interband transitions are restricted by selection rules. The first rule arises from the requirement that the dipole matrix element $\langle u_{i0} | \mathbf{r} | u_{j0} \rangle$ must be

different from 0, for the dipole moment matrix element to be different from 0. For the different possible polarisation directions of the light waves, the magnitude of the dipole matrix element $\langle u_{i0}|\mathbf{r}|u_{j0}\rangle$ is given in table 3.1. It has been calculated from the expressions of the periodic part of the Bloch functions for the different band extrema the of the Kane model [14], presented in chapter 2.

TABLE 3.1. SELECTION RULES FOR INTERBAND TRANSITIONS

Heavy Hole to Conduction Band

propagation	$\langle u_{hh}\|ex\|u_c\rangle$	$\langle u_{hh}\|ey\|u_c\rangle$	$\langle u_{hh}\|ez\|u_c\rangle$
// z	$1/\sqrt{2}\langle S\|ex\|X\rangle$	$1/\sqrt{2}\langle S\|ey\|Y\rangle$	impossible
// x	impossible	$1/\sqrt{2}\langle S\|ey\|Y\rangle$	forbidden
// y	$1/\sqrt{2}\langle S\|ex\|X\rangle$	impossible	forbidden

Light Hole to Conduction Band

propagation	$\langle u_{lh}\|ex\|u_c\rangle$	$\langle u_{lh}\|ey\|u_c\rangle$	$\langle u_{lh}\|ez\|u_c\rangle$
// z	$1/\sqrt{6}\langle S\|ex\|X\rangle$	$1/\sqrt{6}\langle S\|ey\|Y\rangle$	impossible
// x	impossible	$1/\sqrt{6}\langle S\|ey\|Y\rangle$	$2/\sqrt{6}\langle S\|ez\|Z\rangle$
// y	$1/\sqrt{6}\langle S\|ex\|X\rangle$	impossible	$2/\sqrt{6}\langle S\|ez\|Z\rangle$

* $\langle S|ex|X\rangle = \langle S|ey|Y\rangle = \langle S|ez|Z\rangle$ are related to P, the interband matrix element of the velocity operator,

$$P = -i\frac{\hbar}{m_0}\langle S|p_z|Z\rangle \approx -\frac{e}{E_g}\langle S|ez|Z\rangle \tag{3.50}$$

The value of P or $E_p = 2m_0P^2/\hbar^2$ is almost material independent. For bulk GaAs it is equal to $E_p \approx 23$eV [15].

The second selection rule requires that the overlap integral between the envelope functions is different from zero. For a symmetric quantum well the envelope functions have a definite parity with respect to the centre of the well. Under these circumstances the overlap integral is non zero only if the envelope functions of the initial and the final states have the same parity. If the quantum numbers of the initial state is n and of the final state is m, then the overlap integral is non zero only when n+m is even. This selection rule does not apply to asymmetric quantum wells, for which the envelope functions are not symmetric with respect to the centre of the well and therefore transitions with n+m odd are allowed.

Applying the selection rules from Table 3.1 to the two different types of field polarisations TE and TM, the allowed atomic transitions between the conduction band and the valence band can be obtained and the dipole moment matrix element for each polarisation can be evaluated. For;

TE mode (y-propagation, field components E_x and H_z)

$$M_{\ell m} = \left\langle \psi_{hh}^{\ell} \middle| ex \middle| \psi_c^m \right\rangle = \left\langle u_{hh} \middle| ex \middle| u_c \right\rangle \left\langle \phi_v^{\ell} \middle| \phi_c^m \right\rangle = \frac{1}{\sqrt{2}} \langle S|ez|Z \rangle \int_{-\infty}^{+\infty} \phi_v^{\ell *}(z) \phi_c^m(z) dz, \tag{3.51}$$

when the subband ℓ is heavy hole,

$$M_{\ell m} = \left\langle \psi_{lh}^{\ell} \middle| ex \middle| \psi_c^m \right\rangle = \left\langle u_{lh} \middle| ex \middle| u_c \right\rangle \left\langle \phi_v^{\ell} \middle| \phi_c^m \right\rangle = \frac{1}{\sqrt{6}} \langle S|ez|Z \rangle \int_{-\infty}^{+\infty} \phi_v^{\ell *}(z) \phi_c^m(z) dz \tag{3.52}$$

when the subband ℓ is light hole.

TM mode (y-propagation, field components H_x and E_z)

$$M_{\ell m} = \left\langle \psi_{lh}^{\ell} \middle| ez \middle| \psi_c^m \right\rangle = \left\langle u_{lh} \middle| ez \middle| u_c \right\rangle \left\langle \phi_v^{\ell} \middle| \phi_c^m \right\rangle = \frac{2}{\sqrt{6}} \langle S|ez|Z \rangle \int_{-\infty}^{+\infty} \phi_v^{\ell *}(z) \phi_c^m(z) dz,$$

(3.53)

when the subband ℓ is light hole. When the subband ℓ is heavy hole then $M_{\ell m}$=0.

As a summary we can remark that when the electric field is TE-polarised, transitions between the conduction band and both the heavy hole and light hole bands are allowed, while when it is TM-polarised, transitions only between the conduction and the light hole band are allowed.

3.7 Refractive index and absorption coefficients

In order to calculate the refractive index change Δn and the absorption coefficient α of a quantum well, the connection with the first order nonlinear susceptibility $\chi^{(1)}$ must be found. The electric displacement vector **D** is defined as,

$$\mathbf{D} = \varepsilon_0 \mathbf{E} + \mathbf{P} + \mathbf{P}_{transition} = \varepsilon \mathbf{E} + \varepsilon_0 \chi \mathbf{E}$$

(3.54)

where the polarisation has been seperated into two parts, $\mathbf{P}_{transition}$ the resonant component that is due to specific atomic transitions and **P** that includes all the other contributions to the polarisation. This expression can be rewritten as the product of a complex dielectric constant $\varepsilon'(\omega)$ and the electric field **E**,

$$\mathbf{D} = \varepsilon \left[1 + \frac{\varepsilon_0}{\varepsilon} \chi(\omega) \right] \mathbf{E} = \varepsilon'(\omega) \mathbf{E}$$

(3.55)

The dielectric constant $\varepsilon'(\omega)$ has been modified to include the effect of the atomic transitions. We consider a plane electromagnetic wave propagating in the y-direction inside the absorbing medium with dielectric constant $\varepsilon'(\omega)$. The wave has the form,

$$E(y,t) = \tilde{E}e^{-i(\omega t - k'y)} + \tilde{E}^* e^{i(\omega t + k'y)} = Re\left[\tilde{E}e^{-i(\omega t - k'y)}\right] \tag{3.56}$$

where k' is the complex propagation vector.

$$k' = \omega\sqrt{\mu\varepsilon'} \approx k\left[1 + \frac{\varepsilon_0}{2\varepsilon}\chi(\omega)\right], |\chi| << 1 \tag{3.57}$$

and

$$k = \omega\sqrt{\mu\varepsilon} \tag{3.58}$$

The linear optical susceptibility $\chi^{(1)}(\omega)$ can be expressed in terms of its real and imaginary parts $\chi^{(1)}(\omega)=\chi_r^{(1)}(\omega)+i\chi_i^{(1)}(\omega)$, and consequently the complex propagation vector can be separated into its real and imaginary parts,

$$k' \approx k\left[1 + \frac{\chi_r^{(1)}(\omega)}{2n^2}\right] + i\frac{k\chi_i^{(1)}(\omega)}{2n^2} \tag{3.59}$$

where $n=(\varepsilon/\varepsilon_0)^{1/2}$ is the index of refraction in the medium far from resonance. Substituting into the expression for the field (3.56) we find,

$$E(y,t) = Re\left[\tilde{E}e^{-[i\omega t - i(k+\Delta k)y + \alpha y]}\right] \tag{3.60}$$

The result of the polarisation due to atomic transitions is to change the phase delay by Δk and the refractive index by Δn,

$$\Delta k = \frac{k\chi_r^{(1)}(\omega)}{2n^2} \tag{3.61}$$

$$\boxed{\Delta n \approx \frac{\chi_r^{(1)}(\omega)}{2n} = \frac{\mathrm{Re}\left\{\chi^{(1)}(\omega)\right\}}{2n}} \tag{3.62}$$

and to cause the amplitude to vary exponentially with distance according to $e^{\alpha y}$, where,

$$\boxed{\alpha \approx -\frac{k\chi_i^{(1)}(\omega)}{2n^2} = -\frac{k\,\mathrm{Im}\left\{\chi^{(1)}(\omega)\right\}}{2n^2}} \tag{3.63}$$

Depending on the sign of α the amplitude will decrease exponentially, in other words the light will be absorbed or it will increase exponentially and in this case there is gain and light will be emitted. From expressions (3.62) and (3.63) the refractive index change and the absorption coefficient, that are due to the atomic transitions between the quantized energy levels of a semiconductor quantum well, can be calculated.

3.8 Numerical results and discussion

From the expressions derived in the previous sections, the linear absorption (or gain) and the refractive index change can be calculated for different semiconductor quantum wells. In this section we will confine our attention to the optical properties of symmetric GaAs-$Ga_{1-x}Al_xAs$ quantum wells, while in the following chapters we will consider disordered and asymmetric quantum wells.

Quantum well structures have attracted considerable attention because of their superior characteristics, both for active and passive applications, compared to the bulk

semiconductor material. For this reason a lot of the theoretical work has been concentrated in calculating the absorption (or gain) [16]-[17] and refractive index [18]-[19] spectral characteristics. The variation of these characteristics with respect to the carrier density, as well as the application of an electric field perpendicular to the quantum well interface have been studied. The theoretical calculations were found to be in close agreement with the available experimental data [20]. In the numerical calculations presented in this chapter, the spectral characteristics and the polarisation dependence will be evaluated for various cases and the results obtained will be compared with the previous theoretical work.

The following parameters will be assumed in the numerical calculations: the Luttinger parameters for $Ga_{1-x}Al_xAs$ γ_1=6.85–3.4x, γ_2=2.1–1.42x and γ_3=2.9–1.61x, the effective mass for the conduction band $m_c^*=(0.067+0.058x)m_o$ and the linewidth parameter of the density matrix formalism $\gamma_{m\ell}$=0.007eV corresponding to a dephasing time τ_d=60fs. This value for τ_d was estimated in Ref.[20] by fitting the theoretical into the experimental data and was found to be for a GaAs/$Ga_{1-x}Al_xAs$ quantum well almost the same as that of bulk GaAs.

In figure 3.2 and 3.3 the absorption coefficients for TE and TM polarisation for a GaAs-$Ga_{0.75}Al_{0.25}As$ quantum well with 100Å well width is presented, for different carrier densities. By increasing the carrier density the absorption coefficient α from negative becomes positive and in this case there is gain. The gain profile is broadened and reduced due to the dephasing mechanisms. In figure 3.4 and 3.5 the refractive index change Δn for the same structure is calculated, with respect to the refractive index of the barrier material $Ga_{1-x}Al_xAs$. Depending on the positive or negative increment of the refractive index the quantum well region will result in guidance or antiguidance and defocusing of the optical mode. The refractive index change is negative for both the TE and TM modes. The peaks observed in the spectra of the linear optical coefficients originate from the hh1-c1 optical

transition for the TE mode and the lh1-c1 optical transition for the TM mode, but because of the band non-parabolicity the contributions from the other transitions are substantial. From the interband selection rules the heavy hole→electron transitions are three times more intense than the light hole→electron transitions and as expected the gain for the TE is larger than the gain for the TM mode. The refractive index change is more negative for the TM mode than the TE mode and this could result in TM suppression in the guiding structure.

In figures 3.6-3.9 the absorption coefficient and the refractive index change for the same quantum well with carrier concentration $n=1.0\times10^{18}/cm^3$ calculated from the valence band mixing model are compared with the coefficients calculated from the diagonal approximation. It can be seen that the diagonal approximation predicts higher absorption coefficient and refractive index change than the valence band mixing model. This is because, for a fixed carrier density, non-parabolic energy bands give a higher quasi-Fermi level for holes than parabolic bands [18].

In figures 3.10-3.13 the gain coefficient and the refractive index change is calculated for the quantum well with respect to an applied electric field F perpendicular to the quantum well interface. The carrier concentration is set to be constant $n=4.0\times10^{18}/cm^3$. The peak gain shifts to a lower energy region (red shift) and the magnitude of the peak decreases as the applied electric field increases. This is due to the reduction of the magnitude of the dipole moment with the applied electric field [21]. As the electrons and holes are pulled apart the overlap integral between electron and hole wavefunctions decreases, resulting in a reduction of the peak gain as well as an increase in the magnitude of the refractive index change. Another important point following the application of the electric field, is that the transitions that were forbidden, because of the symmetry selection rules, become allowed, since their wavefunctions are no longer symmetric and as a consequence the overlap integrals are no longer zero.

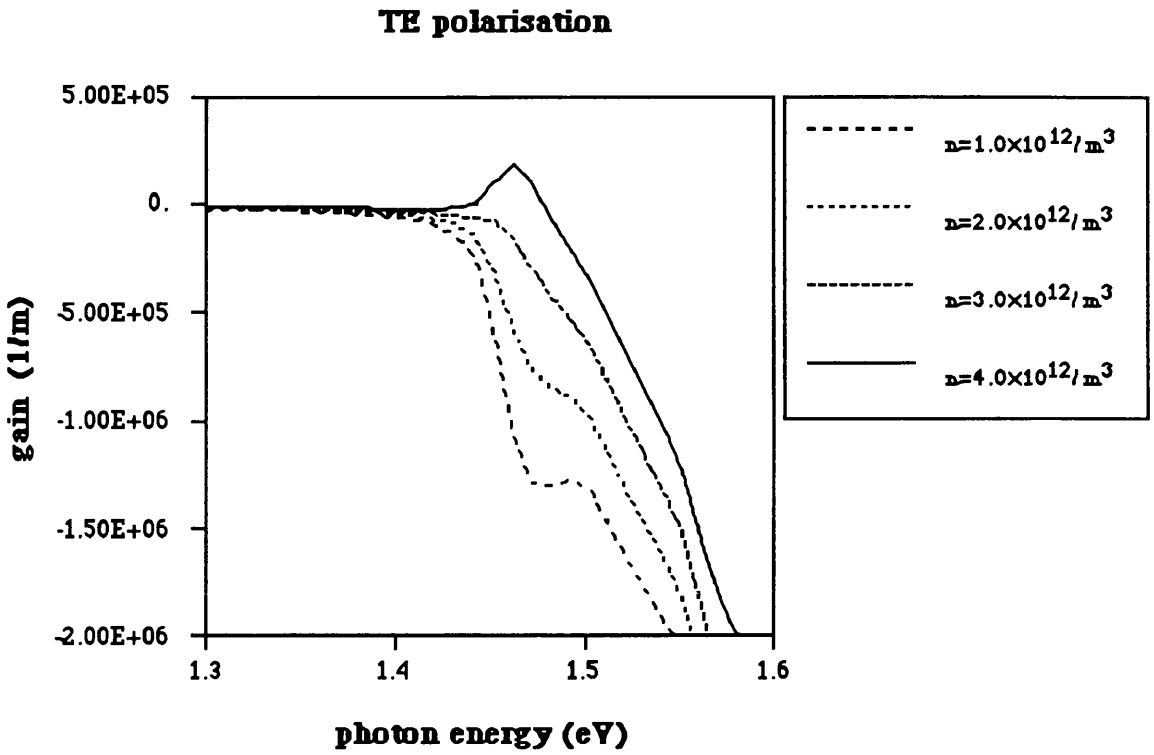

Figure 3.2. Absorption spectra for a 100Å GaAs-$Ga_{0.75}Al_{0.25}As$ for the TE polarisation for various carrier densities

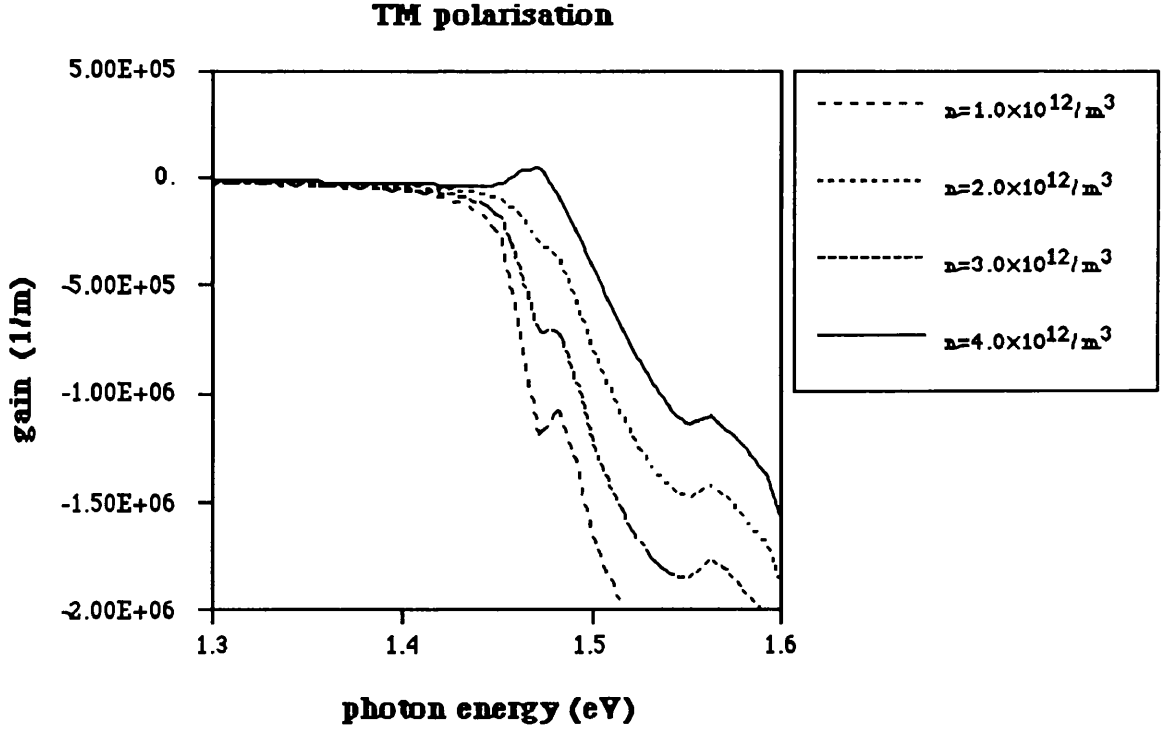

Figure 3.3. Absorption spectra for a 100Å GaAs-$Ga_{0.75}Al_{0.25}As$ for the TM polarisation for various carrier densities

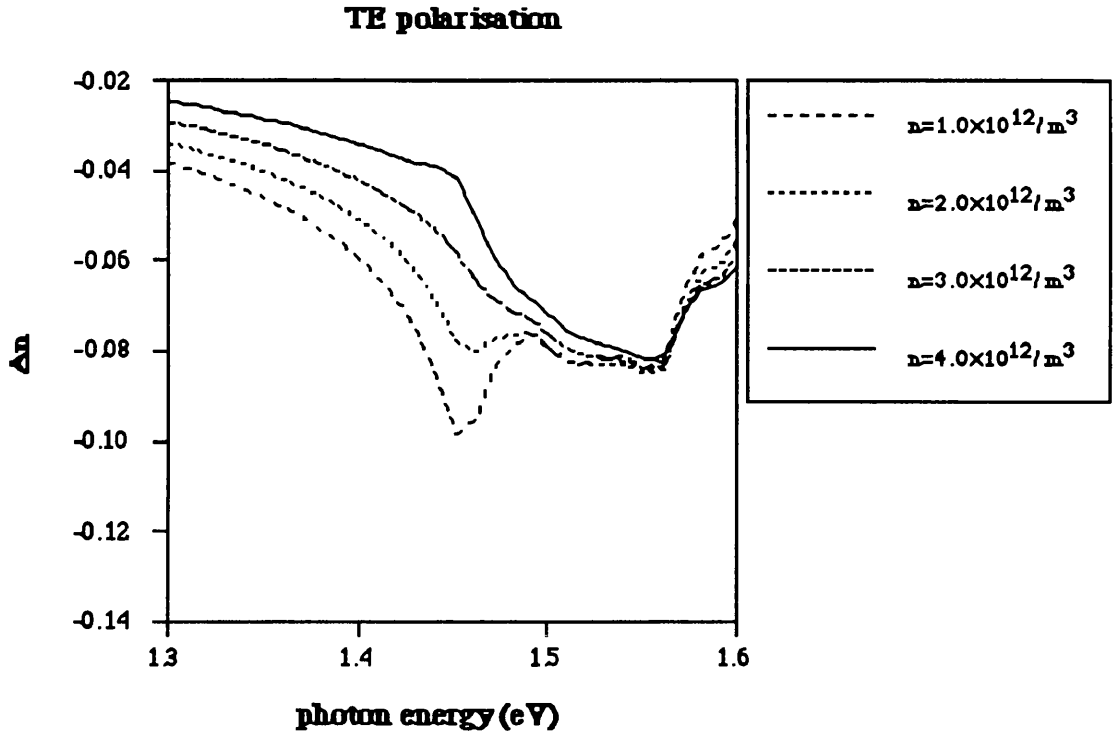

Figure 3.4. Refractive index change for a 100Å GaAs-$Ga_{0.75}Al_{0.25}As$ for the TE polarisation for various carrier densities

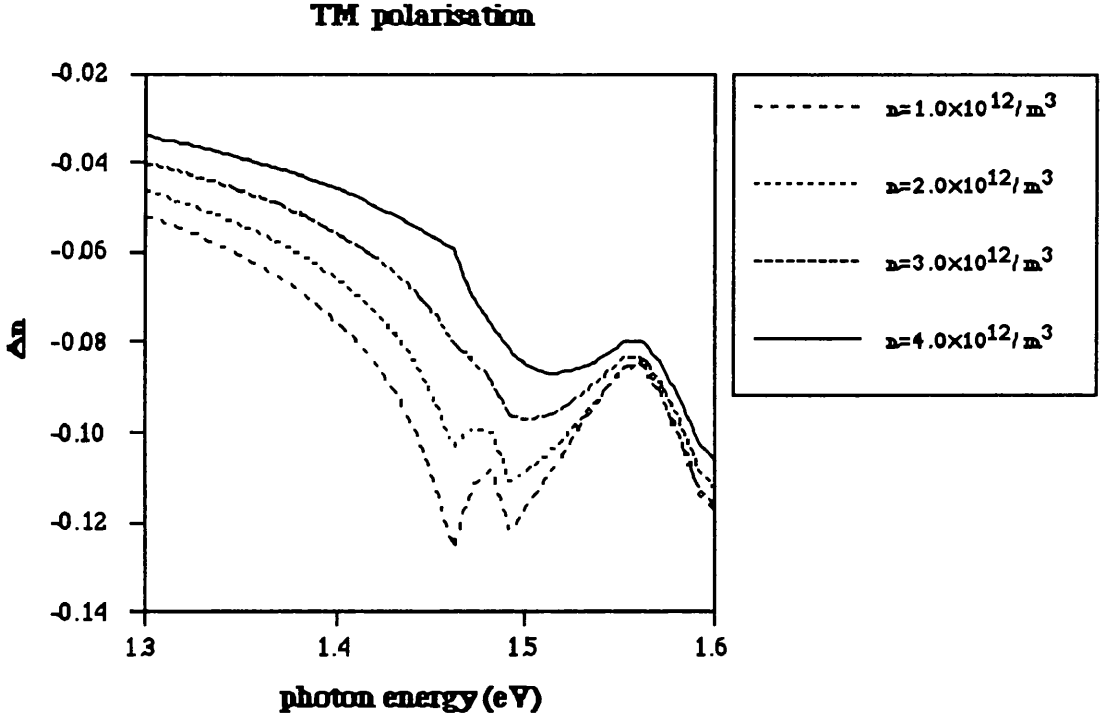

Figure 3.5. Refractive index change for a 100Å GaAs-$Ga_{0.75}Al_{0.25}As$ for the TM polarisation for various carrier densities

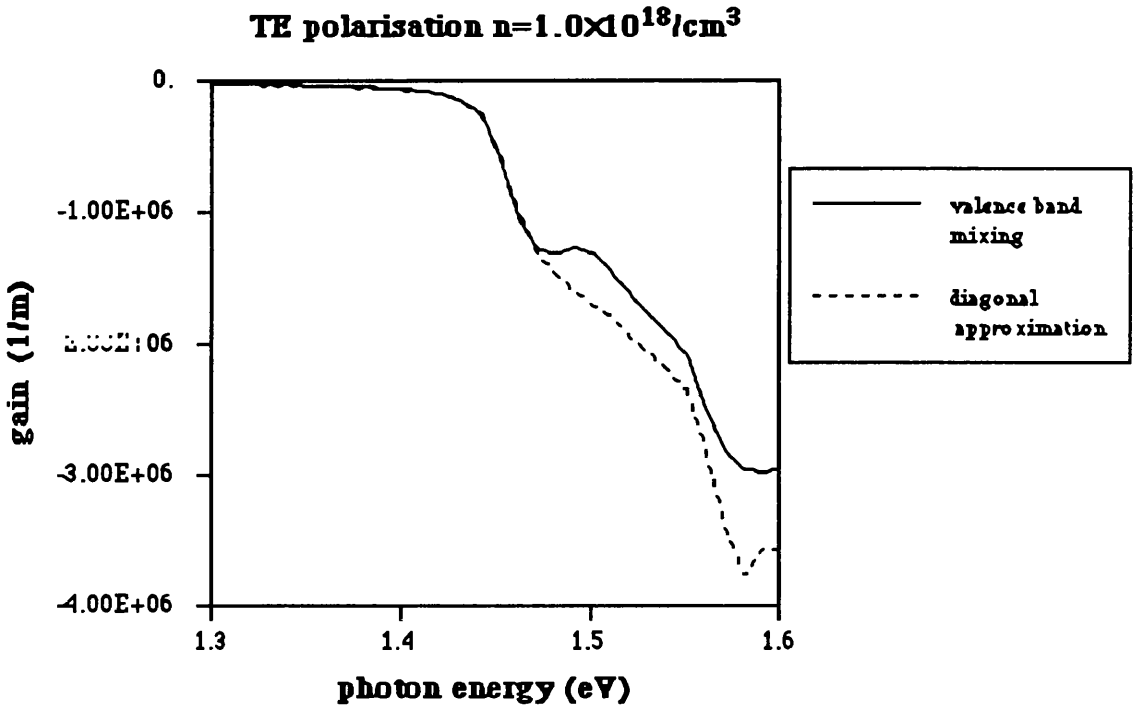

Figure 3.6. Comparison of the absorption spectra for a 100Å GaAs-$Ga_{0.75}Al_{0.25}As$ for the TE polarisation, for $n=1.0\times10^{18}/cm^3$, obtained from the diagonal approximation and the valence band mixing method

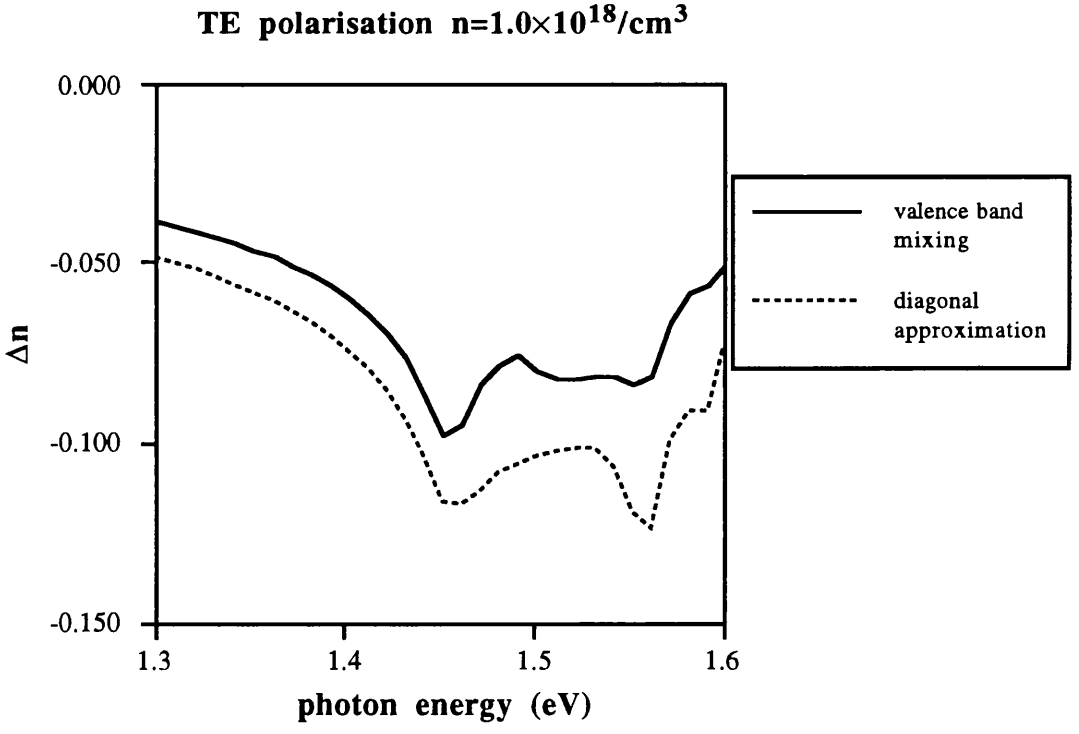

Figure 3.7. Comparison of the refractive index change for a 100Å GaAs-$Ga_{0.75}Al_{0.25}As$ for the TE polarisation, for $n=1.0\times10^{18}/cm^3$, obtained from the diagonal approximation and the valence band mixing method

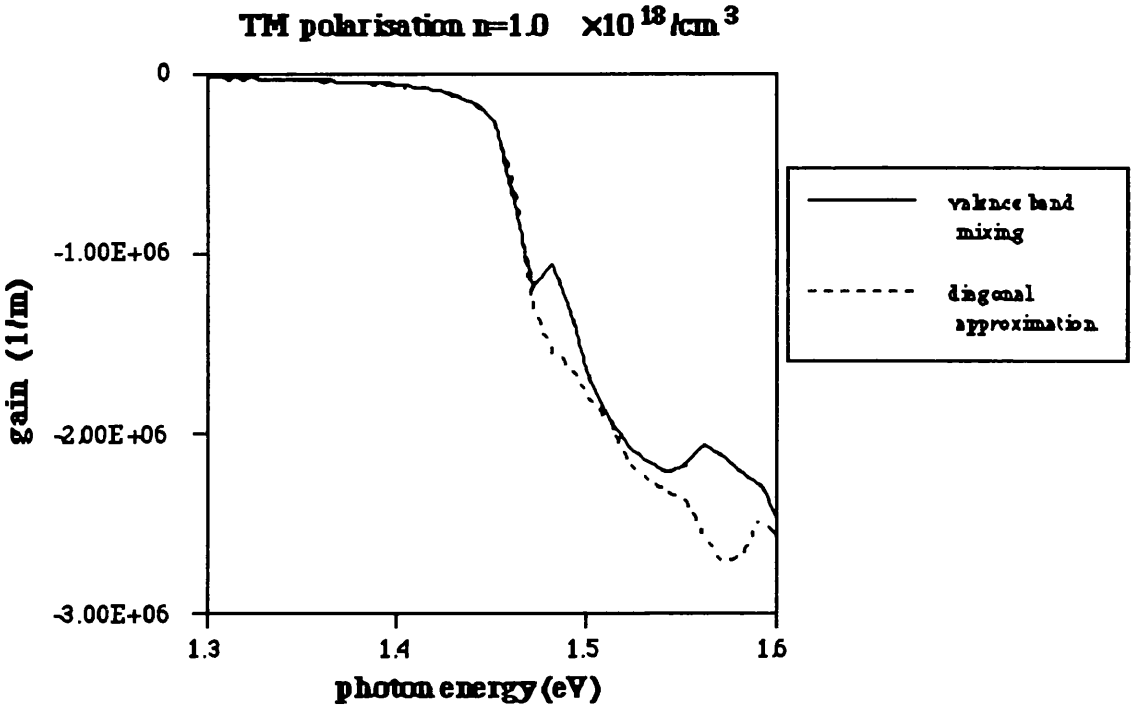

Figure 3.8. Comparison of the absorption spectra for a 100Å GaAs-$Ga_{0.75}Al_{0.25}As$ for the TM polarisation, for $n=1.0\times10^{18}/cm^3$, obtained from the diagonal approximation and the valence band mixing method

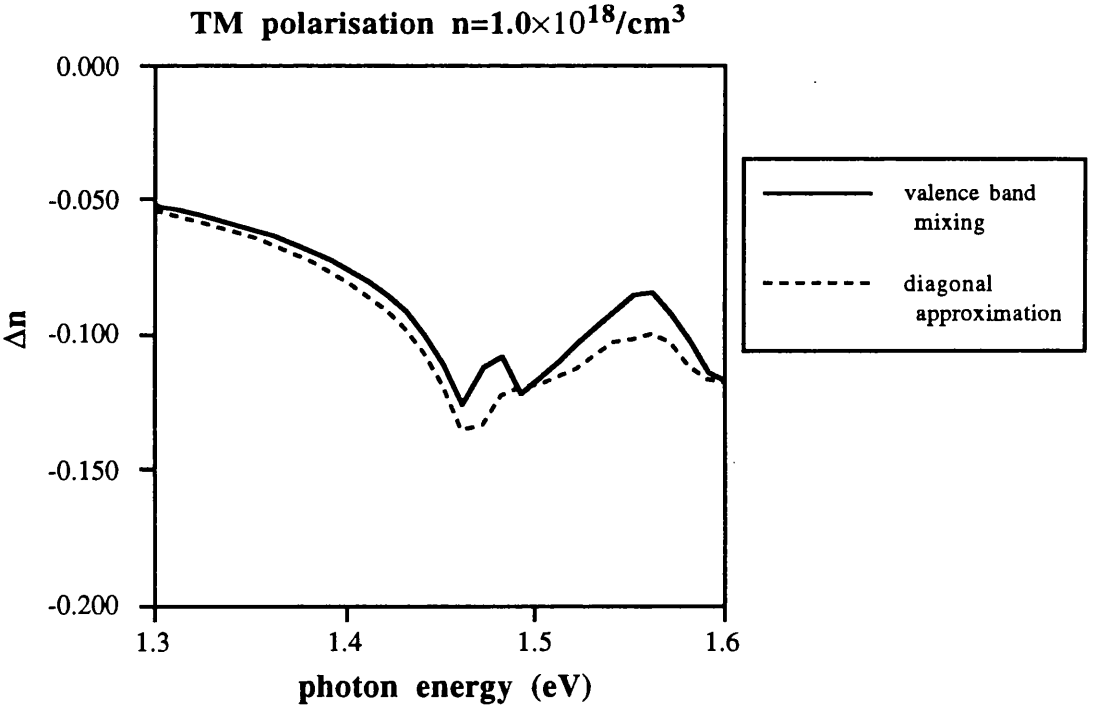

Figure 3.9. Comparison of the refractive index change for a 100Å GaAs-$Ga_{0.75}Al_{0.25}As$ for the TM polarisation, for $n=1.0\times10^{18}/cm^3$, obtained from the diagonal approximation and the valence band mixing method

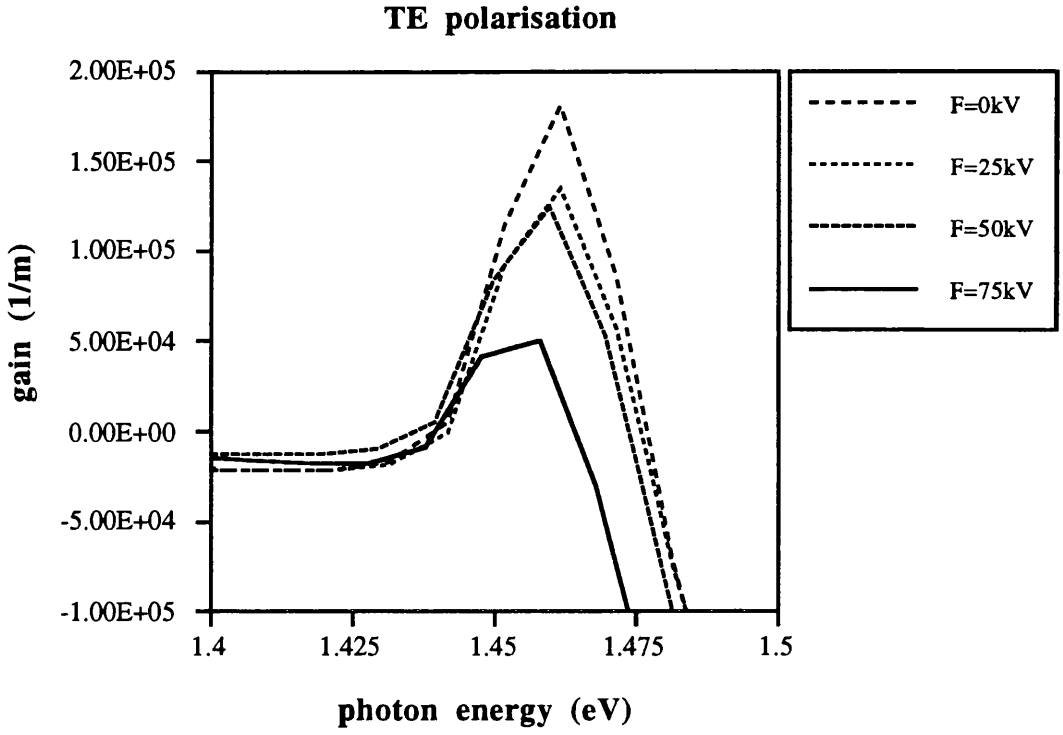

Figure 3.10. Gain spectra for a 100Å GaAs-$Ga_{0.75}Al_{0.25}As$ for the TE polarisation for various applied electric fields

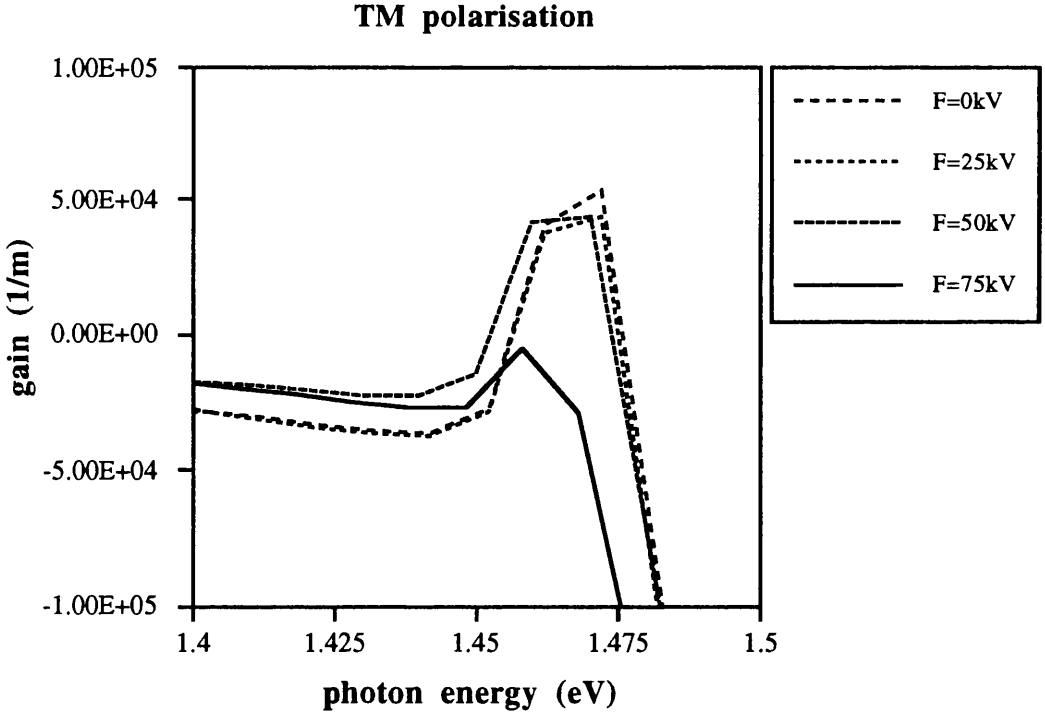

Figure 3.11. Gain spectra for a 100Å GaAs-$Ga_{0.75}Al_{0.25}As$ for the TM polarisation for various applied electric fields

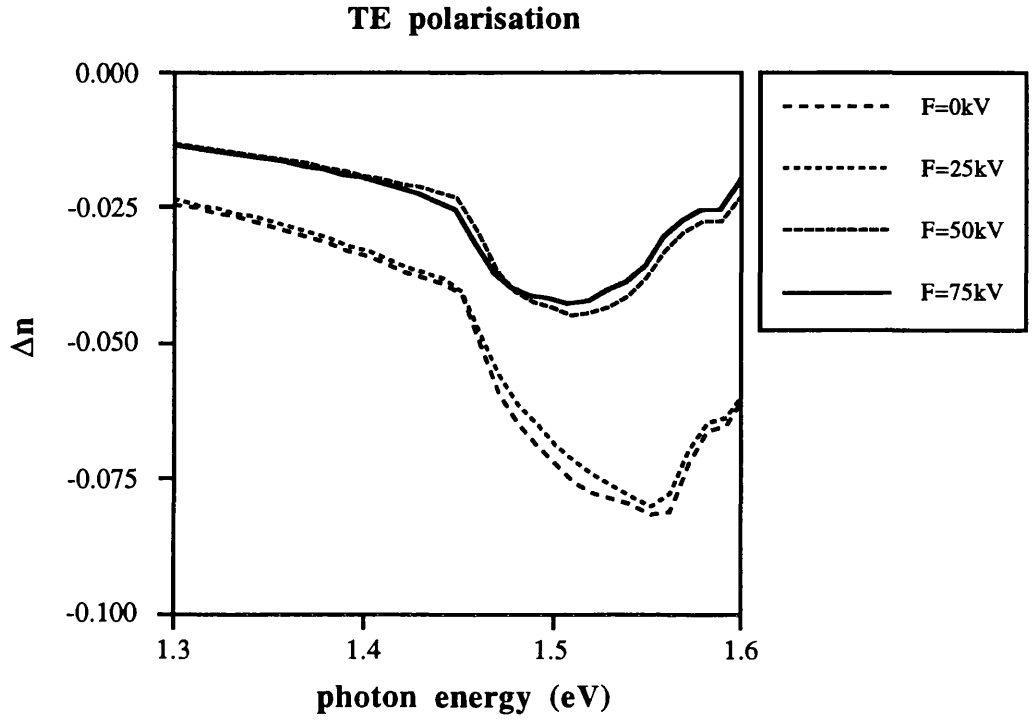

Figure 3.12. Refractive index change for a 100Å GaAs-$Ga_{0.75}Al_{0.25}As$ for the TE polarisation for various applied electric fields

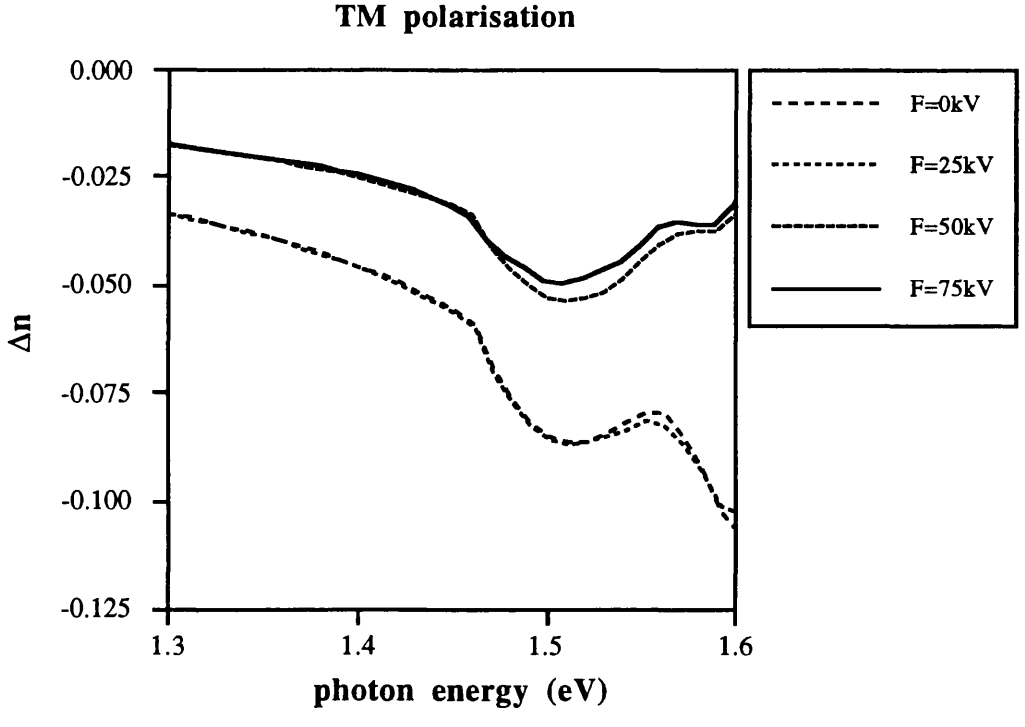

Figure 3.13. Refractive index change for a 100Å GaAs-$Ga_{0.75}Al_{0.25}As$ for the TM polarisation for various applied electric fields

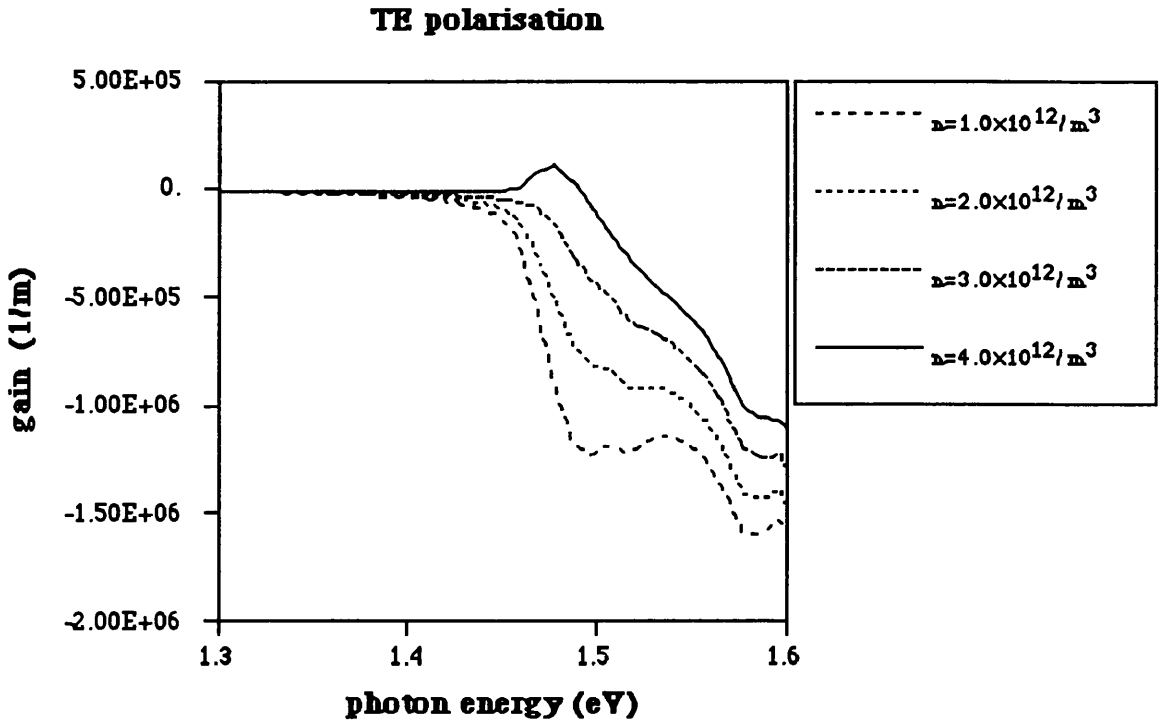

Figure 3.14. Absorption spectra for a 80Å GaAs-$Ga_{0.7}Al_{0.3}As$ for the TE polarisation for various carrier densities

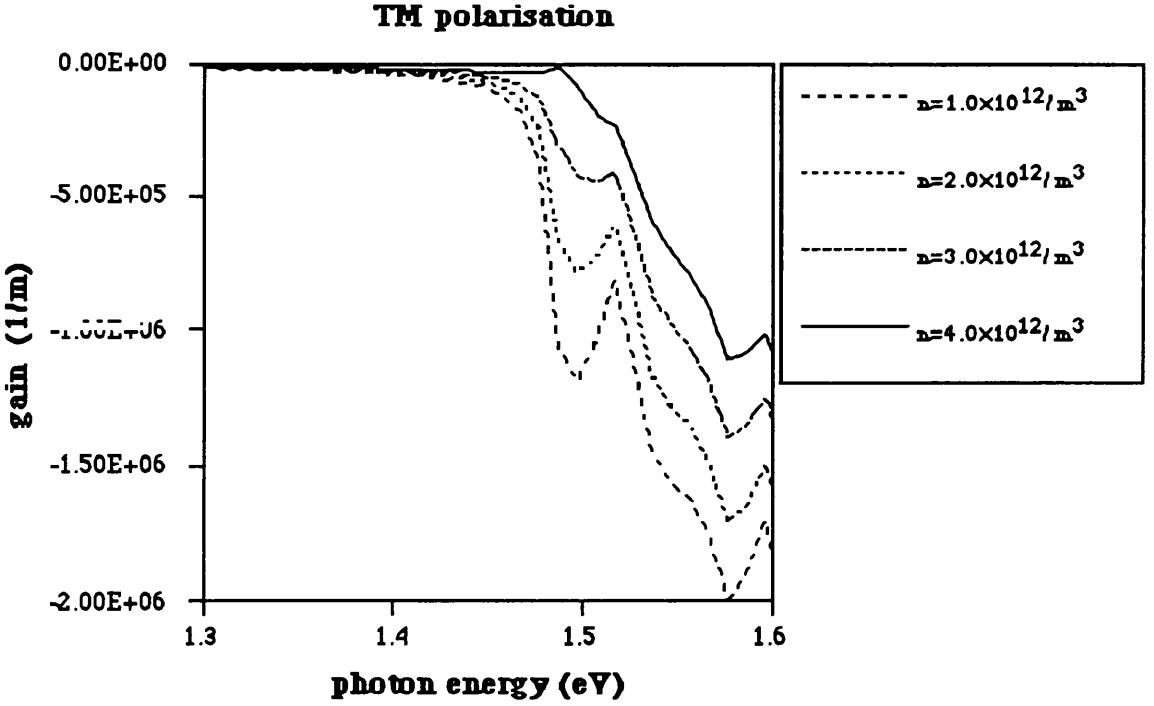

Figure 3.15. Absorption spectra for a 80Å GaAs-$Ga_{0.7}Al_{0.3}As$ for the TE polarisation for various carrier densities

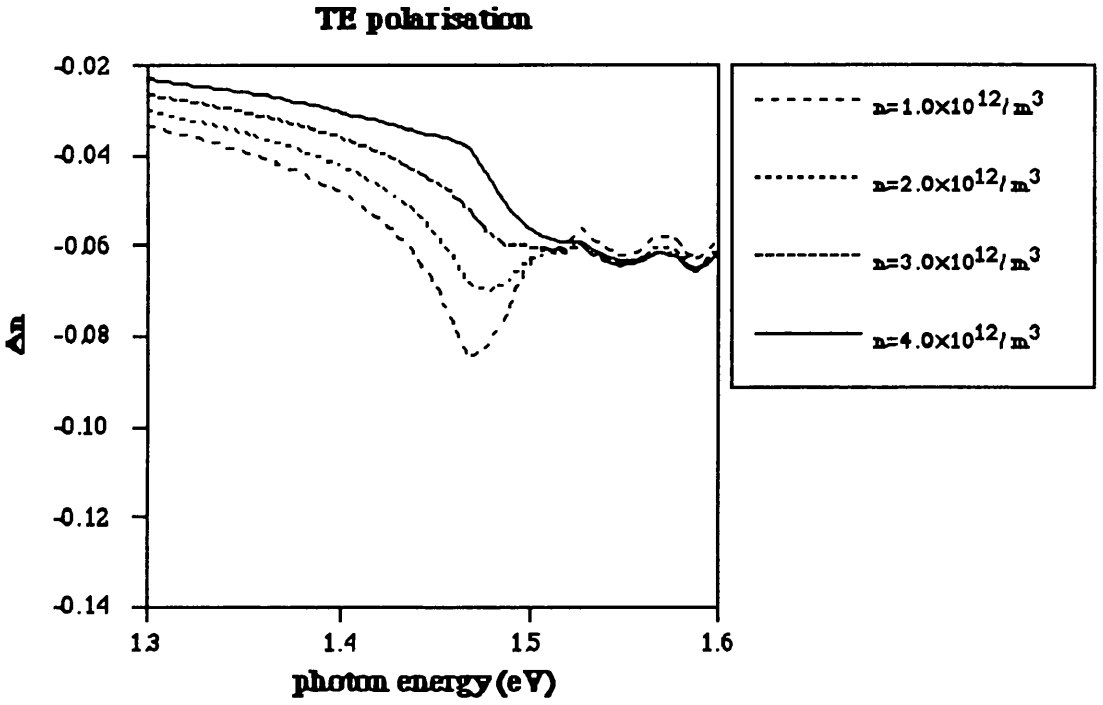

Figure 3.16. Refractive index change for a 80Å GaAs-$Ga_{0.7}Al_{0.3}As$ for the TE polarisation for various carrier densities

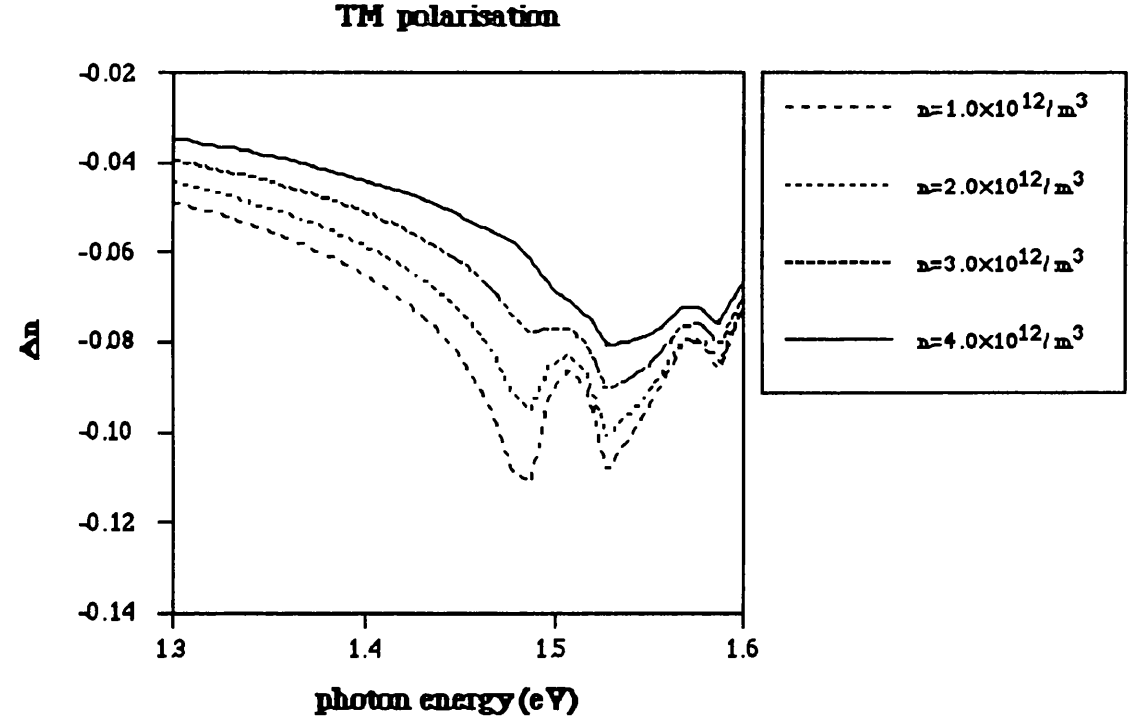

Figure 3.17. Refractive index change for a 80Å GaAs-$Ga_{0.7}Al_{0.3}As$ for the TM polarisation for various carrier densities

In figures 3.14-3.17 the absorption coefficient and the refractive index change are calculated for an 80Å GaAs-$Ga_{0.7}Al_{0.3}As$ square quantum well for different carrier densities. Comparing with the optical constants in figures 3.2-3.5 for the 100Å GaAs-$Ga_{0.75}Al_{0.25}As$ quantum well, we can observe a shift of the peak gain (or absorption edge) to higher energies. This is due to the fact the 80Å well is deeper and narrower and so the bandgap edge is higher. There is also a reduction of the peak gain for the 80Å well compared to the 100Å well with the same carrier density, as well as a reduction of the peak refractive index change.

The numerical results presented in this section can be compared with those obtained from previous theoretical work [17]-[19]. The data for the absorption coefficient and the refractive index change for the square quantum well are in close agreement with the previously published data. The injected carrier density and the applied electric field, without free-carrier screening [22], were found to have the same effect on the optical properties of the semiconductor quantum well as the previous theoretical and experimental work have suggested. The density matrix formalism and the multiband effective mass theory, on which our analysis was based on, are useful tools to describe the optical properties of semiconductor structures. The same analysis will be used in the following sections in order to calculate the optical properties of different structures, disordered quantum wells and asymmetric quantum wells.

3.9 Conclusions

In this chapter the density matrix formalism was presented as a method for obtaining expressions for the optical susceptibilities of semiconductor quantum wells. Based on this method expressions for the linear and the second-order nonlinear optical properties were derived. Numerical results for the absorption α and the refractive index change Δn were

obtained taking into account the band calculations from the previous chapter including valence band mixing. The results were found to be in close agreement with the previously published data and the method enabled us to estimate adequately the effect of increasing the carrier density and the effect of an external applied electric field.

References

[1] W.E. Lamb, *Theory of an optical maser*, Phys. Review A, vol. **134**, pp. 1429-1450, 1964

[2] M. Bloembergen, *Nonlinear Optics*, (W.A. Benjamin Inc., 1965) Chapter 2

[3] R.H Pantell and H.E. Puthoff, *Fundamentals of quantum electronics*, (John Wiley & Sons, 1969) Chapter 2

[4] J. Ducuing and C.Flytzanis, in *Optical properties of solids*, edited by F. Abelès (North-Holland Publishing Company, 1972) Chapter 11, pp. 863-889

[5] D. Marcuse, *Principles of quantum electronics*, (Academic Press, 1980) Chapter 7

[6] M. Yamada, Y. Suematsu, *Analysis of gain suppression in undoped injection lasers*, J. Appl. Phys., vol **52**, pp. 2653-2664, 1980

[7] A. Yariv, *Quantum Electronics*, (John Wiley & Sons, 1989) Chapter 3

[8] P.N. Butcher and D. Cotter, *The elements of nonlinear optics*, (Cambridge University Press, 1990) Chapter 4

[9] D. Ahn and S.L. Chuang, *Calculation of linear and nonlinear intersubband optical absorptions in a quantum well model with an applied electric field*, IEEE J. of Quant. Elec., vol. **23**, pp. 2196-2204, 1987

[10] L. Tsang, D. Ahn and S.L. Chuang, *Electric field control of optical second-harmonic generation in a quantum well*, Appl. Phys. Lett., vol. **52**, pp. 697-699, 1988

[11] M. Yamada, *Theoretical analysis of nonlinear optical phenomena taking into account the beating vibration of the electron density in semiconductor lasers*, J. Appl. Phys., vol **66**, pp. 81-89, 1989

[12] P. Hlawiczka, *Introduction to quantum electronics*, (Academic Press, 1971), Chapter 3

[13] M. Asada, A Kameyama and Y. Suematsu, *Gain and intervalence band absorption in quantum-well lasers*, IEEE J. of Quant. Elec., vol. **20**, pp. 745-753, 1984

[14] E.O. Kane, *Band structure of indium antimonide*, J. Phys. Chem. Solids, vol. **1**, pp. 249-261, 1957

[15] G. Bastard, *Wave mechanics applied to semiconductor heterostructures*, (Lés Édition de Physique, Halsted Press, 1988), Chapter 3

[16] M. Asada and Y. Suematsu, *Density-matrix theory of semiconductor lasers with relaxation broadening model-Gain and gain-suppression in semiconductor lasers*, IEEE J. of Quant. Elec., vol. **21**, pp. 434-441, 1985

[17] D. Ahn and S.L. Chuang, *Optical gain and gain suppression of quantum-well lasers with valence band mixing*, IEEE J. of Quant. Elec., vol. **26**, pp. 13-23, 1990

[18 D. Ahn and S.L. Chuang, *Valence-band mixing effects on the gain and the refractive index change of quantum-well lasers*, J. Appl. Phys., vol. **64**, pp. 4056-4064, 1988

[19] K. Nakamura, A. Shimizu, K. Fujii, M. Koshiba, *Numerical analysis of the absorption and the refractive index change in arbitrary semiconductor quantum-well structures*, IEEE J. of Quant. Elec., vol. **28**, pp. 1670-1676, 1992

[20] M. Yamada, S. Ogita, M. Yamagishi and K. Tabata, *Anisotropy and broadening of optical gain in a GaAs/AlGaAs multiquantum-well laser*, IEEE J. of Quant. Elec., vol. **21**, pp. 640-645, 1985

[21] E.J. Roan and S.L. Chuang, *Linear and nonlinear intersubband electroabsorptions in a modulation-doped quantum well*, J. Appl. Phys., vol. **69**, pp. 3249-3260, 1991

[22] D. Ahn and S.L. Chuang, *Model of the field-effect quantum-well laser with free-carrier screening and valence band mixing*, J. Appl. Phys., vol **64**, pp. 6143-6149, 1988

4 Disordered Quantum Wells

4.1 Introduction

The potential advantages of monolithic integration of several optoelectronic devices in photonic integrated circuits and optoelectronic integrated circuits have attracted considerable interest world-wide. Several approaches to integration based on quantum well layers have been suggested. One approach requires many steps of etching and regrowth, an other is to vary the width of the quantum wells across the wafer during a single stage of epitaxy. Recently quantum well *disordering* (*intermixing*) is also emerging as a powerful technique because it allows for the possibility of lateral patterning of the band structure of heterostructure material. In the disordering processes the bandgap of the quantum well structures is modified, in selected regions, by intermixing the wells with the barriers to form an alloy semiconductor. The bandgap of the intermixed regions is usually larger than that of the original quantum well leading to a reduction in the propagation loss at the initial position of the absorption edge and a modification of the refractive index. Taking advantage of these properties, a number of potential applications of the disordering technique in integrated optoelectronics are possible: low-loss waveguides for interconnecting components on an optoelectronic integrated circuit, extended-cavity narrow-linewidth lasers, nonabsorbing mirrors, single-frequency distributed Bragg

reflection (DBR) lasers, gratings formed through changes in the refractive index, distributed feedback (DFB) gain and phase gratings and others (figure 4.1) [1]-[6].

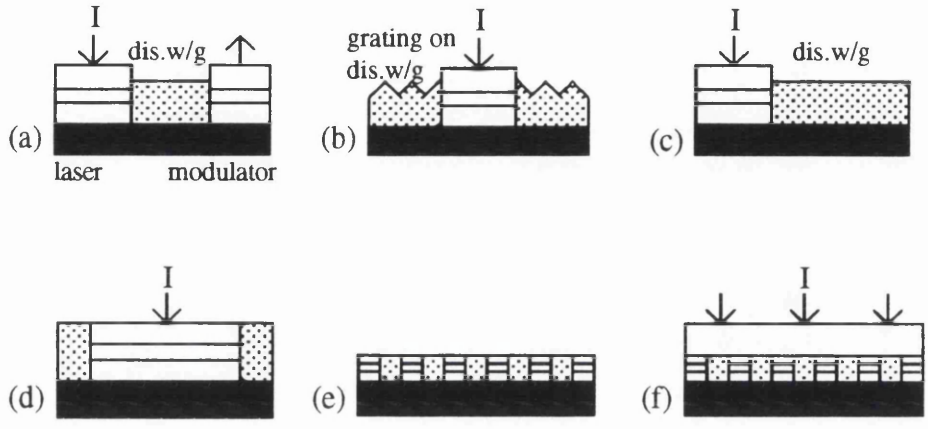

Figure 4.1. Examples of the potential applications of disordered devices for coherent optics (a)integrated laser and modulator, (b)DBR laser, (c)extended-cavity narrow-linewidth laser, (d)high-power laser with non-absorbing mirrors, (e)grating formed by disordering, (f)DFB laser with index and gain gratings.

A number of disordering techniques are been considered for the fabrication of integrated devices, particularly *impurity induced disordering* (IID), *impurity-free vacancy disordering using dielectric caps* and *laser-induced disordering*. The technique selected will depend on the material system and the application and it should satisfy the following requirements; high crystal quality, low free-carrier concentration and low optical propagation losses. Quantum well disordering has mainly been achieved by IID. In IID processes an impurity is introduced into an epitaxial wafer and the wafer is then annealed. During annealing the layers intermix and ion-implantation damage is to a large extent removed. A number of species have been demonstrated to disorder the GaAs/AlGaAs system; active dopands Zn, Si [7]-[8] and neutral dopands Al, F, B [9]-[10]. Total propagation losses as low as 4.6dB cm^{-1} were obtained for the case of fluorine in addition to a 40meV blue shift in the absorption edge and a refractive index change of 0.036 for the TE and 0.021 for the TM polarisation [11]. IID is not suitable for bandgap-tuned modulators and lasers because of

residual damage and traps associated with the implanted species. Impurity-free vacancy disordering is based on creating vacancies in semiconductor materials with the use of dielectric caps. With this technique large bandgap energy shifts are possible without the drawbacks of IID, but has poor reproducibility and poor discrimination between the areas in which disordering is desired and those in which it is not. In laser induced disordering a beam is focused and scanned across the semiconductor surface, melting the semiconductor layers, which recrystallise as an alloy semiconductor. This method has the advantage of being impurity-free and offers the possibility of direct-write, but the quality of the recrystallised material is inferior to the original and the process cannot be controlled to give partial disordering [12].

4.2 Disordered quantum well potential profiles

The design of optoelectronic integrated devices relies on understanding the influence of the intermixing process on the optical properties of the quantum well structures. Disordering results in the transition from an initially square well compositional profile to a gradually graded profile. The compositional profile will determine the potential energy profile confining the carriers and hence the energy shifts and the optical properties. The mechanism by which atoms intermix in III-V quantum well structures varies with the technique used and in general it is not clear at present. Recent progresses in understanding the diffusion mechanism of GaAs/AlGaAs heterostructures, based on experimental results, suggest that it depends on doping, the group V (Al) element vapour pressure and point defect nonequilibrium concentrations, which may be induced by a chemical or a physical process. The doping influences the concentrations of charged point defect species, which in turn influence the diffusivities of the appropriate atoms that utilise the charged point defect species as diffusion vehicles. The group V element vapour pressure effects the compound crystal composition as well as the point defect thermal equilibrium. A

nonequilibrium point defect concentration may also be impurity induced, by diffusion or by ion-implantation [13]-[14].

For the one-dimensional case, a phenomenological description of the diffusion process is given by the flux equation, Fick's first law,

$$j = -D\frac{\partial C}{\partial z} \tag{4.1}$$

and the diffusion equation, Fick's second law,

$$\frac{\partial C}{\partial t} = \frac{\partial}{\partial z}\left[D\frac{\partial C}{\partial z}\right] \tag{4.2}$$

where j is the flux, D is the diffusivity, C the concentration of the diffusing species and z the spatial coordinate. Diffusion phenomena, that are characterised with a constant diffusion coefficient D, have as analytical solutions series of error functions or trigonometrical series, depending on the pattern of the source diffusing [15]-[16].

In order to study the disordering process of quantum well structures, a GaAs/AlGaAs single quantum well with infinite barriers modified by intermixing will be analysed. The diffusion model employed assumes that the excess aluminium concentration in the barrier regions diffuses into the well, accompanied by the out-diffusion of gallium. The diffusion coefficients of Al and Ga are set to be equal and constant and independent of their concentrations throughout the intermixing process. During the first stages of intermixing the composition of the materials around the well and barrier interfaces are only slightly modified from a rectangular shape and can be considered to be partially disordered. After a sufficient time the well and barrier regions will be totally intermixed with loss of quantum confinement effects, resulting in a bulk-like alloy semiconductor. From Fick's second law

(4.2) the Al concentration $C_{Al}(z,t)$ can be expressed at the different stages of the disordering process as a sum of error functions,

$$C_{Al}(z,t) = C_o\left\{1-\frac{1}{2}\left[\mathrm{erf}\left(\frac{h-z}{2\sqrt{Dt}}\right)+\mathrm{erf}\left(\frac{h+z}{2\sqrt{Dt}}\right)\right]\right\} \tag{4.3}$$

where C_0 is the initial square quantum well Al concentration of the barrier material, $h=L_z/2$ and L_z is the square well width (figure 4.2). The extent of the disordering process is characterised by the product of the diffusion coefficient with time *Dt*. The square root $(Dt)^{1/2}$ is defined by many researchers as the diffusion length L_d, since it is expressed in units of length. At the first stages of intermixing $Dt\rightarrow 0$, while $Dt\rightarrow\infty$ corresponds to a fully disordered quantum well. The band gap of the disordered quantum well $E_g(z,t)$ at distance z from the centre of the well (z=0) can be evaluated from the expression (2.37) for the energy gap with respect to the Al concentration $C_{Al}(z,t)$,

$$E_g(z,t)=E_{g\text{-}GaAs}+1.04\cdot C_{Al}(z,t)+ 0.47\cdot[C_{Al}(z,t)]^2 \quad (eV) \tag{4.4}$$

where $E_{g\text{-}GaAs}$ is the energy gap of GaAs and it is equal to 1.42eV at room temperature. The conduction and valence band discontinuities Q_c and Q_v, that determine the conduction and valence band potential profile are assumed to be equal to 57% and 43% of the gap difference respectively. The potential profiles for the conduction and valence band after t time of diffusion with diffusion constant D are equal to,

$$V_c(z,t)=E_g(0,t)+Q_c[E_g(\infty,t)-E_g(0,t)] \tag{4.5a}$$

$$V_v(z,t)=Q_v[E_g(0,t)-E_g(\infty,t)] \tag{4.5b}$$

where the 0 energy level is taken to be the top of the valence band.

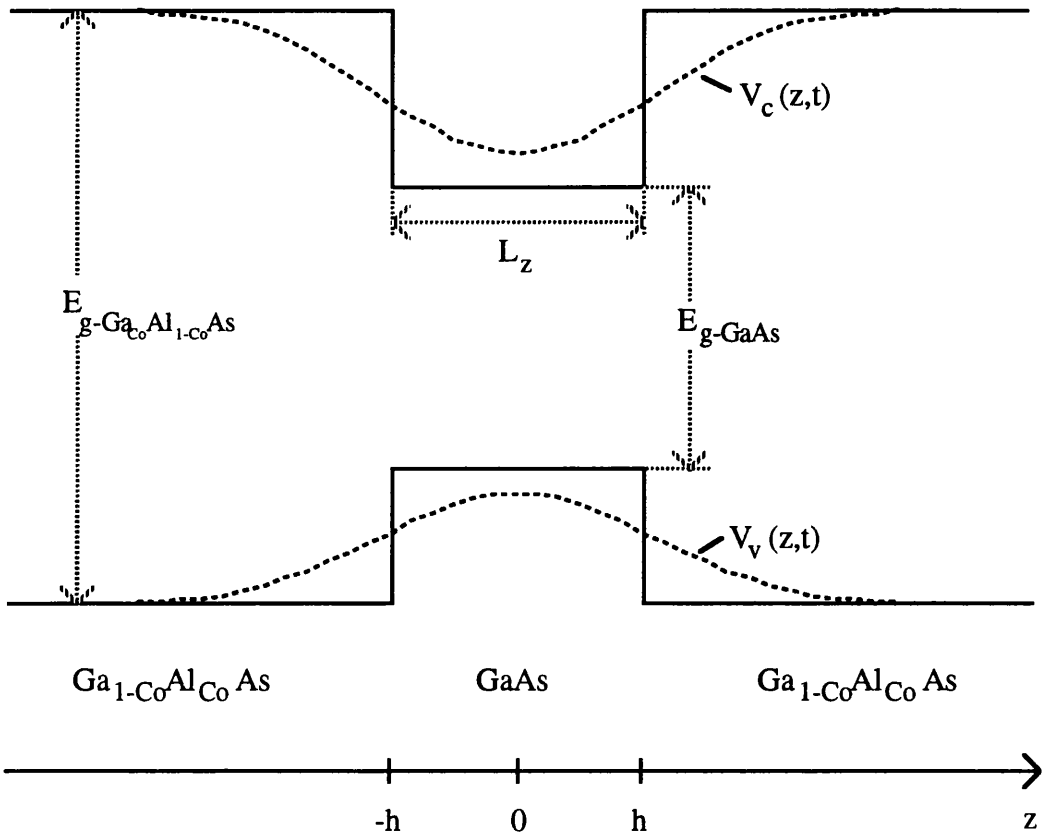

Figure 4.2. Confinement potential profile as a function of the growth z-axis for a square quantum well (solid line) and a disordered quantum well (dashed line) with some of their parameters indicated.

The conduction band potential profile for a 10nm GaAs-$Ga_{0.7}Al_{0.3}As$ calculated from expressions (4.3) and (4.5a) for different stages of the disordering process is shown in figure 4.3. For short diffusion times the disordered quantum well potential profile resembles that of the square quantum well, while for long diffusion times the potential profile becomes flat and bulk-like.

Another model suitable for the determination of the properties of disordered quantum wells that has been suggested is the *hyperbolic secant model* [17]-[19]. According to this model the potential profile of a quantum well at the different stages the disordering process can be expressed as,

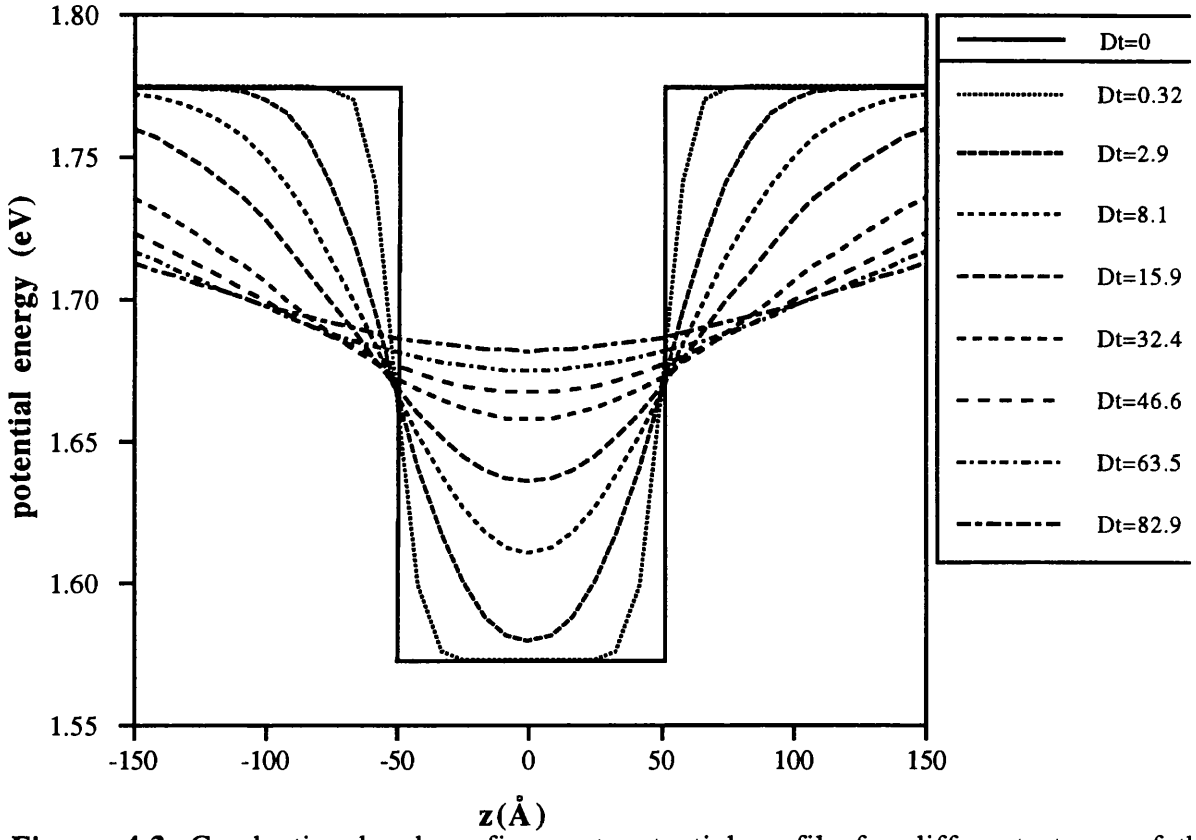

Figure 4.3. Conduction band confinement potential profile for different stages of tl disordering process as a function of the growth z-axis (Dt is expressed in units of nm^2).

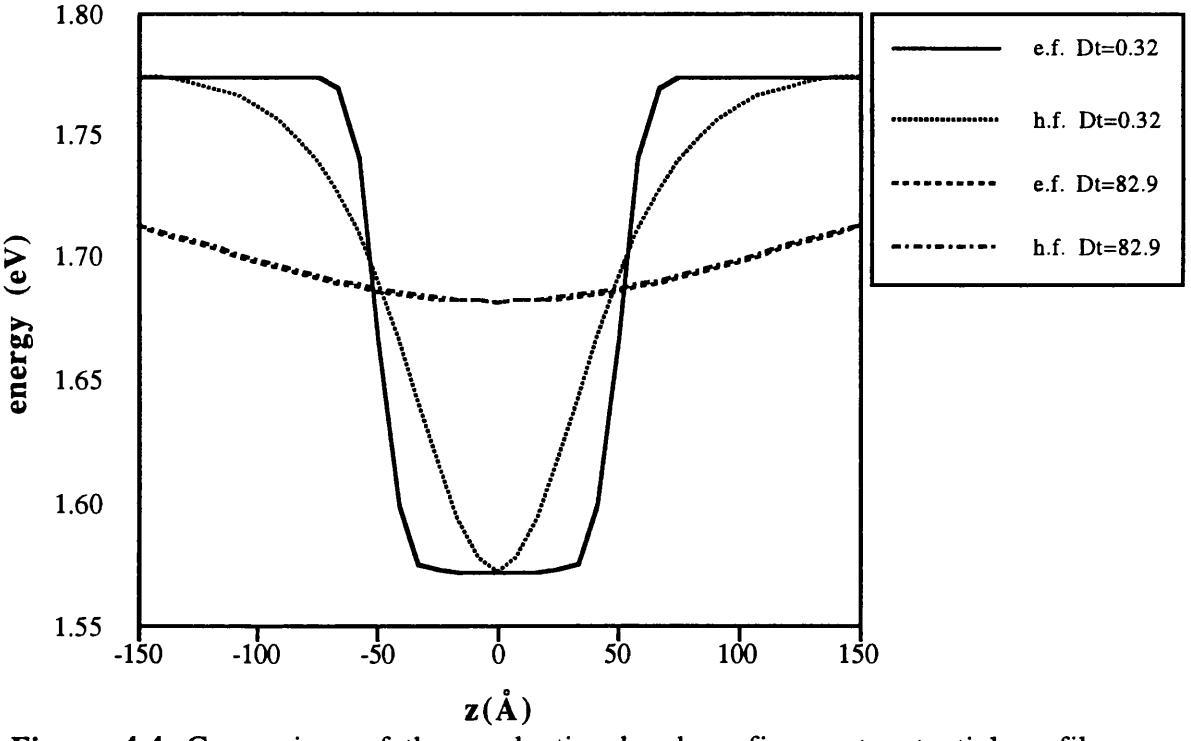

Figure 4.4. Comparison of the conduction band confinement potential profile calculated from the error function model and the hyperbolic secant model for different stages of the disordering process (Dt is expressed in units of nm^2).

$$V(z) = -V_0 \operatorname{sech}^2(\beta z) = -\frac{V_0}{\cosh^2(\beta z)}$$

(4.6)

where β is a parameter that controls the shape of the hyperbolic quantum well. This potential has a minimum $-V_0$ and rises asymptotically to zero at $\pm\infty$. The hyperbolic potential profile resembles the error function profile in shape and has the advantage that an analytic solution of the effective mass equation at the Γ point of the Brillouin zone for the calculation of the subband states exists [20]. By matching the error function profile and the hyperbolic secant profile at the zone centre an expression for the parameter β relating it with the diffusion constant and diffusion time can be obtained,

$$\beta = \frac{2}{L_z}\operatorname{erf}\left(\frac{L_z}{4\sqrt{Dt}}\right) = \frac{1}{h}\operatorname{erf}\left(\frac{h}{2\sqrt{Dt}}\right)$$

(4.7)

The potential depth for the conduction and valence band is equal to,

$$V_{0c} = Q_c \beta h \, \Delta E_{g\text{-}sw}$$

(4.8a)

$$V_{0v} = Q_v \beta h \, \Delta E_{g\text{-}sw}$$

(4.8b)

where $\Delta E_{g\text{-}sw}=E_{g\text{-}GaAs}-E_{g\text{-}Ga_{1-Co}Al_{Co}As}$, the square well gap difference. The confinement profile for the conduction band calculated from the hyperbolic secant profile can be compared to that calculated from the error function model. From figure 4.4 it can be observed that for large Dt the hyperbolic secant profile closely resembles the error function profile in shape. This is not the case for small Dt since the hyperbolic secant profile does not converge to a square well as $Dt \rightarrow 0$ and consequently it is very different from the error function profile. The effect of the disordered well shape on the calculations of the interband transition energies and the optical properties and the accuracy of the approximate

hyperbolic secant model at the different stages of the disordering process will be evaluated in the following sections.

4.3 Band structure calculations

The wavefunctions ψ^i and the energy levels $E^i(\mathbf{k}_{||})$, i=c,hh,lh, of a disordered quantum well can be calculated from the envelope function scheme described in chapter 2. The conduction band is considered to be decoupled form the valence band. The conduction subband edge at the zone centre, $\mathbf{k}_{||}=0$, can be calculated from the Schrödinger-like equation for the envelope function,

$$\left[-\frac{\hbar^2}{2m_c^*(z)}\frac{\partial^2}{\partial z^2}+V_c(z)\right]\phi_n^c(z)=E_n^c\phi_n(z) \tag{4.9}$$

where $V_C(z)$ is the disordered well conduction band potential profile, given in expression (4.5a) and $m_c^*(z)$ is the position dependent conduction band effective mass. For the case of the error function profile equation (4.9) can be solved numerically using the standard finite difference method. The error function profile is a smooth varying potential profile and has boundary conditions only at infinity, where the envelope functions must vanish within the barrier regions. Each of the conduction band levels calculated is twice degenerate (Kramers degeneracy). Away from the zone centre ($\mathbf{k}_{||}\neq0$) the conduction band is assumed to be parabolic. The valence subbands and their dispersion relations can be calculated from the 4×4 Hamiltonian given in expression (2.31), where $V_V(z)$ is the disordered well valence band potential profile given in expression (4.5b).

The lowest conduction subband with respect to the bottom of the conduction band potential (at z=0) and the lowest valence subband with respect the top of the valence band at $\mathbf{k}_{||}=0$

calculated for a 10nm GaAs-$Ga_{0.7}Al_{0.3}As$ are shown in figure 4.5. It can be observed that at the initial stages of the disordering process the subband-edge energies increase, reaching a maximum at $Dt \approx 7nm^2$ and then decrease approaching zero as $Dt \rightarrow \infty$. This effect takes place because in the early stages of the process only the heterostructure interfaces are being affected, resulting in a well with the same depth and a relatively narrow width. As a consequence the energy levels initially shift away from the bottom of the well (or the top for the valence band). While the intermixing process proceeds the well becomes shallower and wider and the energy levels shift towards the bottom of the well. However the interband transition energy $E_{c1\text{-}hh1}$ defined as $E_{c1\text{-}hh1}=E_g+E_{c1}+E_{hh1}$ increases monotonically with Dt, since the disordered quantum well bandgap E_g increases rapidly and overpowers the reduction of the energy subbands [21]. It should also be mentioned that the number of bound states increases with Dt. At the latter stages when the well is extensively disordered the material displays bulk-like behaviour and the energy states converge to a continuum.

In chapter 2 it has been observed that the square well in-plane dispersions of the Γ_8 subbands display a strong nonparabolicity due to valence band mixing. In figure 4.6 and 4.7 the shift of the hh1 and the lh1 energy levels at the different stages of the disordering process, for a 10nm GaAs-$Ga_{0.7}Al_{0.3}As$, can be observed. The calculation is extending from a square quantum well (Dt=0) to an almost fully disordered quantum well ($Dt \approx 84nm^2$). The valence band mixing effect remains strong with increasing interdiffusion and an almost parabolic band is restored at the latter stages of the disordering process (figures 4.6,4.7). It should be mentioned that, because the potential profile is symmetric, the valence subbands exhibit a twofold Kramers spin degeneracy.

For the case of the hyperbolic secant potential profile given in expression (4.6) an analytic solution for the eigenvalues and eigenvectors of equation (4.9) exists, assuming that $m_c^*(z)$ is constant with respect to z and equal to m_c^*. This analytic solution is described in

Appendix C. By applying this solution to the conduction band of the disordered quantum well, the subband energies E_{nc} at $\mathbf{k}_{||}=0$ can be obtained and are equal to,

$$E_{nc} = V_{0c} - \frac{\hbar^2\beta^2}{8m_c^*}\left[\left(\frac{8m_c^*V_{0c}}{\hbar^2\beta^2}+1\right)^{\frac{1}{2}} - (2n_c+1)\right]^2 \tag{4.10a}$$

$$n_c = 0,1,\ldots,n_c < \sqrt{\frac{2m_c^*V_{0c}}{\hbar^2\beta^2}+\frac{1}{4}} - \frac{1}{2} \tag{4.10b}$$

In the analytic solution, the effect of band coupling cannot be included in the calculations for the disordered quantum well valence band and so the heavy hole and light hole subbands are considered to be decoupled. At the zone centre the energy levels are calculated from (4.9) by setting the relevant parameters to those of the heavy or light hole subbands. Away from the zone centre the dispersion relations are assumed to be parabolic. Similarly to equation (4.10) the valence subband energy E_{nv} at $\mathbf{k}_{||}=0$ is equal to,

$$E_{nv} = -V_{0v} + \frac{\hbar^2\beta^2}{8m_v^*}\left[\left(\frac{8m_v^*V_{0v}}{\hbar^2\beta^2}+1\right)^{\frac{1}{2}} - (2n_v+1)\right]^2 \tag{4.11a}$$

$$n_v = 0,1,\ldots,n_v < \sqrt{\frac{2m_v^*V_{0v}}{\hbar^2\beta^2}+\frac{1}{4}} - \frac{1}{2} \tag{4.11b}$$

where the subscript v takes the values hh and lh for the calculation of the heavy hole or the light hole subbands respectively. From expressions (4.10) and (4.11) the conduction and valence subbands for the hyperbolic secant profile can be calculated for the 10nm GaAs-$Ga_{0.7}Al_{0.3}As$ quantum well and compared with the subband energies obtained for the error function profile at $\mathbf{k}_{||}=0$ in figures 4.8 and 4.9. It has been demonstrated that the hyperbolic potential profile as $Dt\rightarrow 0$ does not approach the square potential profile. For this limiting

case the calculated subbands are larger in magnitude than those calculated for the square well and the error function potential profile.

While the disordering process continues, the energy levels shift monotonically towards the bottom of the well, converging to the energy levels calculated from the error function profile, as expected from the comparison of the potential profiles obtained from the two disordering models. The interband transition energy shift $\Delta E_{c1\text{-}hh1}=E_{c1\text{-}hh1}-E_{sw\text{-}c1\text{-}hh1}$ calculated from the two models is shown in figure 4.10. For values of Dt larger than 15nm^2 (L_d≈4nm), corresponding to interband transition energy shift of approximately 120meV, the hyperbolic function model is a good approximation of the error function model for the calculation of $\Delta E_{c1\text{-}hh1}$.

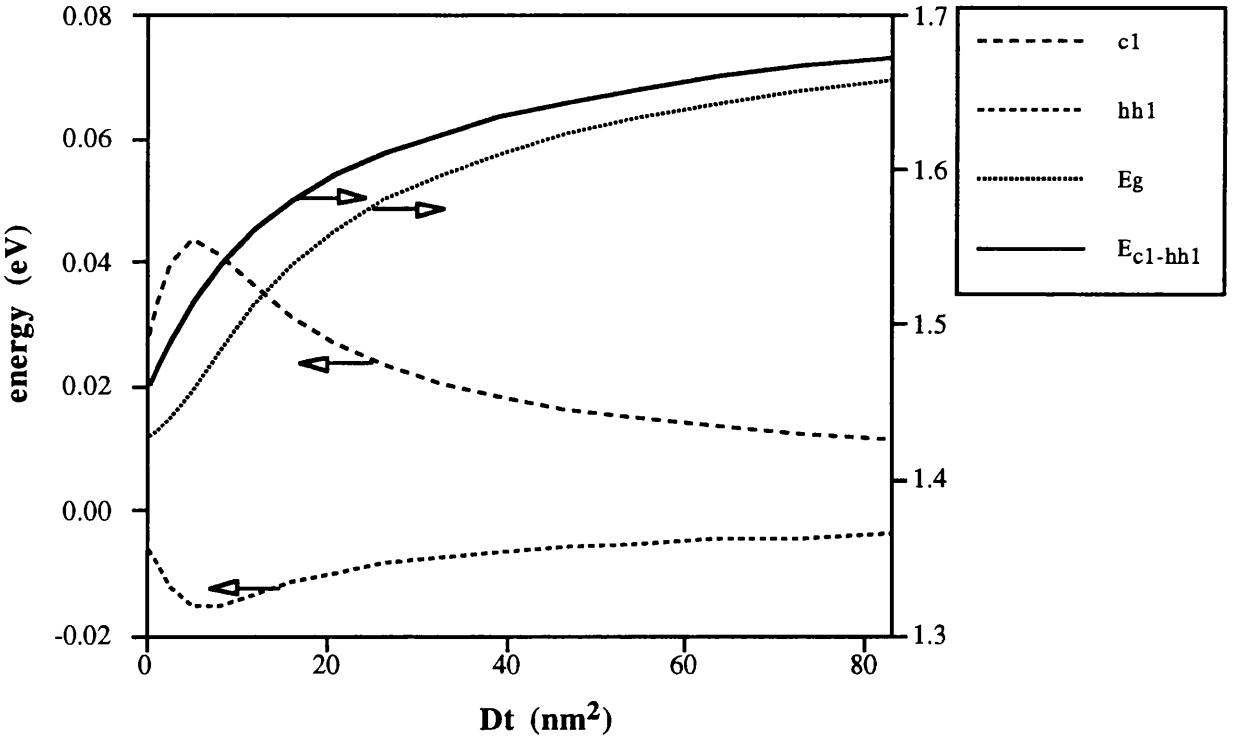

Figure 4.5. Energy shift of the conduction subbands c1 and hh1, the bandgap E_g and the interband transition $E_{c1\text{-}hh1}$ with respect to Dt, calculated using the error function model.

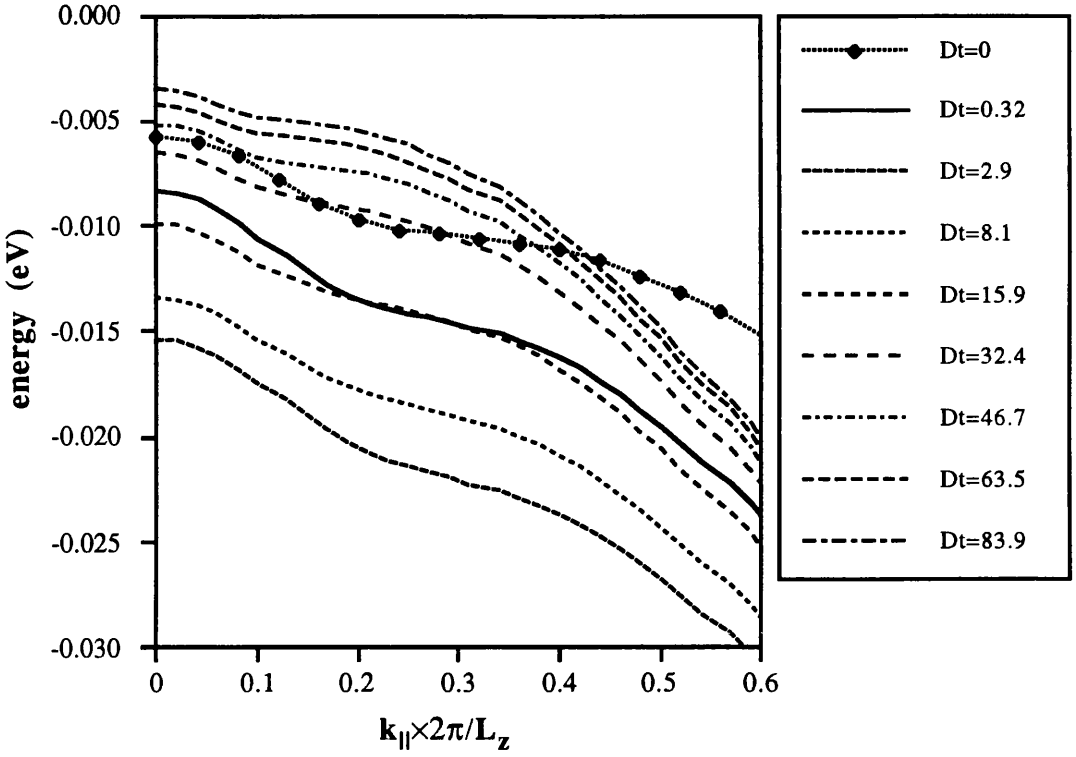

Figure 4.6. Shift of the valence energy subband hh1 calculated using the error function model (Dt=0 corresponds to a square well, Dt in units of nm^2).

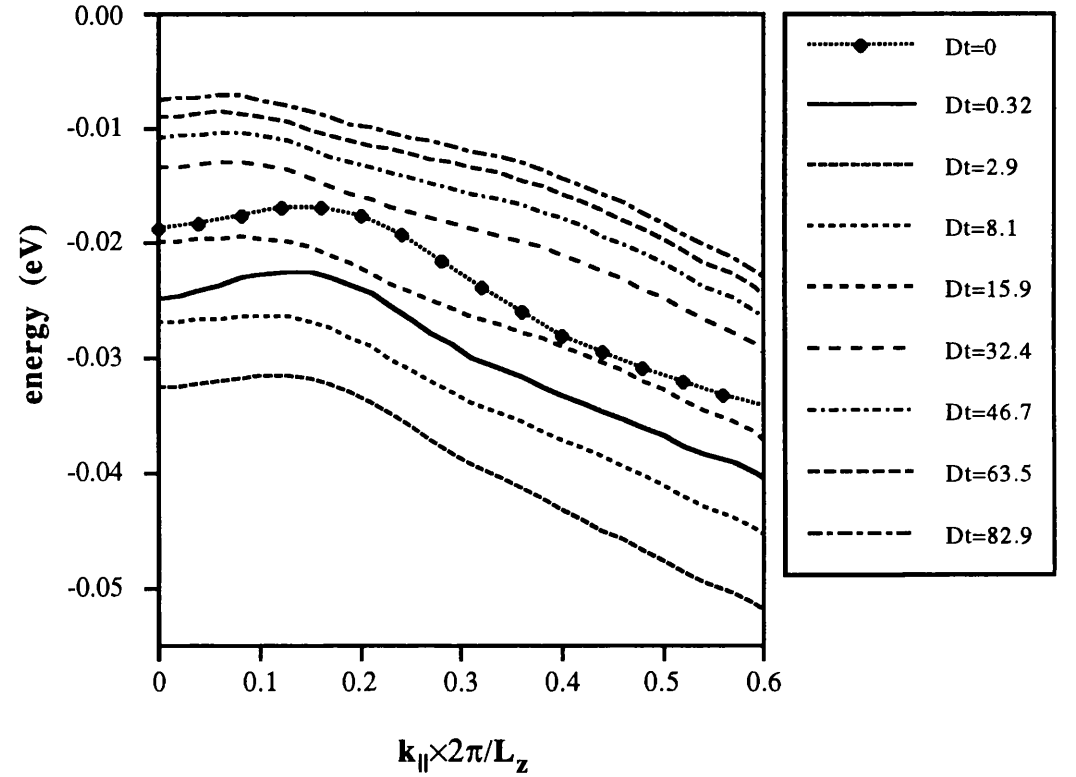

Figure 4.7. Shift of the valence energy subband lh1 calculated using the error function model (Dt=0 corresponds to a square well, Dt in units of nm^2).

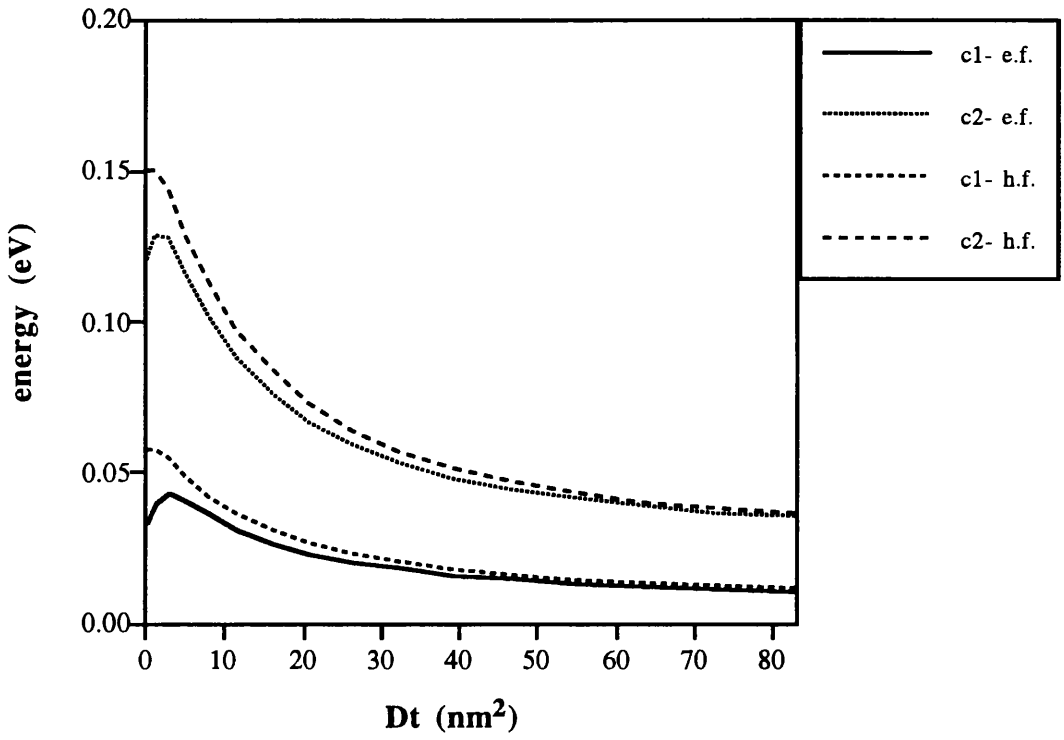

Figure 4.8. Shift of the conduction energy subbands c1 and c2 calculated using the error function model (e.f.) and the hyperbolic function model (h.f.).

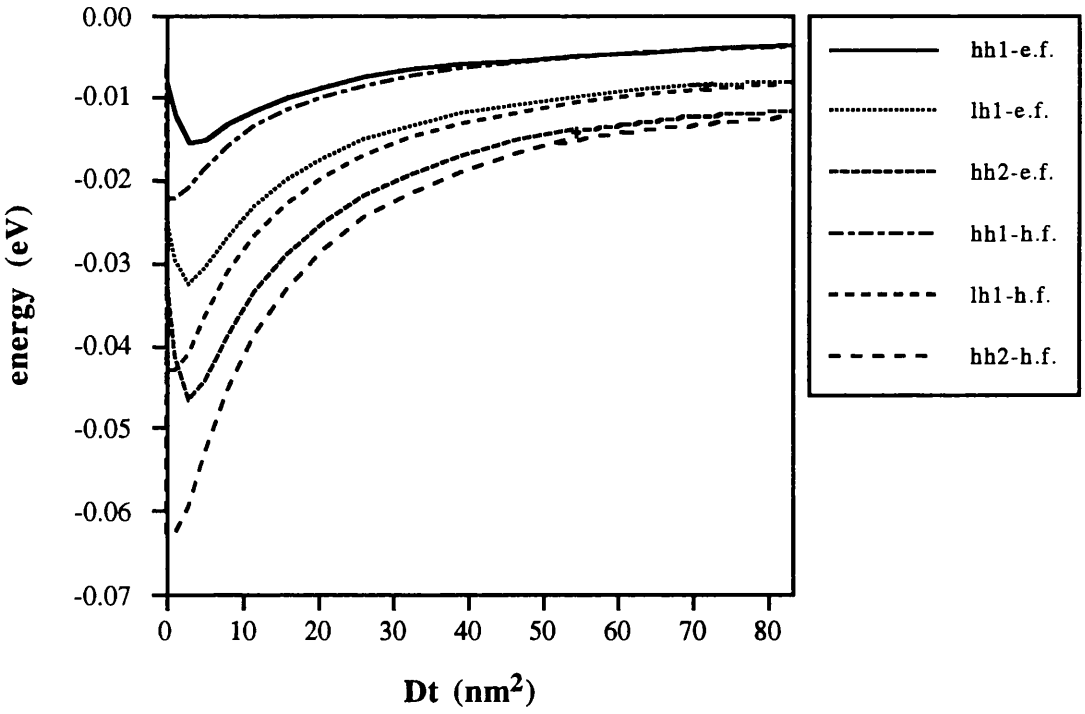

Figure 4.9. Shift of the valence energy subbands hh1, lh1 and hh2 calculated using the error function model (e.f.) and the hyperbolic function model (h.f.).

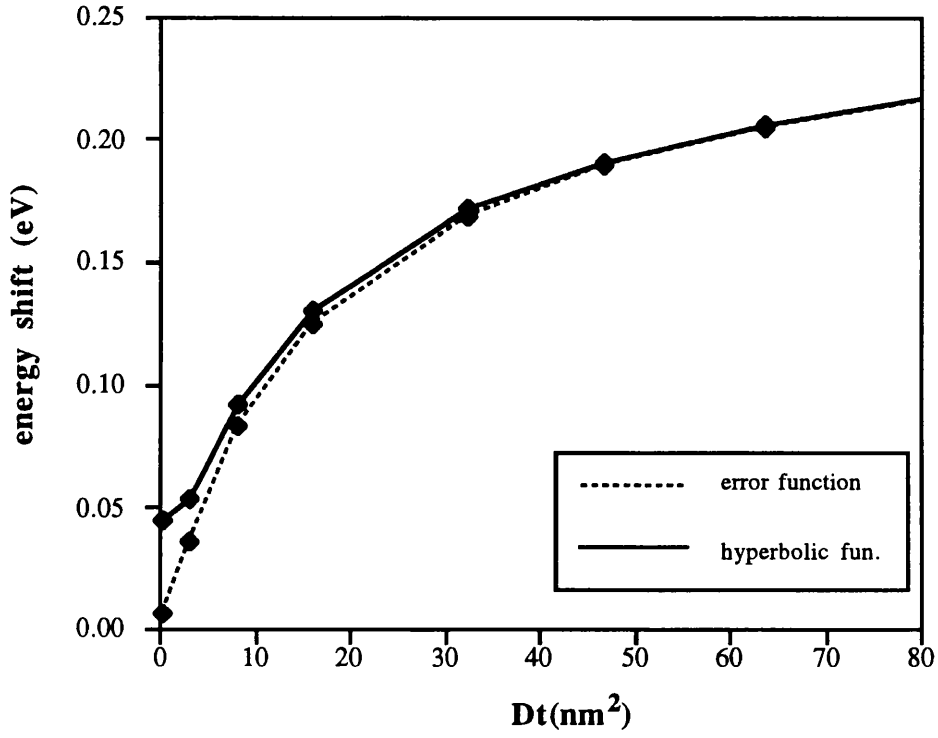

Figure 4.10. Shift of the interband energy $\Delta E_{c1\text{-}hh1}$ calculated using the error function model and the hyperbolic function model (the diamonds correspond to the potential profiles and Dt of figure 4.3).

4.4 Refractive index and absorption coefficients

In the introduction of this chapter it was acknowledged that the intermixing process is useful for a number of potential applications in integrated optoelectronics. The design of integrated devices relies on understanding the influence of the intermixing process on the optical properties of the quantum well structures. The effect of the disordering process on the potential profile and consequently on the confined subband-edge energies has been evaluated in the previous sections. Making use of these results the absorption coefficient and the refractive index through the different stages of the disordering process can be calculated. The method that will be used is the density matrix formalism described in chapter 3. The TE and TM absorption coefficients can be calculated for the error function

model from the imaginary part of expression (3.44) and from (3.62) by summing the contributions from the interband transitions and integrating numerically, while the TE and TM refractive index change from the bulk material can be calculated from the real part of expression (3.44) and (3.61)

The results obtained for a 10nm GaAs-$Ga_{0.7}Al_{0.3}As$ are presented in figures 4.11 to 4.14. The TE and TM absorption spectra are determined by the transitions between the conduction (c) to the heavy hole (hh) and light hole (lh) subbands. From the selection rules given in table 3.1 it can be observed that the TM absorption coefficient (α_{TM}) is dominated by the light hole transitions. For the TE absorption coefficient (α_{TE}) the contribution of both transitions is almost equivalent, with that of the heavy hole slightly larger. It can be seen that for photon energies below the c-hh interband transition energy the TE is larger then the TM absorption coefficient ($\alpha_{TE}>\alpha_{TM}$), while close to the c-lh edge the TM becomes larger then the TE ($\alpha_{TE}<\alpha_{TM}$). In figures 4.11 and 4.12 it can also be observed that for both TE and TM polarisations the absorption coefficient displays a substantial blue shift of the absorption edge. The magnitude of the first absorption peak remains almost constant through the early stages of the disordering process. At the latter stages of the disordering the absorption coefficient at the first peak is not only shifted to higher photon energies, but is also reduced drastically in magnitude.

The refractive index spectra exhibits similar behaviour for both TE and TM polarisations (figures 4.13,4.14). Δn displays a substantial blue shift and the magnitude of the first peak remains almost constant through the early stages of the disordering process. At the latter stages of the disordering Δn is not only shifted to higher photon energies, but also reduced drastically in magnitude. This behaviour is expected since the material is becoming bulk-like and the difference of the refractive index change from the bulk refractive index is bound to reduce.

The absorption coefficient can be calculated for the hyperbolic secant potential profile model from expressions (3.44) and (3.62) similarly to the error function profile. Two cases can be considered. The first is to use the analytic expressions for the subband energies and their corresponding wavefunctions, derived in the previous section, in order to calculate the absorption coefficient from expressions (3.44) and (3.62). The second is to calculate numerically the subband energies and wavefunctions of the hyperbolic secant potential profile, similarly to the error function calculations, so that the valence band-coupling may be incorporated. The second case is included in order to allow us to estimate and compare the effect of the potential profile used separately from the effect of valence band-coupling on the calculation of the optical properties of disordered quantum wells. In figures 4.15 and 4.16 the absorption coefficients calculated from the error function model, the analytic hyperbolic model and the numerical hyperbolic model including band-coupling are compared for two different examples.

In figure 4.15 the well is partially intermixed and only slightly deviating from a square well ($Dt=0.32nm^2$). For this case the hyperbolic secant potential profile differs significantly from the error function profile and as a result the calculated subband energies, which have been discussed in the previous sections. It is expected that the calculated absorption coefficients will also differ. The α_{TE} calculated using the hyperbolic potential profile including band-coupling is similar in shape to the α_{TE} calculated using the error function potential profile but shifted by 40meV, which is exactly the calculated energy difference in the $E_{c1\text{-}hh1}$ between the two models. The α_{TE} calculated using the analytic hyperbolic model matches the numerical hyperbolic α_{TE} below the $E_{c1\text{-}hh1\text{-}h}$ interband energy (indicated with an arrow), in other words it is shifted by 40meV from the α_{TE} of the error function model. Above the $E_{c1\text{-}hh1\text{-}h}$ edge the magnitude of the absorption coefficient becomes much smaller to that obtained using the other models.

In figure 4.16 the well is almost totally intermixed and results in a bulk-like material ($Dt=82.9nm^2$). For this example the hyperbolic secant potential profile resembles the error function profile and as a result the calculated subband energies at the zone centre $\mathbf{k}_{||}=0$ are approximately equal for the three cases. Away from the zone centre the in-plane dispersion relations will be approximately the same for the error function profile and the numerical hyperbolic profile, since valence band-mixing is included in both cases. For the analytic hyperbolic secant model the dispersion relations are assumed to be parabolic. As a result the absorption coefficient calculated using the hyperbolic potential profile including band-coupling is equal to the α_{TE} calculated using the error function potential profile. It is also equal to the α_{TE} calculated using the analytic hyperbolic model below the $E_{c1\text{-}hh1\text{-}h}$ interband energy (indicated with an arrow). For photon energies higher then the $E_{c1\text{-}hh1\text{-}h}$ edge the magnitude of the α_{TE} calculated using the analytic hyperbolic model becomes smaller to that obtained from the other models.

Similar behaviour is observed when comparing the refractive index of the disordered quantum well calculated for the three different cases. In figure 4.17 the refractive index change from the bulk semiconductor material for the TE polarisation (Δn_{TE}) is calculated for a well partially intermixed and only slightly deviating from a square well ($Dt=0.32nm^2$). The Δn_{TE} calculated using the hyperbolic potential profile including band-coupling is similar in shape to the Δn_{TE} calculated using the error function potential profile but shifted by 40meV, which is exactly the calculated energy difference in the $E_{c1\text{-}hh1}$ between the two models. The Δn_{TE} calculated using the analytic hyperbolic model does not match the numerical hyperbolic Δn_{TE} neither below, nor above the $E_{c1\text{-}hh1\text{-}h}$ interband energy. In figure 4.18 Δn_{TE} is calculated for a well almost totally intermixed ($Dt=82.9nm^2$). The Δn_{TE} calculated using the hyperbolic potential profile including band-coupling is equal to the Δn_{TE} calculated using the error function potential profile, but it is not equal to the Δn_{TE} calculated using the analytic hyperbolic model.

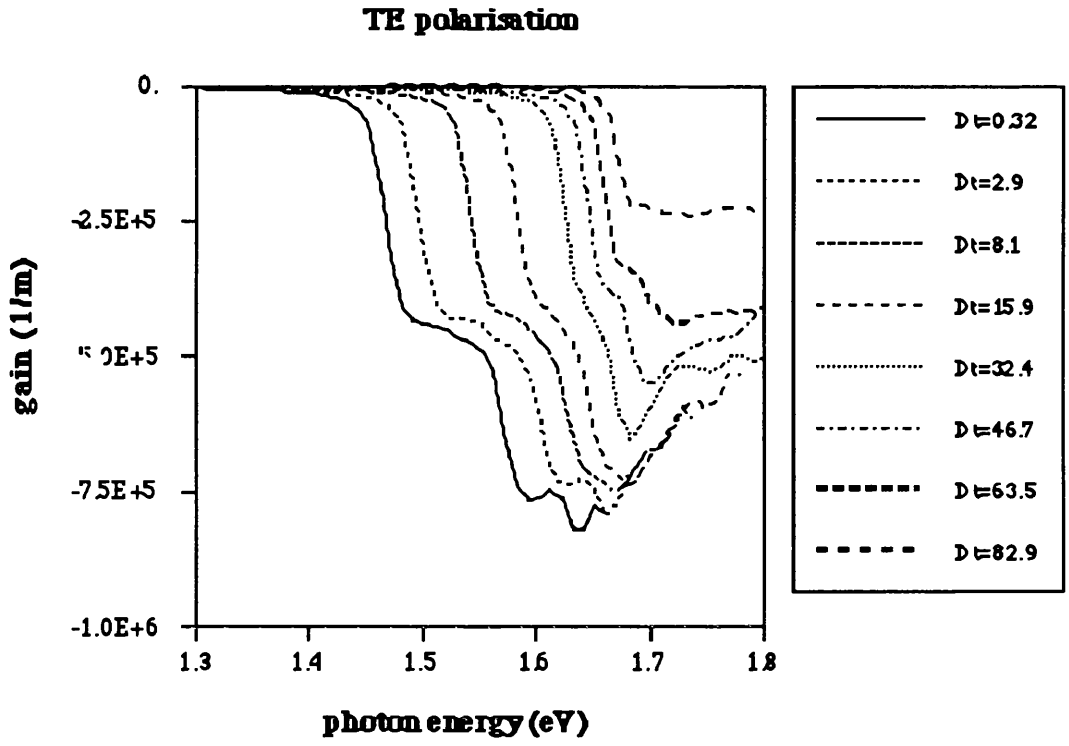

Figure 4.11. TE absorption spectra for a 100Å GaAs-$Ga_{0.7}Al_{0.3}As$ quantum well at the different stages of the disordering process (Dt in units nm^2).

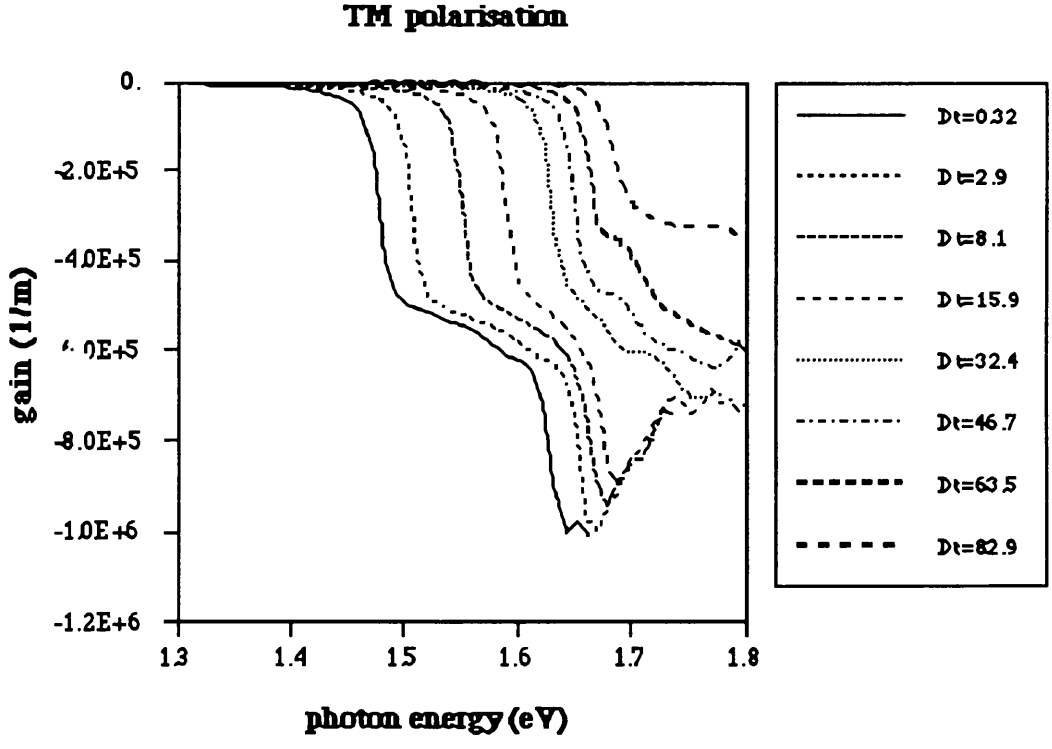

Figure 4.12. TM absorption spectra for a 100Å GaAs-$Ga_{0.7}Al_{0.3}As$ quantum well at the different stages of the disordering process (Dt in units nm^2).

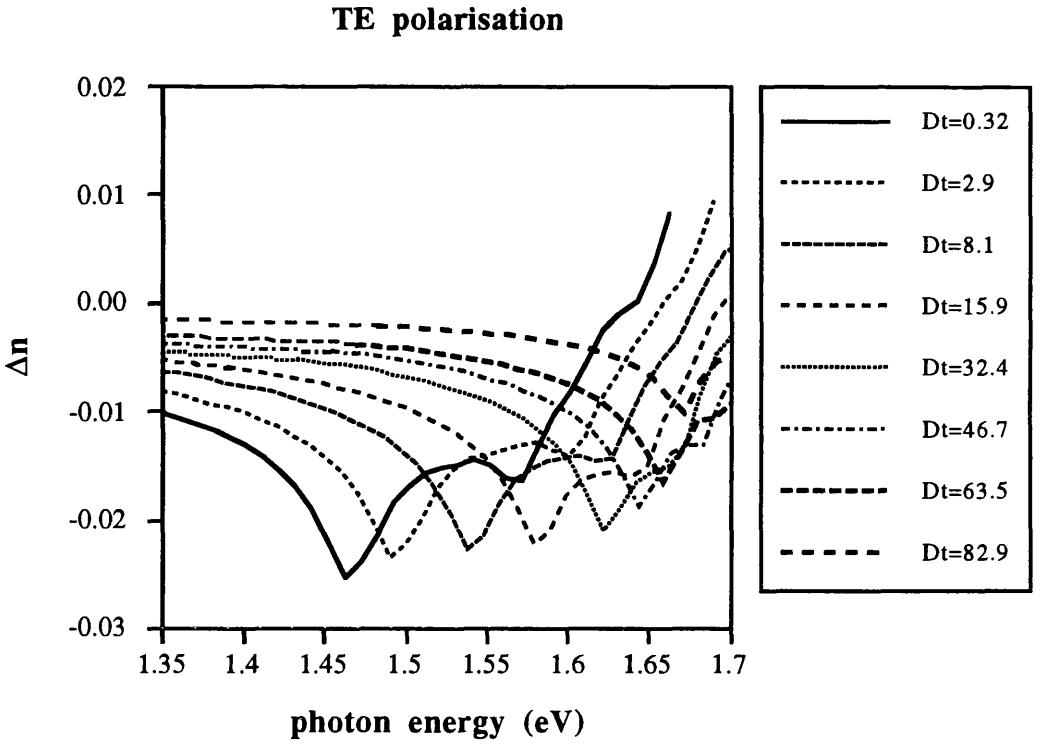

Figure 4.13. TE refractive index change spectra for a 100Å GaAs-$Ga_{0.7}Al_{0.3}As$ quantum well at the different stages of the disordering process (Dt in units nm^2).

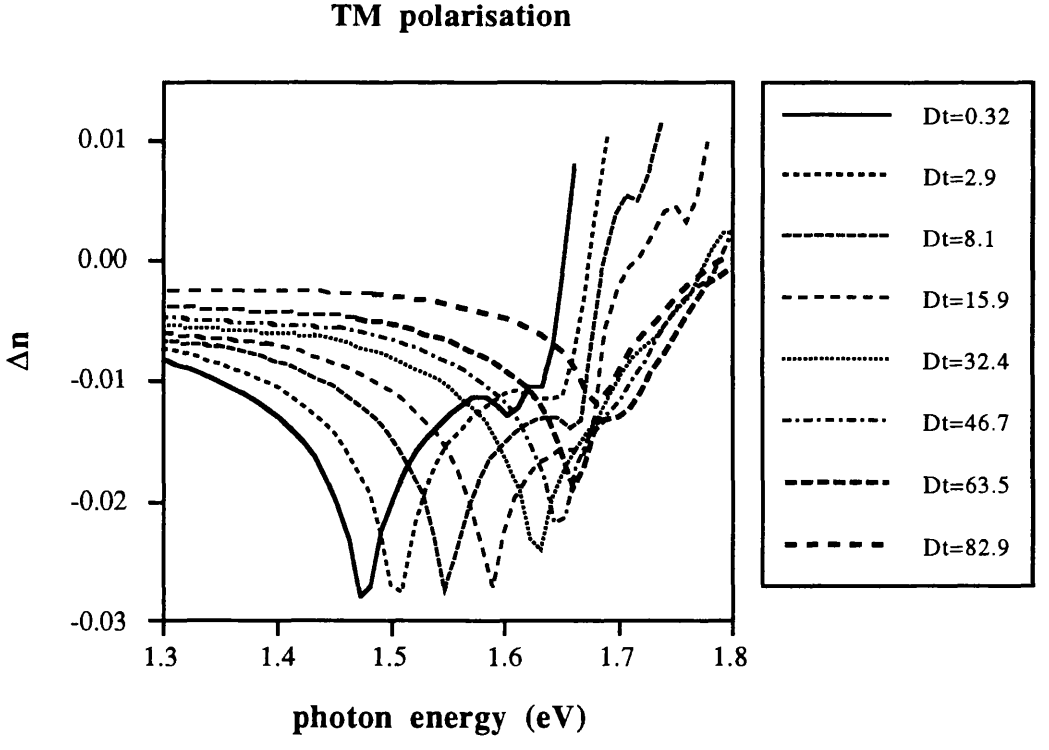

Figure 4.14. TM refractive index change spectra for a 100Å GaAs-$Ga_{0.7}Al_{0.3}As$ quantum well at the different stages of the disordering process (Dt in units nm^2).

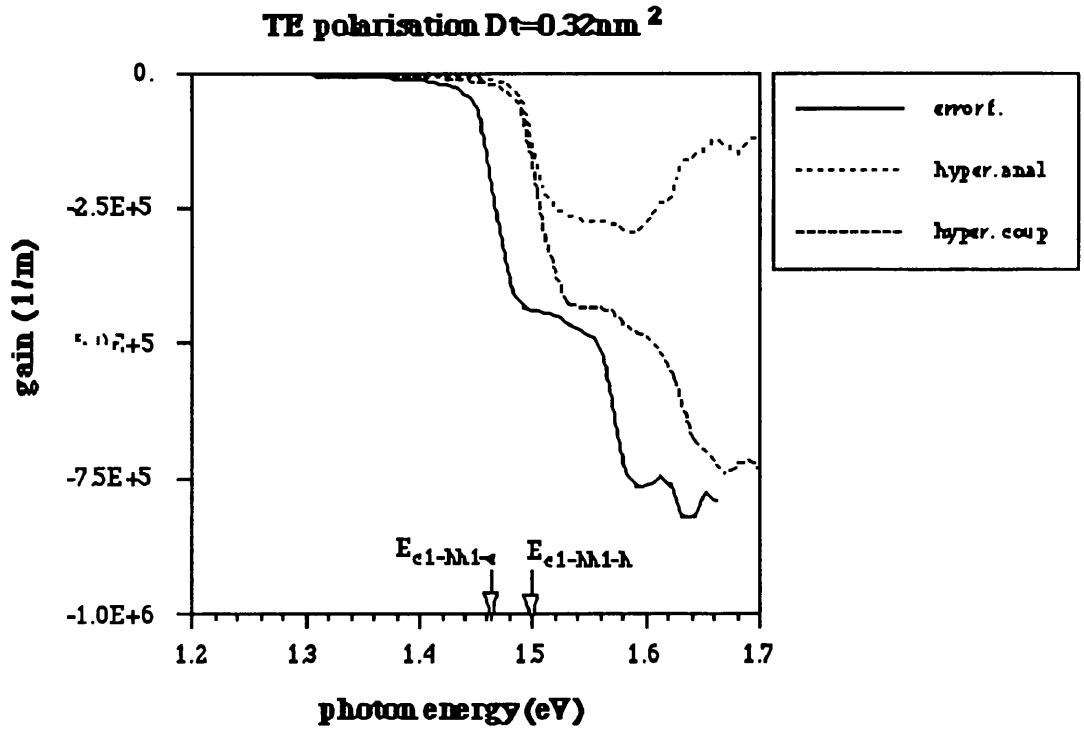

Figure 4.15. Comparison of the α_{TE} for a partially intermixed 100Å GaAs-$Ga_{0.7}Al_{0.3}As$ quantum well calculated using the different models.

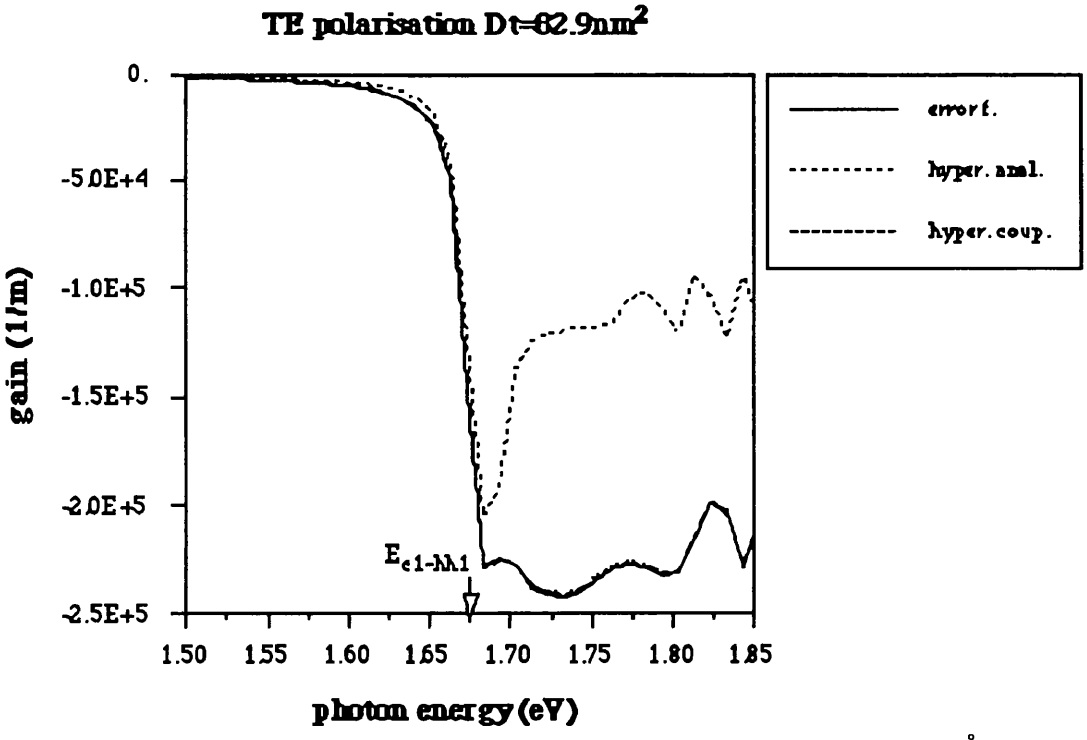

Figure 4.16. Comparison of the α_{TE} for a totally intermixed 100Å GaAs-$Ga_{0.7}Al_{0.3}As$ quantum well calculated using the different models.

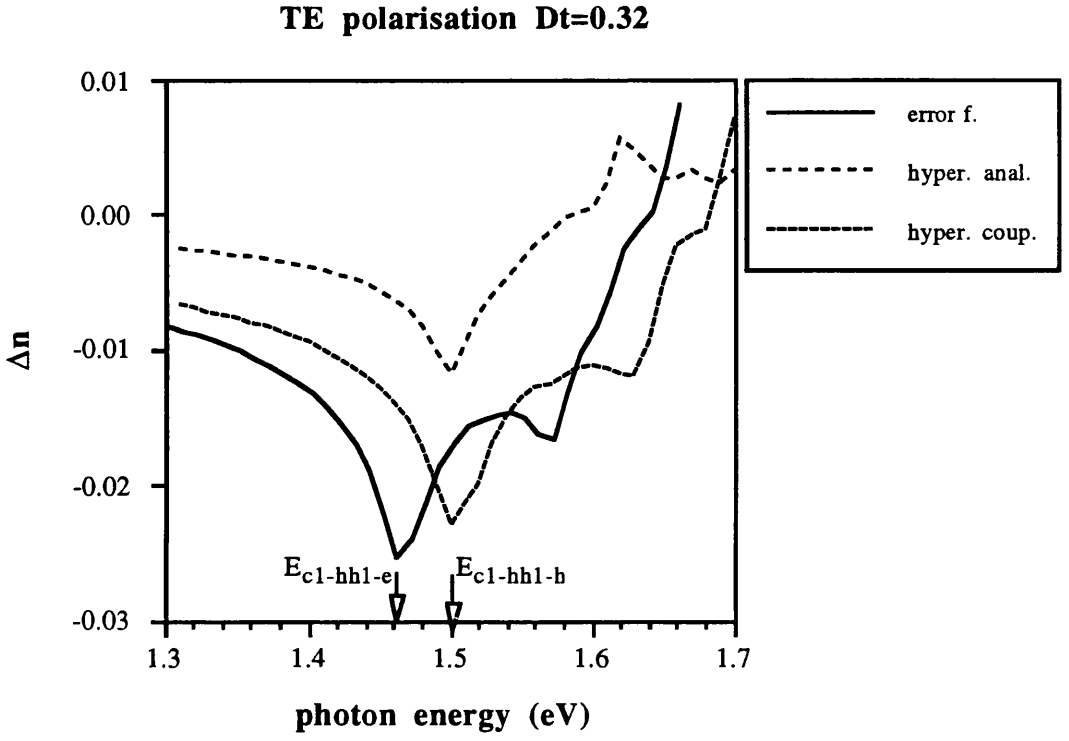

Figure 4.17. Comparison of the Δn_{TE} for a partially intermixed 100Å GaAs-$Ga_{0.7}Al_{0.3}As$ quantum well calculated using the different models.

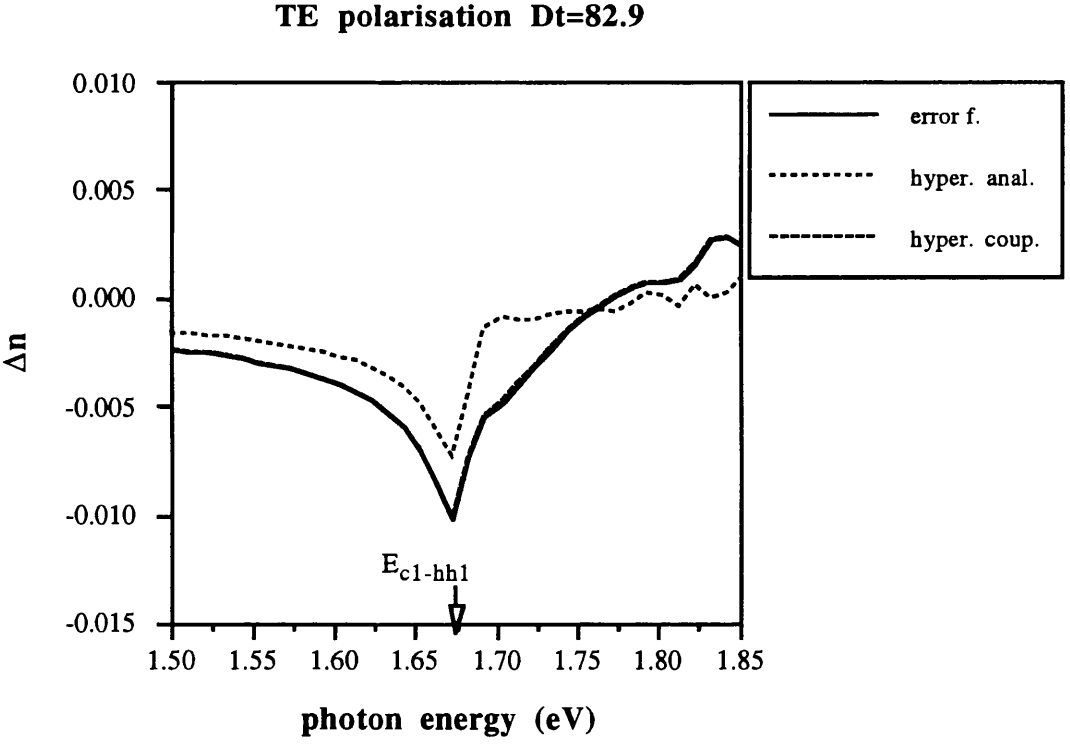

Figure 4.18. Comparison of the Δn_{TE} for a totally intermixed 100Å GaAs-$Ga_{0.7}Al_{0.3}As$ quantum well calculated using the different models.

4.5 Discussion

The technique of modelling the interband transition energy $E_{c1\text{-}hh1}$ and comparing it with experimental measurements of the shift in the photoluminescence is a standard method of estimating the diffusion coefficient [22]-[23]. This is accomplished by performing several anneals on a sample already implanted with an impurity and record the photoluminescence after each anneal. Then from the calculated graph $\Delta E_{c1\text{-}hh1}$-Dt the diffusion coefficient D can be obtained for each step of the annealing process. The data obtained can be plotted with respect to the annealing time in order to determine how D varies throughout the process. This model can also be used to determine whether an implant or any other disordering method used has increased the degree of intermixing or not.

By applying this technique the diffusion coefficient can be estimated for a 6nm GaAs quantum well with $Ga_{0.74}Al_{0.26}As$ barrier implanted with two different impurities, fluorine (F) and boron (B) and annealed. The interband transition energy shift $\Delta E_{c1\text{-}hh1}$ can be calculated using the error function model and the hyperbolic secant function model (figure 4.19) and compared to the photoluminescence measurements obtained in Ref. [24]. The diffusion coefficient obtained from the two models for the case of fluorine disordering can be seen in figure 4.20. It can be observed that D is not constant but reduces with time and the value for D calculated using the hyperbolic model is smaller than that calculated using the error function model. For the case of boron disordering the diffusion coefficient was estimated to be constant with time. For this case D was calculated only by using the error function model because the measured interband energy shift was smaller than the minimum the hyperbolic model is able to predict. For longer diffusion times and larger energy shifts a reduction of D might be expected even for the case of boron. Comparing the two implants the diffusion coefficient obtained for fluorine measurements is almost double to that obtained for boron. It is apparent that the use of fluorine enhances the disordering process.

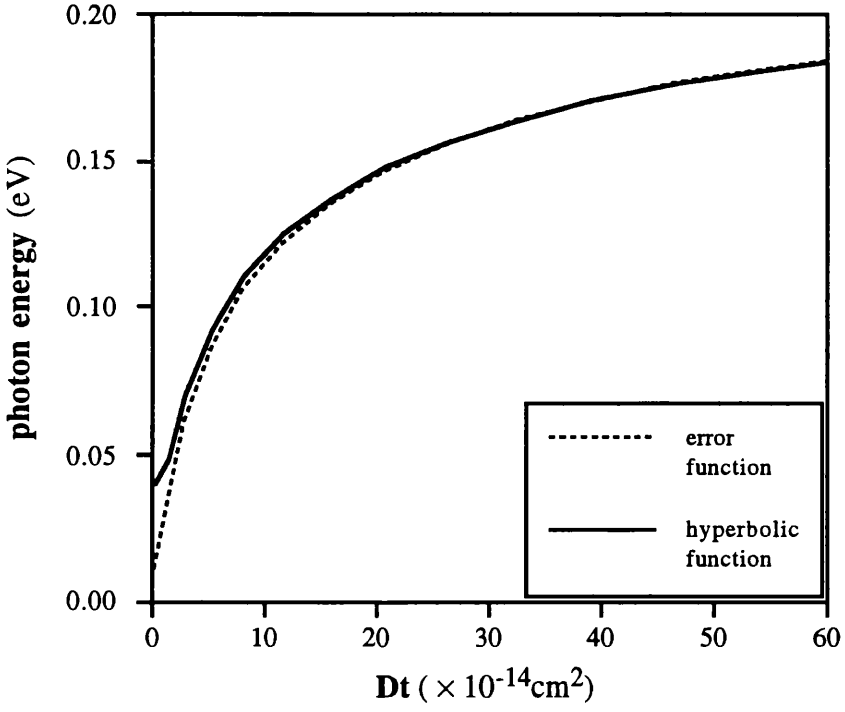

Figure 4.19. Shift of the interband energy $\Delta E_{c1\text{-}hh1}$ calculated using the error function model and the hyperbolic function model for a 6nm GaAs-$Ga_{0.74}Al_{0.26}As$ quantum well.

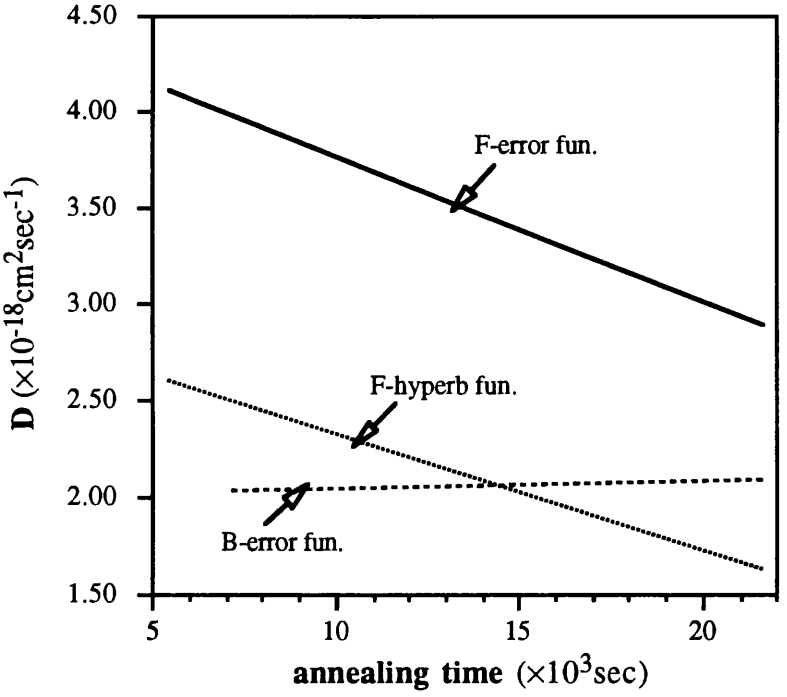

Figure 4.20. Diffusion coefficient D calculated using the error function model and the hyperbolic function model for a 6nm GaAs-$Ga_{0.74}Al_{0.26}As$ quantum well for fluorine (F) and boron (B) impurity induced disordering.

The magnitude of D is of the order $10^{-18}cm^2sec^{-1}$ and this value coincides with the coefficients estimated in previous theoretical work [22]. If D is constant then the initial hypothesis of a Fick's law diffusion process is sufficient. The assumption for constant D is valid if at a given temperature the concentration of the point defect species governing the diffusion process is constant in space and time. For diffusion in a semiconductor and particularly in GaAs this is not usually the case and the diffusion process can be described more accurately by the approximation that the diffusion coefficient D(C) is concentration-dependent.

The error function method and the hyperbolic secant function method have been used by other researchers for the calculation of the absorption coefficient and the refractive index change. The results obtained in the previous section using the hyperbolic secant model for the absorption coefficient are in close agreement with the results from Ref. [17] and [19], as well as the results of the refractive index change calculations from Ref. [18]. For the case of the error function model the published calculations differ from those of the previous section in the computations of the absorption coefficient and the refractive index change. These variations are due to the fact that in the published calculations the exciton effect is taken into account in the description of the band structure [25]-[27]. Therefore the present formulation demonstrates simplified optical coefficients without the exciton resonance at the absorption edge, which may be unresolved even after long diffusion times. As a result it can introduce an inaccuracy at the band edge in certain cases and an underestimation of the optical properties. The differences can also be due to fact that in the published calculations the refractive index change was obtained from the absorption coefficients using the Kramers-Krönig transformation. An other important parameter in estimating the optical properties of disordered quantum wells is the number of states taken into account in the computations. In the calculations presented in this chapter only the bound states were considered, while in the published calculations a number of the states extending in the continuum were also included.

Summarising the results obtained in this chapter a disordered quantum well can be described by a sum of error functions obtained from Fick's law of diffusion, assuming a constant diffusion coefficient D. This error function potential profile can be approximated by a hyperbolic secant potential profile that has analytic solutions. This approximation is valid only for long diffusion times (large Dt) for the calculation of the photoluminescence peak $E_{c1\text{-}hh1}$ and for the calculation of the absorption coefficient close to the absorption edge. For short diffusion times and for the calculation of the refractive index change the results obtained using the analytic solution differ substantially from the results obtained using the error function model. Further improvement in the calculation of the optical properties presented in this chapter is possible if the exciton effect and a number of the disordered quantum well states that are not bound inside the well but extend in the continuum are included. For more accurate results it is also of importance to modify the assumption of a constant diffusion coefficient to that of a the diffusion coefficient D(C) that is concentration-dependent.

4.6 Conclusions

In this chapter the properties of the disordered quantum wells have been studied. The confinement profile describing the wells after intermixing was obtained using Fick's law of diffusion. For the calculation of the band structure two cases were considered the error function potential profile including valence band mixing and an approximate profile with an analytic solution, the hyperbolic secant potential profile with parabolic bands. Numerical results for the absorption α and the refractive index change Δn were obtained. The results were compared and the effect of the shape of the profile and the effect of valence band mixing on the optical properties and the diffusion coefficient was discussed. The calculations were found to be in close agreement with the previously published data and the

method enabled us to estimate adequately the effect of the intermixing process on the band structure and the optical properties of the disordered quantum wells.

References

[1] J.H. Marsh, S.I. Hansen, A.C. Bruce, R.M. De La Rue, *Applications of neutral impurity disordering in fabricating low-loss optical waveguides and integrated waveguide devices*, Opt. and Quant. Electron., vol. **23**, pp. S941-S957, 1991

[2] W.P. Gillin, D.J. Dunstan, K.P. Homewood, L.K. Howard and B.J. Sealy, *Interdiffusion in InGaAs/GaAs quantum well structures as a function of depth*, J. Appl. Phys., vol. **73**, pp. 3782-3786, 1993

[3] A. Hamoudi, E. Ligeon, K. Saminadayar, J. Cibert, L.S. Dang and S. Tatarenko, *Annealing effect on the shape of CdTe/ZnTe quantum wells*, Appl. Phys. Lett., vol. **60**, pp. 2797-2799, 1992

[4] J. Beauvais, J.H. Marsh, A.H. Kean, A.C. Bryce and C. Button, *Suppression of bandgap shifts in GaAs/AlGaAs quantum wells using strondium fluoride caps*, Electron. Lett., vol. **28**, pp. 1670-1671, 1992

[5] J.H. Marsh, S.A. Bradshaw and A.C. Bryce, *Impurity induced disordering of GaInAs quantum wells with barriers of AlGaInAs or GaInAsP*, J. of Electr. Materials, vol. **20**, pp. 973-978, 1991

[6] J. Oshinowo, A. Forchel, D. Grützmacher, M. Stollenwerk, M. Heuken and K. Heime, *Photoluminescence study of interdiffusion in $In_{0.53}Ga_{0.47}As/InP$ surface quantum wells*, Appl. Phys. Lett., vol. **60**, pp. 2660-2662, 1992

[7] J.P. Leburton, K. Hess, N. Holonyak, Jr., J.J. Coleman and M. Camras, *Index of refraction of AlAs-GaAs superlattices*, J. Appl. Phys., vol. **54**, pp. 4230-4231, 1983

[8] S.K. Han, S. Sinha and R.V. Ramaswamy, *Effect of zinc impurity-induced disordering on the refractive index of GaAs/AlGaAs multiquantum wells*, Appl. Phys. Lett., vol. **64**, pp. 760-762, 1994

[9] I.V. Bradley, B.L. Weiss, J.S. Roberts, *Alumimium implantation-induced disordering of AlGaAs/GaAs quantum well structures*, Opt. and Quant. Electron., vol **23**, pp. S823-S828, 1991

[10] S.R Andrew, J.H. Marsh, M.C. Holland and A.H. Kean, *Quantum-well laser with integrated passive waveguide fabricated by neutral impurity disordering*, IEEE Photon. Techn. Lett., vol. **4**, pp. 426-428, 1992

[11] S.I. Hansen, J.H. Marsh, J.S. Roberts, R. Gwilliam, *Refractive index changes in a GaAs multiple quantum well structure produced by impurity-induced disordering using boron and fluorine*, Appl. Phys. Lett., vol. **58**, pp. 1398-1400, 1991

[12] J.H. Marsh, *Quantum well intermixing*, Semicond. Sci. Technol., vol. **8**, pp. 1136-1155, 1993

[13] T.Y. Tan, U. Gösele and S. Yu, *Point defects, diffusion mechanisms and superlattice disordering in gallium arsenide-based materials*, Critical Reviews in Solid State and Material Sciences, vol. **17**, pp. 47-106, 1991

[14] A. Ourmazd, M. Scheffler, M. Heinemann and J-L. Rouviere, *Microscopic properties of thin films: Learning about point defects*, MRS Bulletin, pp. 24-31, December 1992

[15] J. Crank, *The mathematics of diffusion*, (Clarendon Press, 1975) Chapter 2

[16] B. Tuck, *Introduction to diffusion in semiconductors*, (IEE Monograph Series, Peter Peregrinus Ltd., 1974) Chapter 2

[17] E.H. Li and B.L. Weiss, *The optical properties of AlGaAs/GaAs hyperbolic quantum-well structures*, J. Appl. Phys., vol. **70**, pp. 1054-1056, 1991

[18] E.H. Li and B.L. Weiss, *The change in refractive index of AlGaAs/GaAs single quantum wells due to impurity-induced mixing*, IEEE Photon. Techn. Lett., vol. **3**, pp. 787-789, 1991

[19] E.H. Li and B.L. Weiss, *Analytical solution of the subbands and absorption coefficients of AlGaAs-GaAs hyperbolic quantum wells*, IEEE J. of Quant. Elec., vol. **29**, pp. 311-321, 1993

[20] P. Morse and H. Feshbach, *Methods of theoretical physics*, (McGraw-Hill, 1953) Chapter 6, pp. 768-769

[21] E.H. Li, B.L. Weiss and K.S. Chan, *Effect of interdiffusion on the subbands in an $Al_xGa_{1-x}As/GaAs$ single-quantum-well structure*, Phys. Rev. B, vol. **46**, pp. 15181-15192, 1992

[22] T.E. Schlesinger, T. Kuech, *Determination of the interdiffusion of Al and Ga in undoped (Al,Ga)As/GaAs quantum wells*, Appl. Phys. Lett., vol. **49**, pp. 519-521, 1986

[23] I.V. Bradley, W.P. Gillin, K.P. Homewood and R.P. Webb, *The effects of ion implantation on the interdiffusion coefficients in $In_xGa_{1-x}As/GaAs$ quantum well structures*, J. Appl. Phys., vol. **73**, pp. 1686-1692, 1993

[24] S.I. Hansen, *The refractive index change in GaAs-AlGaAs quantum wells by neutral impurity induced disordering using boron and fluorine*, PhD Thesis, 1993

[25] A.T. Meney, *Exciton binding energies and absorption in intermixed GaAs-AlGaAs quantum wells*, J. Appl. Phys., vol. **72**, pp. 5729-5734, 1992

[26] A.T. Meney, *Effects of impurity induced disorder on the index of refraction in GaAs-AlGaAs quantum wells*, Superlattices and Microstructures, vol. **11**, pp. 47-53, 1992

[27] E.H. Li, B.L. Weiss, K.S. Chan and J. Micallef, *Polarization dependent refractive index of an interdiffusion induced AlGaAs/GaAs quantum well*, Appl. Phys. Lett., vol. **62**, pp. 550-552, 1993

5 Asymmetric-Step Quantum Wells

5.1 Introduction

Nonlinear-optical properties of quantum wells and superlattices have attracted a great deal of attention in the technological area of optical switching and routing. Many of the potential devices that have been suggested need a material with an intensity-dependent refractive index coefficient ($n=n_0+n_2I$), which originates from various $\chi^{(3)}$ processes, in order to achieve a field dependent phase shift. Speed and low switching power are the requirements for efficient optical signal processing device [1]. However, it has been difficult to find materials that combine high enough nonlinearities (n_2) and low enough losses (α) to make picosecond all-optical switching devices. A lot of effort has been concentrated in improving the nonlinear properties of the different materials and proposing new geometries that enhance the performance of the switching devices [2]. Recently there has been increasing interest in obtaining large nonlinear phase shifts, by an effective intensity dependent refractive index, n_2, using second-order nonlinearities. The presence of these phase shifts was originally investigated and demonstrated experimentally in Ref. [3] and [4]. The nonlinear phase shifts arise as down-conversion of the second harmonic 2ω, away from perfect phase matching, to the fundamental. The second harmonic is in general out of phase with the fundamental source field at ω. This process has been termed *cascaded* as it involves the consecutive application of second order nonlinearities $\chi^{(2)}(\omega,\omega):\chi^{(2)}(-\omega,2\omega)$.

5.2 Cascading process

The cascading approach is a promising way to obtain large (multiple values of π) field dependent phase shift of the fundamental beam, under a variety of conditions [5], without absorptive losses [6]. Phase shifts of the order of π to 2π have been observed in quasi-phase-matched KTP waveguides, due to cascaded second-order processes [7]. Quasi-phase matching is a technique essential for the cascaded process in order to obtain nonlinear phase shifts. The cascaded process depends on down-conversion of the second-harmonic to the fundamental and at perfect matching conditions this effect would not be possible, since at these conditions the optical power from the fundamental field is transferred to the second-harmonic (figure 5.1). In order to obtain large phase-shifts the relative phase has to be corrected at regular intervals using a structural periodicity built into the nonlinear medium $\chi^{(2)}(\omega,\omega):\chi^{(2)}(-\omega,2\omega)$ (figure 5.2).

It has been shown that this approach can be used to implement nonlinear all-optical switching devices such as the Mach-Zehnder interferometer, the directional coupler [8]-[9] and the push-pull switch [10]. The basic configuration of the Mach-Zehnder interferometer is shown in figure 5.3(a). The incident field is split into two and both fields undergo independent phase shifts until they recombine to produce an output. The purpose of a nonlinear Mach-Zehnder interferometer is to change the relative phase by changing the input power. The nonlinear directional coupler (figure 5.3(b)) has two separate inputs and the waveguides are sufficiently close to permit energy exchange between the channels due to spatial field overlap. After half beat length a signal input into one channel exits from the other. For all-optical switches the relative channel outputs are changed by increasing the input power.

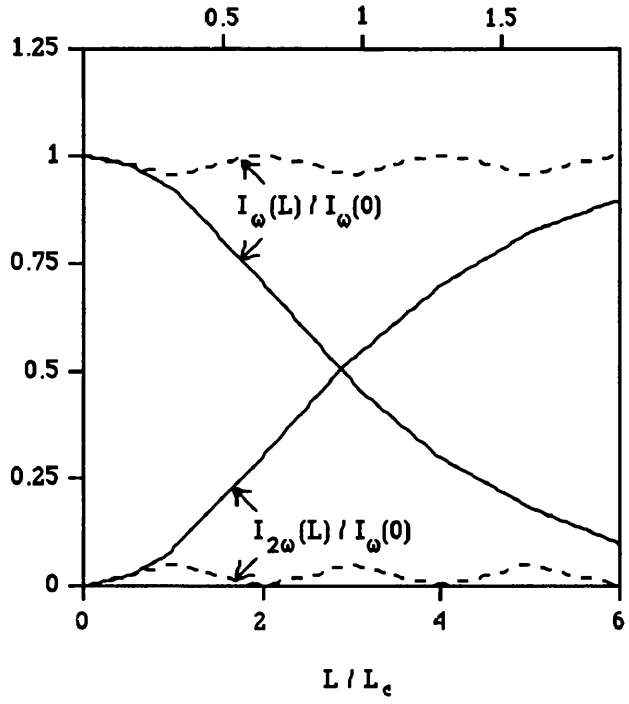

Figure 5.1. Normalised plots of second-harmonic intensity $I_{2\omega}$ and fundamental intensity I_ω versus length of medium L for perfect phase matching (continuous curves and upper horizontal scale) and for finite phase mismatch (dashed curves and lower horizontal scale) [11].

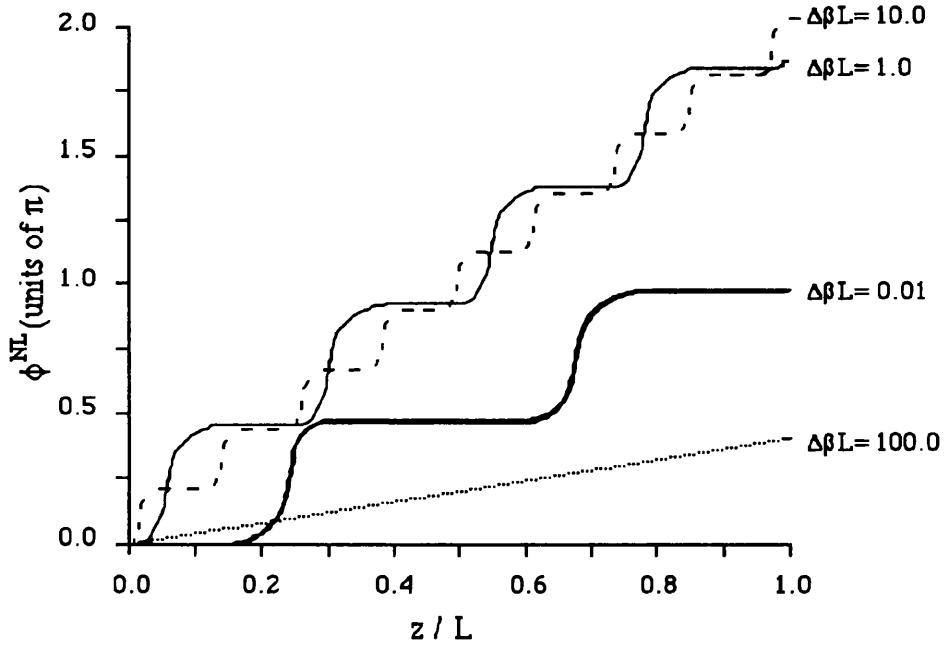

Figure 5.2. Variation in the nonlinear phase shift ϕ^{NL} with z for different detunings $\Delta\beta L$=0.01, 1.0, 10, 100. Here κL=4 [5].

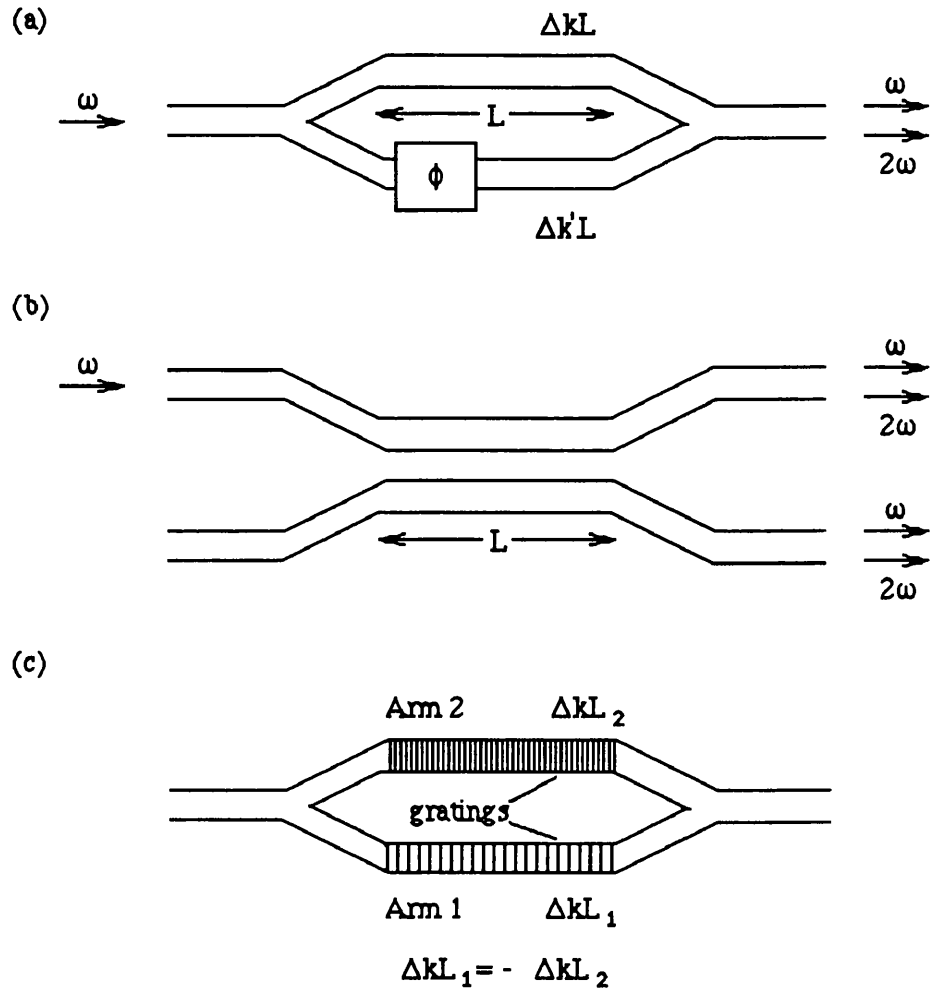

Figure 5.3. All-optical switching devices.

The push-pull switch (figure 5.3(c)) is based on a Mach-Zehnder interferometer, where quasi-phase matching produces a nonlinear phase shift with a different sign in each arm of the interferometer.

It is essential for the implementation of the cascaded effective n_2 to use materials with large second-order nonlinearities. These materials are required to crystallise in non-centrosymmetric space groups, in which $\chi^{(2)}$ is non vanishing by symmetry [12].

5.3 Asymmetric quantum wells

Large third-order nonlinearities have been observed in bulk and quantum well semiconductors and efficient fast switching devices have been demonstrated [13]-[14]. However most semiconductors, which crystallise in zinc-blende structures, have a point symmetry $\bar{4}3m$, and their second order susceptibility has a single nonzero independent component $\chi_{xyz}^{(2)}$ ($d_{14}=0.5\chi_{xyz}^{(2)}=0.208\pm0.022$nm/V for GaAs at the transparency region, below the optical energy gap) [15]. This restricts the choice of orientations for the applied and produced fields. In addition zinc-blende structures do not exhibit birefringence and hence conventional phase-matching is not possible. Symmetric quantum well structures possess inversion symmetry, therefore $\chi^{(2)}$ for these structures is equal to the bulk susceptibility d_{14}.

In order to be able to fabricate useful semiconductor devices, with large second order nonlinearities and tensor components in different directions various designs have been suggested. These are based on the fact that it is possible to remove the inversion symmetry of quantum wells, by using built-in asymmetric quantum-well systems, such as graded wells, step wells, or two coupled asymmetric wells, or symmetric quantum wells with applied external electric field (figure 5.4). Large susceptibilities $\chi^{(2)}$ have been predicted and observed, at different working wavelengths.

A large number of the published theoretical calculations [16]-[18] and observations [19]-[22] are concerned with nonlinear second-order susceptibilities based solely on intersubband transitions. For the intersubband transitions the second-harmonic susceptibility in the 10μm range has been predicted to reach values of the order of 960nm/V, which are in close agreement with those measured [20].

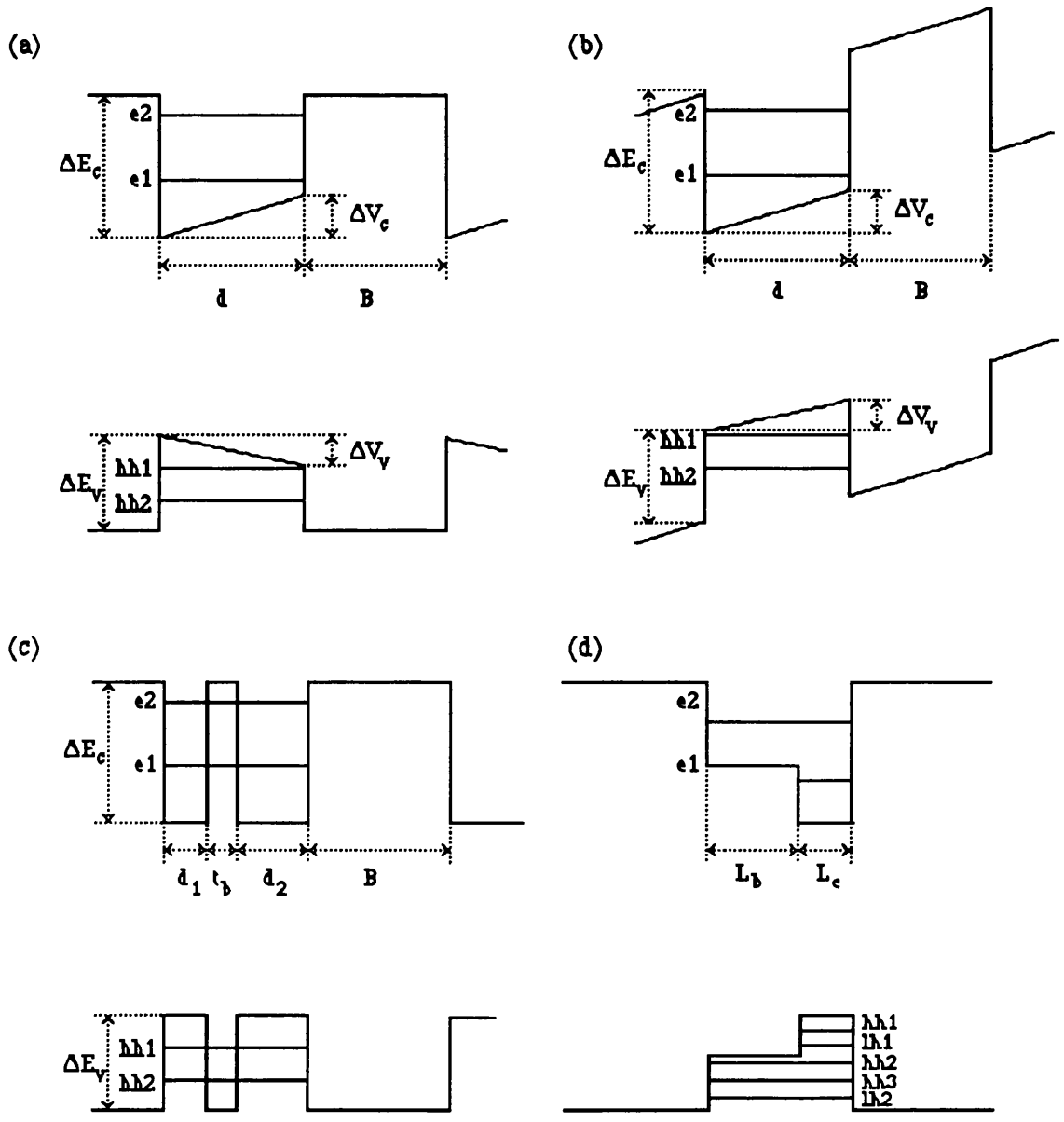

Figure 5.4. Asymmetric quantum well structrures: (a) graded quantum well, (b) symmetric quantum well with applied electric field, (c) asymmetric coupled quantum wells, (d) asymmetric-step quantum well.

Processes involving interband transitions between conduction band and heavy hole valence band subbands have been focused on one nonvanishing second-harmonic coefficient, $\chi_{xzx}^{(2)}$ [23]-[26], with a predicted magnitude close to 110pm/V in the 1.5μm range [25], which is larger than that of $LiNbO_3$ ($\chi_{xzx}^{(2)}$=10.1pm/V).

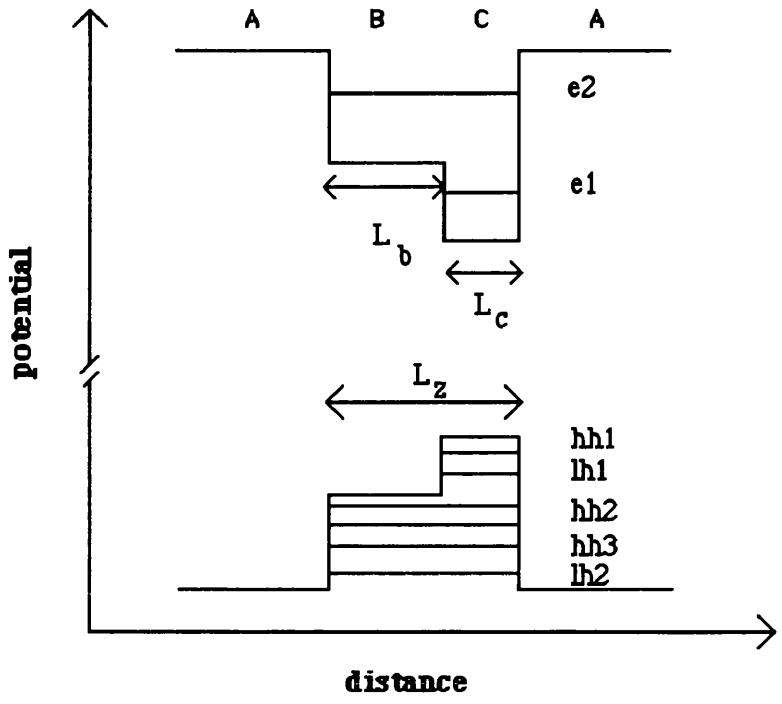

Figure 5.5. Asymmetric step quantum well.

An *asymmetric two-step* GaAlAs quantum well (figure 5.5) is a promising way of obtaining large second-order nonlinearities. The advantages of introducing such an asymmetry is that there is no requirement for applying continuously an external field to sustain the asymmetry and that it is easier to fabricate than the graded quantum well. It can be demonstrated that for an asymmetric two-step quantum well a second-order susceptibility tensor $\chi_{zzz}^{(2)}$ (d_{33}) exists. The utilisation of the $\chi_{xzx}^{(2)}$ (d_{15}) coefficient in a waveguide geometry requires the excitation of both TE and TM modes. On the other hand the $\chi_{zzz}^{(2)}$ (d_{33}) coefficient would permit only the excitation of the TM mode. Therefore a component of the susceptibility tensor in the (zzz) direction would ease the cascaded process, since only one input electric field is needed to generate the second harmonic and the second harmonic emerges from the same direction as the input field: $TM_{00}(\omega)+TM_{00}(\omega)\rightarrow TM_{00}(2\omega)$ (figure 5.6).

Moreover the use of structurally induced second-order nonlinearities widens the possible phase matching techniques. Domain reversal is feasible by inverting the asymmetric quantum wells. This may be difficult to achieve in semiconductors since fabrication procedures would require periodic etching and regrowth of the structure, increasing the propagation losses considerably. Other methods of inducing a modulation in the nonlinear susceptibility have been suggested. These would involve the techniques of periodic quantum well disordering [27] or orientational patterning [28]. With these methods the nonlinear coefficient can be modulated from a maximum value to zero. These techniques seem more viable compared to domain reversal, but result in a reduction of the effective nonlinear coefficient by a factor of 2.

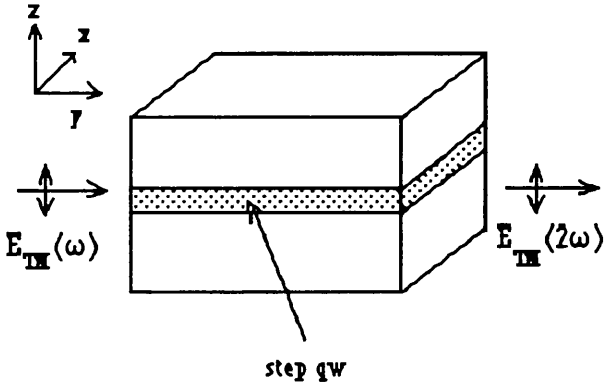

Figure 5.6. Schematic of a semiconductor device suitable for the application of the cascaded second-order nonlinear approach

The asymmetric quantum well consists of two thin layers of $Ga_{1-x}Al_xAs$ semiconductor material B and C, with different well thicknesses L_b and L_c (total well width $L_z=L_b+L_c$) and Al concentrations x_b and x_c (figure 5.5). A monochromatic input wave of frequency ω, at below one half of the bandgap, excites an electric field at the second harmonic frequency 2ω. We can design the semiconductor so that, for an input frequency $\hbar\omega=0.8$eV ($\lambda=1.55\mu$m), the second harmonic $2\hbar\omega=1.6$eV ($\lambda/2=0.77\mu$m) falls in the vicinity of

transition frequencies of the medium, but at the same time at a large enough wavelength so that the second harmonic is not absorbed.

5.4 Derivation of the expression for $\chi_{zzz}^{(2)}(-2\omega;\omega,\omega)$

An expression for the second-order susceptibility $\chi_{\mu\alpha\beta}^{(2)}(-2\omega;\omega,\omega)$ was obtained in chapter 3 from the density matrix formalism,

$$\chi_{\mu\alpha\beta}^{(2)}(2\omega;\omega,\omega) = \frac{1}{4\pi\varepsilon_0\hbar^2 L_z}\mathbf{S}_T \int_{\substack{0 \\ (\mathbf{k}_{||}\in 1^{st}\,B.Z)}}^{k_{max}} dk\, k \sum_{\ell,m,n}\{f_v(E_\ell)[1-f_c(E_m)]\} \left[\frac{\langle\psi^\ell|er_\mu|\psi^m\rangle\langle\psi^m|er_\alpha|\psi^n\rangle\langle\psi^n|er_\beta|\psi^\ell\rangle}{\{\Omega^{m\ell}(k)-2\omega\pm i\gamma_{m\ell}\}\{\Omega^{n\ell}(k)-\omega\pm i\gamma_{n\ell}\}}\right] \tag{5.1}$$

$\mathbf{S}_T$ is the total symmetrisation operator denoting that the expression is summed over all the 6 possible permutations of the pairs $(\mu,-2\omega)$, (α,ω), (β,ω), illustrated by the Feynman diagrams in figure 5.7. L_z is the quantum well width. $\langle\psi^i|er_\nu|\psi^j\rangle$ are the dipole-moment matrix elements, where ψ^i, ψ^j are the wavefunction of the i,j bands i,j=n,m,ℓ and the greek letters $\nu=\mu,\alpha,\beta$ take the values x,y,z. $\Omega^{m\ell}=[E^m(\mathbf{k}_{||})-E^\ell(\mathbf{k}_{||})]/\hbar$ and $\Omega^{n\ell}=[E^n(\mathbf{k}_{||})-E^\ell(\mathbf{k}_{||})]/\hbar$ are the transition frequencies between the bands with energy levels $E^i(\mathbf{k}_{||})$. $\gamma_{m\ell}$ and $\gamma_{n\ell}$ are the linewidth parameters of the density matrix formalism and the sign associated with these parameters is determined by the principle of causality mentioned in chapter 3. The energy levels are functions of the in-plane wavevector $\mathbf{k}_{||}=(k_x,k_y)$. $f_c(E_m)$ and $f_v(E_\ell)$ are the Fermi functions of the conduction subband E_m and the valence subband E_ℓ.

For an intrinsic semiconductor we can assume that the conduction band is empty and the valence band is full and so $f_v(E_\ell)[1-f_c(E_m)]\approx 1$. The second-order susceptibility is

designed to be near-resonant to the band-gap energy ($2\hbar\omega<E_g$) and so it is a good approximation for the calculation of $\chi_{zzz}^{(2)}$ to keep only the resonant terms. These are described by the permutations (1) and (2) in figure 5.7, where the ground state ℓ is in the valence band and the states m,n in the conduction band. Following these assumptions the expression for $\chi_{\mu\alpha\beta}^{(2)}(-2\omega;\omega,\omega)$ can be reduced to,

$$\chi_{\mu\alpha\beta}^{(2)}(2\omega;\omega,\omega) = \frac{1}{4\pi\varepsilon_0\hbar^2 L_z} \int_{\substack{0 \\ (\mathbf{k}_{||}\in 1^{st}\,B.Z)}}^{k_{max}} dk\, k \sum_{\ell,m,n} \left[\frac{\langle \psi_v^\ell | er_\mu | \psi_c^m \rangle \langle \psi_c^m | er_\alpha | \psi_c^n \rangle \langle \psi_c^n | er_\beta | \psi_v^\ell \rangle}{(\Omega_{cv}^{m\ell} - 2\omega - i\gamma_{m\ell})(\Omega_{cv}^{n\ell} - \omega - i\gamma_{n\ell})} + \frac{\langle \psi_v^\ell | er_\mu | \psi_c^m \rangle \langle \psi_c^m | er_\beta | \psi_c^n \rangle \langle \psi_c^n | er_\alpha | \psi_v^\ell \rangle}{(\Omega_{cv}^{m\ell} - 2\omega - i\gamma_{m\ell})(\Omega_{cv}^{n\ell} - \omega - i\gamma_{n\ell})} \right] \tag{5.2}$$

and since both terms are the same,

$$\chi_{zzz}^{(2)}(-2\omega;\omega,\omega) = \frac{1}{\varepsilon_0 L_z} \frac{1}{2\pi\hbar^2} \sum_{\ell,m,n} \int_{\substack{0 \\ (\mathbf{k}_{||}\in 1^{st}\,B.Z)}}^{k_{max}} dk\, k \frac{\langle \psi_v^\ell | ez | \psi_c^m \rangle \langle \psi_c^m | ez | \psi_c^n \rangle \langle \psi_c^n | ez | \psi_v^\ell \rangle}{(\Omega_{cv}^{m\ell} - 2\omega - i\gamma_{m\ell})(\Omega_{cv}^{n\ell} - \omega - i\gamma_{n\ell})} \tag{5.3}$$

Following the same procedure an expression for the susceptibility tensor $\chi_{xzx}^{(2)}(-2\omega;\omega,\omega)$ can be obtained,

$$\chi_{xzx}^{(2)}(-2\omega;\omega,\omega) = \frac{1}{\varepsilon_0 L_z} \frac{1}{2\pi\hbar^2} \sum_{\ell,m,n} \int_{\substack{0 \\ (\mathbf{k}_{||}\in 1^{st}\,B.Z)}}^{k_{max}} dk\, k \frac{\langle \psi_v^\ell | ex | \psi_c^m \rangle \langle \psi_c^m | ez | \psi_c^n \rangle \langle \psi_c^n | ex | \psi_v^\ell \rangle}{(\Omega_{cv}^{m\ell} - 2\omega - i\gamma_{m\ell})(\Omega_{cv}^{n\ell} - \omega - i\gamma_{n\ell})} \tag{5.4}$$

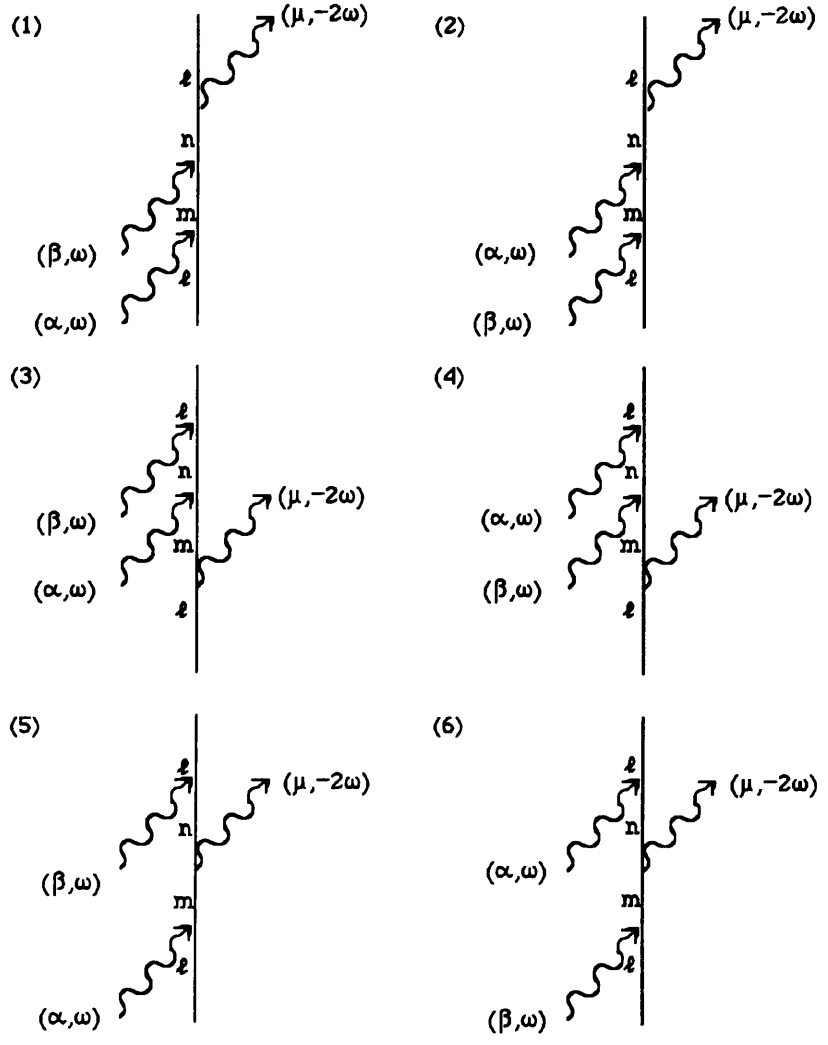

Figure 5.7. Feynman diagrams illustrating the 6 permutations involved in the determination of $\chi^{(2)}$

5.5 Band structure calculations

The wavefunctions ψ^i and the energy levels $E^i(\mathbf{k}_{\|})$, i=c,hh,lh, can be calculated from the envelope function scheme described in chapter 2. The same assumptions hold for the conduction and valence bands:

(i)In GaAlAs heterostructures the coupling, due to the quantum well potential, between the conduction band (Γ_6) and the valence band is relatively weak.

(ii)The split-off band (Γ_7) can be discarded from the calculations, because the energy split Δ ($\Delta=E_{\Gamma 8}-E_{\Gamma 7}=0.341$ eV in GaAs) is relatively large.

(iii)The heavy-hole and the light-hole bands (Γ_8) are strongly intermixed due to coupling.

The same boundary conditions for the envelope functions must be applied also at the interfaces of the heterostructure materials.

Figure 5.8 shows the in-plane dispersion relations of the valence band for an asymmetric step quantum well with 40Å $Ga_{0.85}Al_{0.15}As$ and 60Å $Ga_{0.67}Al_{0.33}As$ wells within $Ga_{0.52}Al_{0.48}As$ barriers, calculated from the envelope function approximation with band-mixing. These can be compared with the results obtained from the parabolic band approximation, shown in figure 5.9 for the same step well. As can be seen the crossings of the hh and lh bands in the parabolic band model have been substituted with anti-crossings in the valence-band mixing model, resulting in strongly non-parabolic hh and lh subbands. It is of importance to notice that the energy levels in the parabolic band approximation are twice degenerate, while for the band-mixing model away from $\mathbf{k}_{||}=0$ this two-fold degeneracy (Kramers degeneracy) is lifted as can be observed in figure 5.8. This is due to the quantum well sturcture inversion asymmetry.

5.6 Interband and intraband matrix elements

In the expressions (5.3) and (5.4) the dipole-moment matrix elements $\langle\psi_i|er_\mu|\psi_j\rangle$ $\mu=x,y,z$, between bands i and j (i,j=c,lh,hh) are equivalent to the integral,

$$\left\langle \psi_i \middle| er_\mu \middle| \psi_j \right\rangle = e\int \psi_i^*(\mathbf{r})\, r_\mu\, \psi_j(\mathbf{r})\, d\mathbf{r} \tag{5.5}$$

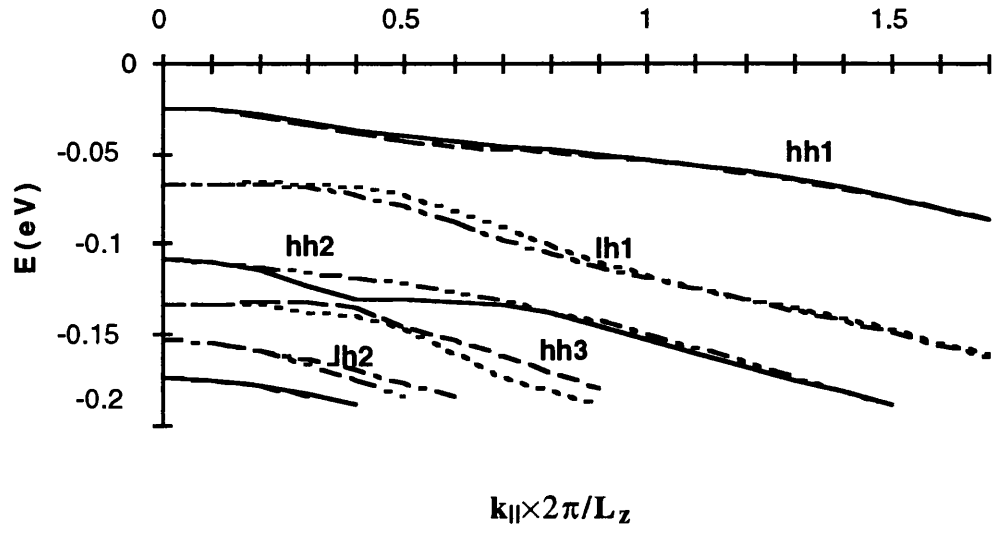

Figure 5.8. Band-mixing approximation in-plane dispersion relations of the valence band for an asymmetric step quantum well with 40Å $Ga_{0.85}Al_{0.15}As$ and 60Å $Ga_{0.67}Al_{0.33}As$ wells within $Ga_{0.52}Al_{0.48}As$ barriers

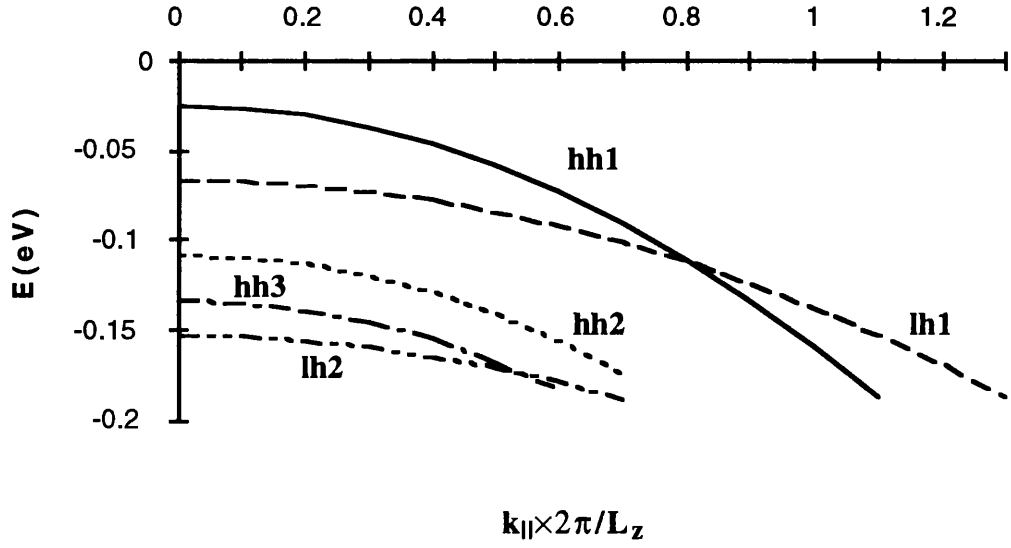

Figure 5.9. Parabolic approximation in-plane dispersion relations of the valence band for an asymmetric step quantum well with 40Å $Ga_{0.85}Al_{0.15}As$ and 60Å $Ga_{0.67}Al_{0.33}As$ wells within $Ga_{0.52}Al_{0.48}As$ barriers

The intraband $\langle\psi_c^m|ez|\psi_c^n\rangle$ dipole-moment matrix element involves transitions between two states of the conduction band and the interband $\langle\psi_v^\ell|er_\mu|\psi_c^m\rangle$ and $\langle\psi_c^n|er_\mu|\psi_v^\ell\rangle$ matrix elements involve transitions between the conduction band and the valence band and so they are going to be treated differently. The wavefunctions ψ_i, i=c,hh,lh are given by the expressions (2.20) and (2.22),

$$\psi_i(\mathbf{r}) = f_i(\mathbf{r})\, u_{i0}(\mathbf{r}) = \frac{1}{\sqrt{S}} e^{i\mathbf{k}_{\|}\cdot\mathbf{r}_{\|}} \phi_i(z) u_{i0}(\mathbf{r}) \tag{5.6}$$

The Bloch functions u_i are orthonormal and hence for the intraband transitions the expression for the dipole-moment matrix element is reduced to (Appendix B),

$$\left\langle \psi_c^m \middle| ez \middle| \psi_c^n \right\rangle = e\left\langle \phi_c^m \middle| z \middle| \phi_c^n \right\rangle = e\int_{-\infty}^{+\infty} \phi_c^{*\,m}(z)\, z\, \phi_c^n(z)\, dz \tag{5.7}$$

The expression for the interband transition is (Appendix B),

$$\left\langle \psi_v^\ell \middle| er_\mu \middle| \psi_c^m \right\rangle = \left\langle u_v \middle| er_\mu \middle| u_c \right\rangle \left\langle \phi_v^\ell \middle| \phi_c^m \right\rangle = \left\langle u_v \middle| er_\mu \middle| u_c \right\rangle \int_{-\infty}^{+\infty} \phi_v^{\ell *}(z)\, \phi_c^m(z)\, dz \tag{5.8}$$

Interband transitions are restricted by selection rules. The z interband dipole-moment matrix element is non-zero only for transitions between the light hole band and the conduction band. This selection rule is only valid at the zone centre $\mathbf{k}_{\|}=0$. Away from the zone centre, $\mathbf{k}_{\|}\neq 0$, due to the valence subband mixing described earlier, the heavy hole band wavefunctions exhibit partially a light hole-like behaviour. As a result, transitions between the heavy hole and the conduction band are allowed at $\mathbf{k}_{\|}\neq 0$. The value of the dipole moment matrix element between the periodic part of the Bloch functions is equal to,

$$\langle u_{lh}|\,ez\,|u_c\rangle = \frac{2}{\sqrt{6}}\langle S|\,ez\,|Z\rangle \approx -\frac{2}{\sqrt{6}}\frac{e}{E_g}P$$

(5.9)

The factor $2/\sqrt{6}$ is obtained by the Kane model [29] and P is the interband matrix element of the velocity operator given by the expression (3.49). Substituting the terms for the interband and intraband matrix elements in the expression (5.3) for $\chi_{zzz}^{(2)}$, we finally obtain,

$$\chi_{zzz}^{(2)}(-2\omega;\omega,\omega) = \frac{e^3P^2}{3\pi\varepsilon_0 L_z E_g^2}\sum_{\ell,m,n}\int_{\substack{0\\(k_{||}\in 1^{st}\,B.Z)}}^{k_{max}} dk\,k\,\frac{\langle\phi_v^\ell|\,\phi_c^m\rangle\langle\phi_c^m|\,z\,|\phi_c^n\rangle\langle\phi_c^n|\,\phi_v^\ell\rangle}{(E_{cv}^{m\ell}(\mathbf{k}_{||}) - 2\hbar\omega - i\hbar\gamma_{m\ell})(E_{cv}^{n\ell}(\mathbf{k}_{||}) - \hbar\omega - i\hbar\gamma_{n\ell})}$$

(5.10)

The envelope function approximation is accurate only at the vicinity of the zone centre and not in the entire Brillouin zone, but this does not create any problem since the integral in the expression (5.10) converges at a wavenumber equal to approximately 10% of the Brillouin zone.

The x interband dipole-moment matrix element is non-zero for the transitions between the heavy hole subbands and the conduction band as well as the light hole subbands and the conduction band. The value of the dipole moment matrix elements between the periodic part of the Bloch functions is equal to,

$$\langle u_{hh}|\,ex\,|u_c\rangle = \frac{1}{\sqrt{2}}\langle S|\,ex\,|X\rangle \approx -\frac{1}{\sqrt{2}}\frac{e}{E_g}P$$

(5.11)

$$\langle u_{lh}|\,ex\,|u_c\rangle = \frac{1}{\sqrt{6}}\langle S|\,ex\,|X\rangle \approx -\frac{1}{\sqrt{6}}\frac{e}{E_g}P$$

(5.12)

The factors $1/\sqrt{2}$ and $1/\sqrt{6}$ are similarly obtained from the Kane model.

Substituting the terms for the interband and intraband matrix elements in the expression (5.4) for $\chi_{xzx}^{(2)}$, we finally obtain,

$$\chi_{xzx}^{(2)}(-2\omega;\omega,\omega) = \frac{e^3P^2}{2\pi\varepsilon_0 L_z E_g^2}\sum_{\ell,m,n}$$

$$\int_{\substack{0\\(\mathbf{k}_{||}\in 1^{st}\,B.Z)}}^{k_{max}} dk\,k\,\frac{c_\ell^2\langle\phi_v^\ell|\,\phi_c^m\rangle\langle\phi_c^m|\,z\,|\phi_c^n\rangle\langle\phi_c^n|\,\phi_v^\ell\rangle}{(E_{cv}^{m\ell}(\mathbf{k}_{||})-2\hbar\omega-i\hbar\gamma_{m\ell})(E_{cv}^{n\ell}(\mathbf{k}_{||})-\hbar\omega-i\hbar\gamma_{n\ell})}$$

(5.13)

wher c_ℓ is equal to $c_\ell=(1/\sqrt{2})$ if ℓ is heavy hole and $c_\ell=(1/\sqrt{6})$ if ℓ is light hole.

5.7 Numerical results and discussion

The energy levels and the wavefunctions at $\mathbf{k}_{||}=0$ for both the conduction and the valence subbands are presented in figure 5.10 for the asymmetric step quantum well of figure 5.8, that is consisted of 40Å $Ga_{0.85}Al_{0.15}As$ and 60Å $Ga_{0.67}Al_{0.33}As$ wells within $Ga_{0.52}Al_{0.48}As$ barriers. The asymmetry introduced by the quantum well structure results in strongly asymmetric wavefunctions. The inversion symmetry is lifted and so the second-order susceptibility $\chi_{zzz}^{(2)}$ (d_{33}) can be generated.

An estimate for the order of $\chi_{zzz}^{(2)}$ of the asymmetric well can be computed from the expression (5.10). The results obtained are shown in figure 5.11 for the asymmetric step

quantum well with 40Å $Ga_{0.85}Al_{0.15}As$ and 60Å $Ga_{0.67}Al_{0.33}As$ wells within $Ga_{0.52}Al_{0.48}As$ barriers. The following parameters have been assumed; for the Luttinger parameters γ_1=6.85−3.4x, γ_2=2.1−1.42x and γ_3=2.9−1.61x, the effective mass for the conduction band $m_c^*=(0.067+0.058x)m_o$ and the linewidth parameters of the density matrix formalism $\gamma_{m\ell}=\gamma_{n\ell}$=0.007eV, corresponding to a dephasing time τ_d=60fs.

At the wavelength of interest, well bellow the absorption edge, the real part of $\chi_{zzz}^{(2)}$ is 100pm/V. This value is of the same order of magnitude to that of the bulk semiconductor, but with tensor components in a direction more suitable for the cascaded and most of the second-harmonic applications. The absorption coefficient and the refractive index change for this asymmetric step quantum well, calculated from the expressions in Chapter 3, are shown in figures 5.12 and 5.13. The absorption coefficient at the second-harmonic $2\hbar\omega$=1.6eV ($\lambda/2$=0.77μm), chosen to be well bellow the bandgap, is very small as expected. This is required in order to avoid the second-harmonic being absorbed. In figures 5.14 and 5.15 the second-order susceptibility $\chi_{zzz}^{(2)}$ was calculated for different well structures.

Comparison of the second-order susceptibility $\chi_{zzz}^{(2)}$ calculated from the band-mixing model and the parabolic band model is shown in figure 5.16. It is clear that value of the susceptibility estimated from the parabolic band model is smaller by a factor of 4. It is evident that it is of importance to use an accurate band structure model to describe the in-plane dispersion of the asymmetric quantum well. The envelope function method is a good approximation for GaAs-Ga(Al)As heterostructures. Further improvement can be accomplished by taking more band characteristics into account, like coupling of the valence band with the Γ_6 conduction band and inversion-asymmetry splitting, as well as higher order **k**-terms in the **k**·**p** perturbation method. Figure 5.17 shows the contribution of each of the distinct subband transitions, the sum of which make up the total of $\chi_{zzz}^{(2)}$. As can be

seen the transitions hh1-c1-c2 and hh1-c2-c1 contribute significantly, but the first resonance originates from the transition between lh1-c1-c2.

In figure 5.18 the second-order susceptibility tensor component $\chi_{zzz}^{(2)}$ calculated for the asymmetric step quantum well with 40Å $Ga_{0.85}Al_{0.15}As$ and 60Å $Ga_{0.67}Al_{0.33}As$ wells within $Ga_{0.52}Al_{0.48}As$ barriers is compared with the $\chi_{xzx}^{(2)}$ calculated for the same asymmetric step well from expression (5.13). As expected, because of the contribution from the heavy hole transitions, the second-order susceptibility tensor component $\chi_{xzx}^{(2)}$ is larger than $\chi_{zzz}^{(2)}$, but only by a factor of 2 at the wavelength of interest. This factor can be compensated by the reduced complexity of the waveguide geometry proposed, with the utilisation of the second-harmonic susceptibility component $\chi_{zzz}^{(2)}$.

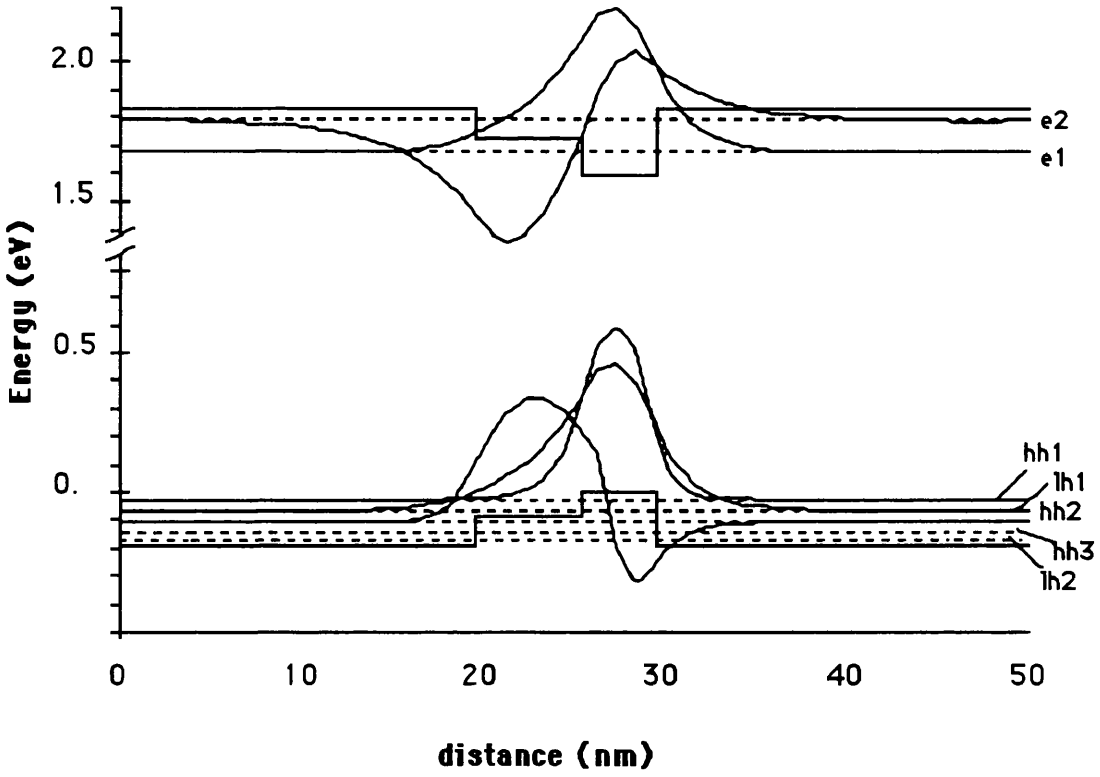

Figure 5.10. Energy levels and wavefunctions for an asymmetric step quantum well with 40Å $Ga_{0.85}Al_{0.15}As$ and 60Å $Ga_{0.67}Al_{0.33}As$ wells within $Ga_{0.52}Al_{0.48}As$ barriers at $\mathbf{k}_{||}=0$.

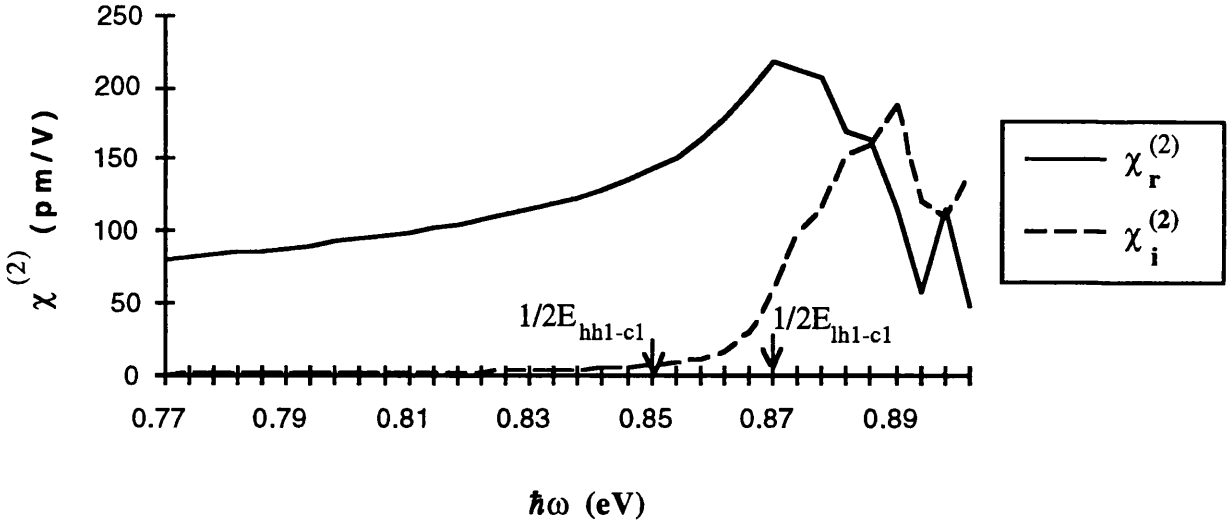

Figure 5.11. $\chi_{zzz}^{(2)}(-2\omega;\omega,\omega)$ for an asymmetric step quantum well with 40Å $Ga_{0.85}Al_{0.15}As$ and 60Å $Ga_{0.67}Al_{0.33}As$ wells within $Ga_{0.52}Al_{0.48}As$ barriers.

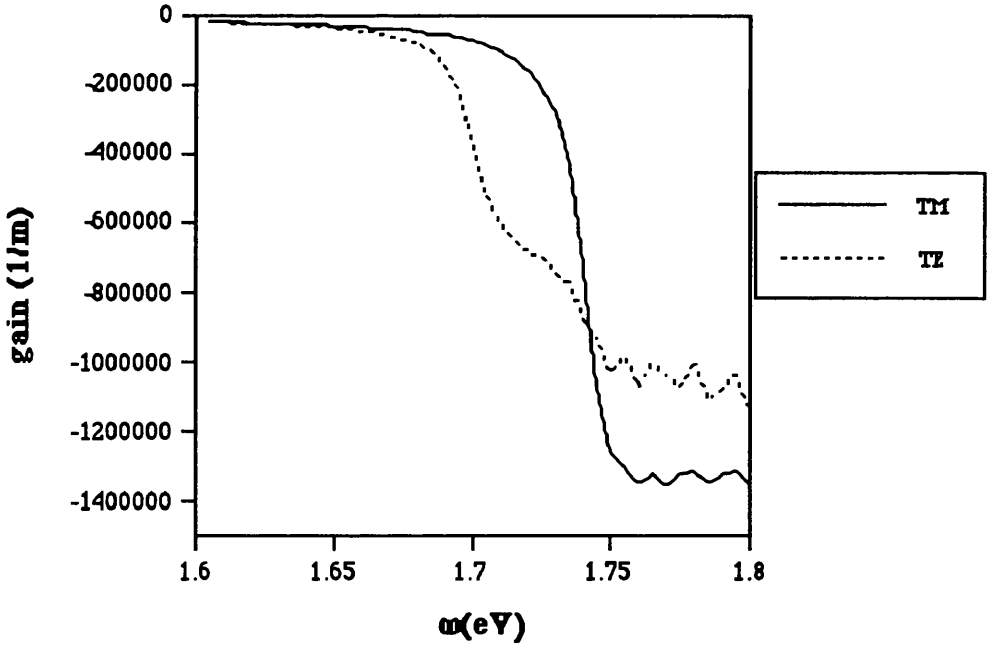

Figure 5.12. Absorption coefficient $\alpha(\omega)$ for an asymmetric step quantum well with 40Å $Ga_{0.85}Al_{0.15}As$ and 60Å $Ga_{0.67}Al_{0.33}As$ wells within $Ga_{0.52}Al_{0.48}As$ barriers.

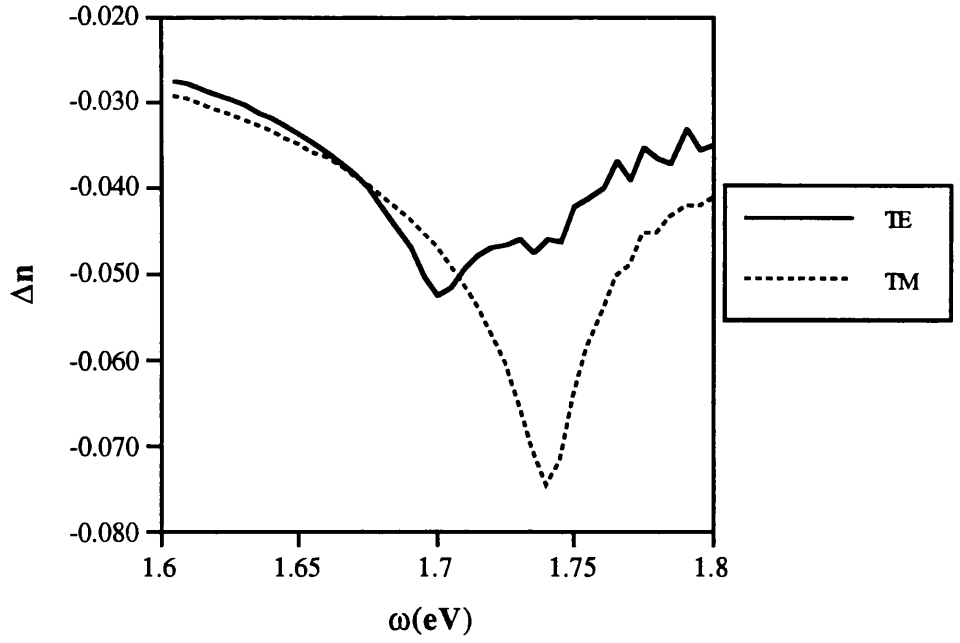

Figure 5.13. Refractive index change $\Delta n(\omega)$ for an asymmetric step quantum well with 40Å $Ga_{0.85}Al_{0.15}As$ and 60Å $Ga_{0.67}Al_{0.33}As$ wells within $Ga_{0.52}Al_{0.48}As$ barriers.

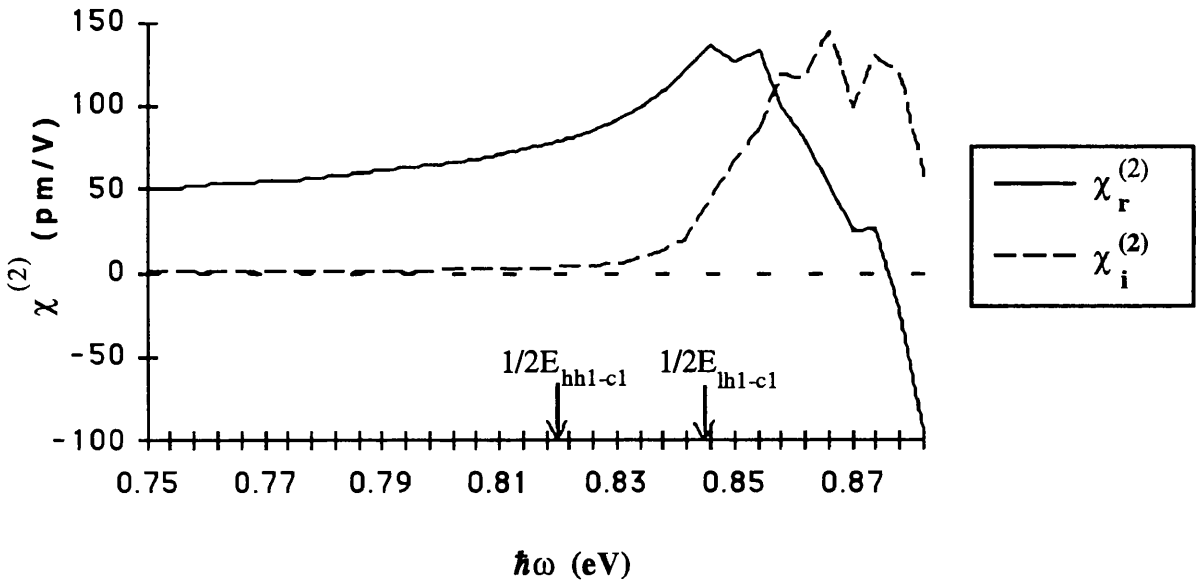

Figure 5.14. $\chi_{zzz}^{(2)}(-2\omega;\omega,\omega)$ for an asymmetric step quantum well with 40Å $Ga_{0.90}Al_{0.10}As$ and 60Å $Ga_{0.67}Al_{0.33}As$ wells within $Ga_{0.52}Al_{0.48}As$ barriers.

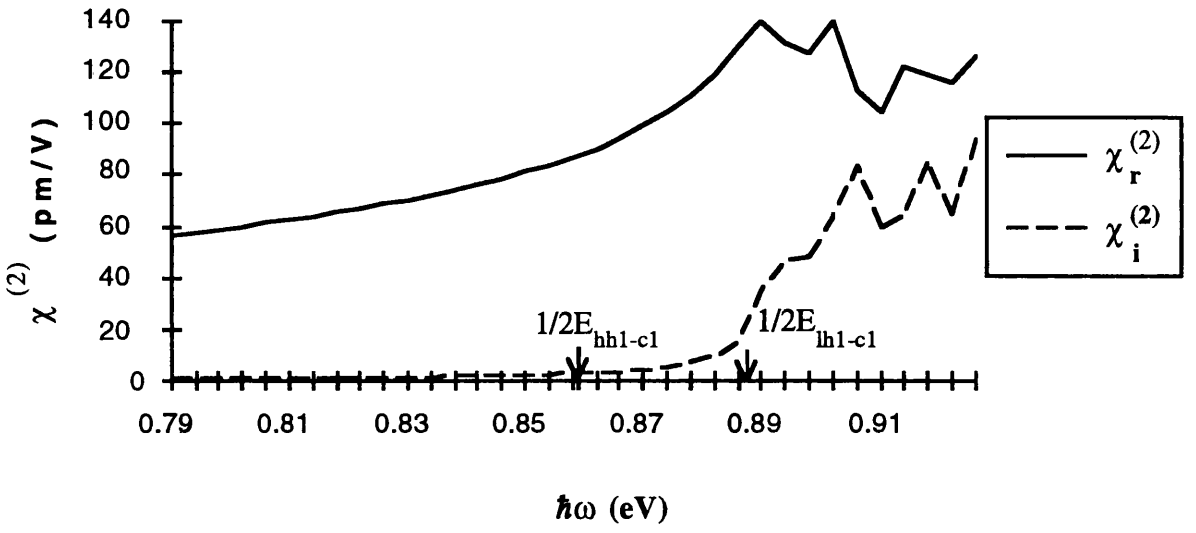

Figure 5.15. $\chi_{zzz}^{(2)}(-2\omega;\omega,\omega)$ for an asymmetric step quantum well with a 30Å $Ga_{0.90}Al_{0.10}As$ and a 60Å $Ga_{0.67}Al_{0.33}As$ within $Ga_{0.52}Al_{0.48}As$ barriers.

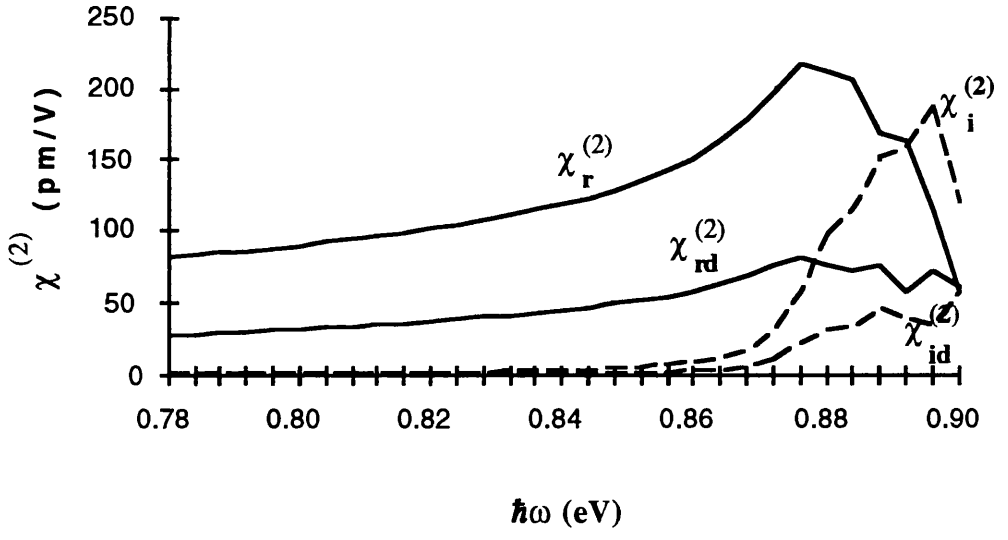

Figure 5.16. Comparison of the calculated $\chi_{zzz}^{(2)}(-2\omega;\omega,\omega)$ from the parabolic band model ($\chi_{rd}^{(2)}$ and $\chi_{id}^{(2)}$, real and imaginary parts respectively) and the band-mixing model ($\chi_r^{(2)}$ and $\chi_i^{(2)}$, real and imaginary parts respectively) for the asymmetric step quantum well with 40Å $Ga_{0.85}Al_{0.15}As$ and 60Å $Ga_{0.67}Al_{0.33}As$ wells within $Ga_{0.52}Al_{0.48}As$ barriers.

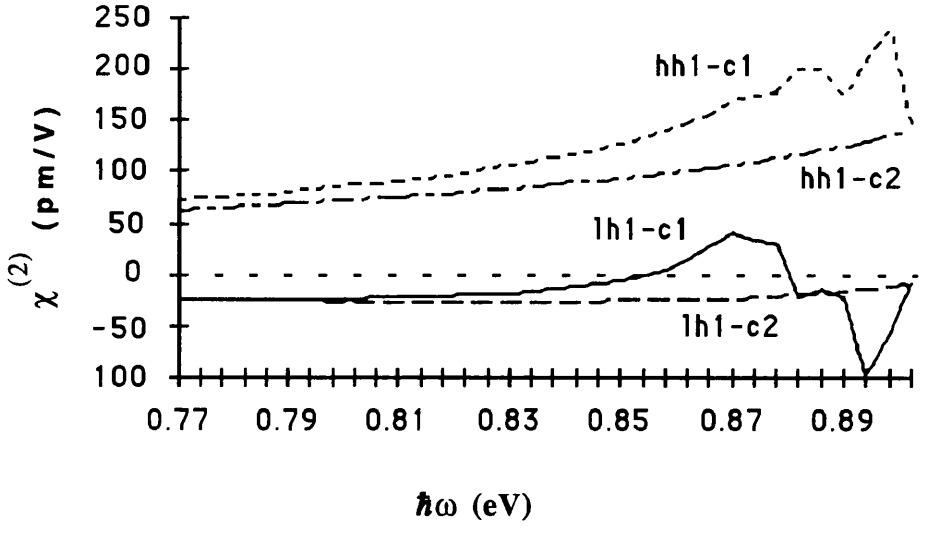

Figure 5.17. Contributions to the real part of $\chi_{zzz}^{(2)}(-2\omega;\omega,\omega)$ by the transitions between hh to conduction band and lh to conduction band for an asymmetric step quantum well with 40Å $Ga_{0.85}Al_{0.15}As$ and 60Å $Ga_{0.67}Al_{0.33}As$ wells within $Ga_{0.52}Al_{0.48}As$ barriers.

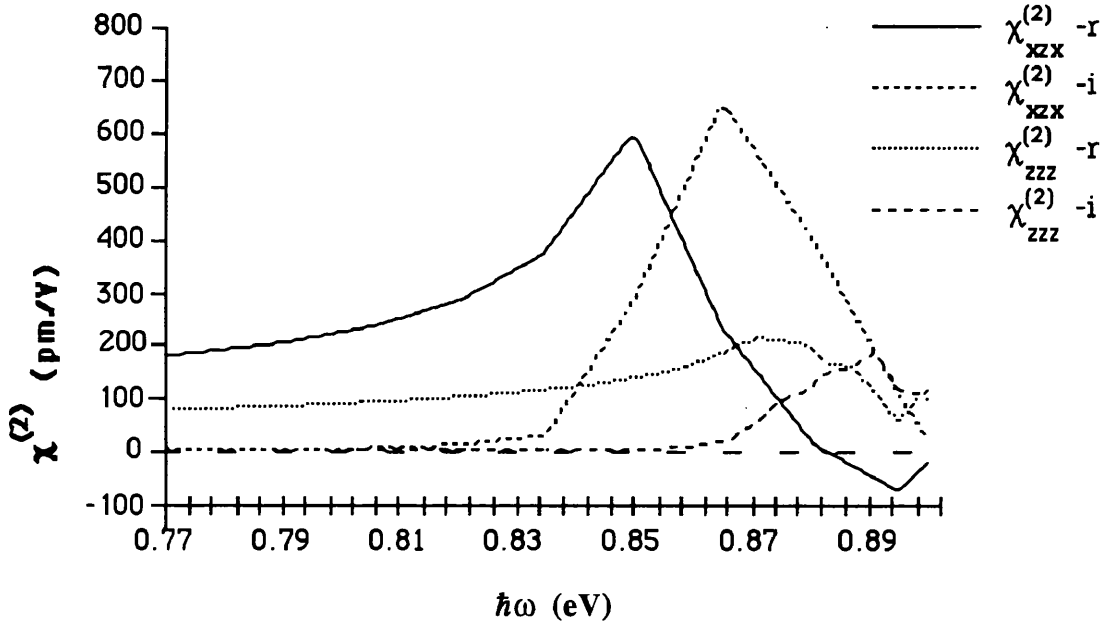

Figure 5.18. Comparison of the calculated $\chi_{zzz}^{(2)}(-2\omega;\omega,\omega)$ ($\chi_{zzz}^{(2)}$-r and $\chi_{zzz}^{(2)}$-i, real and imaginary parts respectively) and the $\chi_{xzx}^{(2)}(-2\omega;\omega,\omega)$ ($\chi_{xzx}^{(2)}$-r and $\chi_{xzx}^{(2)}$-i, real and imaginary parts respectively) for the asymmetric step quantum well with 40Å $Ga_{0.85}Al_{0.15}As$ and 60Å $Ga_{0.67}Al_{0.33}As$ wells within $Ga_{0.52}Al_{0.48}As$ barriers.

In the numerical calculations all the bound states were included. A further improvement can be obtained by including in the sum a number of the subbands that lie in the continuum. Moreover, optimising the asymmetric step well structure by varying the different well and barrier materials and well widths, can enhance the $\chi_{zzz}^{(2)}$ at a desired wavelength.

5.8 Conclusions

An asymmetric two-step GaAlAs quantum well was proposed appropriate for applications that employ the cascading second-order nonlinear effect which require a $\chi_{zzz}^{(2)}$ (d_{33}) second-order susceptibility tensor. The asymmetric quantum well consists of two thin layers of GaAlAs semiconductor material with different well thicknesses and Al concentrations. An estimate for the $\chi_{zzz}^{(2)}$ was obtained using the density matrix formalism and the envelope function approximation including the valence band-mixing model. It was shown that a $\chi_{zzz}^{(2)}$ (d_{33}) second-order susceptibility tensor is possible based on transitions between the light hole and light hole like valence band and the conduction band at a wavelength of 1.55μm. The magnitude of the $\chi_{zzz}^{(2)}$ was estimated to be of the same order of magnitude with that of the bulk GaAs material and $\chi_{xzx}^{(2)}$.

References

[1] Y. Silberberg and P.W. Smith, in *Nonlinear Photonics*, Vol.30 of *Springer Series in Electronics and Photonics*, edited by H.M. Gibbs, G. Khitrova, and N. Peyghambarian (Springer-Verlag 1990) Chapter 6

[2] D.F. Eaton, *Nonlinear Materials*, Science, vol. **253**, pp. 281-287, 1991

[3] N.R. Belashenkov, S.V. Garagarskii and M.V. Inochkin, *Nonlinear refraction of light on second-harmonic generation,* Opt. Spektrosk., vol. **66**, pp. 806-808, 1989

[4] R. DeSalvo, D.J. Hagan, M. Sheik-Bahae, G. Stegeman and E.W. Van Stryland, *Self-focusing and self-defocusing by cascaded second-order effects in KTP*, Opt. Lett., vol. **17**, pp. 28-30, 1992

[5] G.I. Stegeman, M. Sheik-Bahae, E. Van Stryland, and G. Assanto, *Large nonlinear phase shifts in second-order nonlinear-optical processes*, Opt. Lett., vol. **18**, pp. 13-15, 1993

[6] G.I. Stegeman, and E.M. Wright, *All-optical waveguide switching*, J. Opt. Quantum Electron., vol **22**, pp. 95-122, 1990

[7] M.L. Sundheimer, Ch. Bosshard, E.W. Van Styland, and G.I. Stegeman, *Large nonlinear phase modulation in quasi-phase-matched KTP waveguides as a result of cascaded second-order processes,* Opt. Lett., vol. **18**, pp.1397-1399, 1993

[8] G. Assanto, G.I. Stegeman,M. Sheik-Bahae, and E. Van Stryland, *All optical switching devices based on large nonlinear phase shifts from second harmonic generation,* Appl. Phys. Lett., vol. **62**, pp. 1323-1325, 1993

[9] D.C. Hutchings, J.S. Aitchison and C.N. Ironside, *All-optical switching based on nondegenerate phase shifts from a cascaded second-order nonlinearity*, Opt. Lett., vol. **18**, pp. 793-795, 1993

[10] C.N. Ironside, J.S. Aitchison and J.M. Arnold, *An all-optical switch employing the cascaded second-order nonlinear effect*, IEEE J. of Quant. Elec., vol. **29**, pp. 2650-2654, 1993

[11] P.N. Butcher and D. Cotter, *The elements of nonlinear optics*, (Cambridge University Press, 1991), p. 221

[12] C.Flytzanis, in *Quantum Electronics* Vol.1, part A, edited by H. Rabin and C.L.Tsang (Academic Press, 1975) Chapter 2, pp.24-25

[13] K. Al-Hemyari, J.S. Atchison, C.N. Ironside, G.T. Kennedy, R.S. Grant, and W. Sibbet, *Ultrafast all-optical switching in GaAlAs integrated interferometer in 1.55μm spectral region,* Electron. Lett., vol. **28**, pp.1090-1092, 1992

[14] J.S.Aitchison, A.Villeneuve, G.I. Stegeman, *All optical switching in a nonlinear GaAlAs X junction*, Opt. Lett., vol. **18**, pp. 1153-1155, 1993

[15] same as Ref. [12], p. 173

[16] J. Khurgin, *Second-order intersubband nonlinear-optical susceptibilities of asymmetric quantum-well structrures*, J. Opt. Soc. Am. B, vol. **6**, pp. 1673-1682, 1989

[17] S. Li, and J. Khurgin, *Second-order nonlinear optical susceptibility in p-doped asymmetric quantum wells*, Appl. Phys. Lett., vol. **62**, pp. 1727-1729, 1993

[18] L. Tsang, D. Ahn, and S.L. Chuang, *Electric field control of optical second-harmonic generation in a quantum well*, Appl. Phys. Lett., vol. **52**, pp. 697-699, 1988

[19] E. Rosencher, P. Bois, J. Nagle, E. Costard, and S. Delaitre, *Observation of nonlinear optical rectification at 10.6μm in compositionally asymmetrical AlGaAs multiquantum wells*, Appl. Phys. Lett., vol. **55**, pp. 1597-1599, 1989

[20] S.J Yoo, M.M. Fejer, and R.L. Byer, *Second-order susceptibility in asymmetric quantum wells and its control by proton bombardment*, Appl. Phys. Lett., vol. **58**, pp. 1724-1726, 1991

[21] P. Boucaud, F.H. Julien, D.D. Yang, J.-M. Lourtioz, E.Rosencher, P.Bois and J. Nagle, *Detailed analysis of second-harmonic generation near 10.6μm in GaAs/AlGaAs asymmetric quantum wells*, Appl. Phys. Lett., vol. **57**, pp. 215-217, 1990

[22] Z. Chen, M. Li, D. Cui, H. Lu, and G. Yang, *Surface-emitting second-harmonic generation by intersubband transition in asymmetric quantum wells with slab waveguides,* Appl. Phys. Lett., vol. **62**, pp. 1502-1503, 1993

[23] J. Khurgin, *Second-order susceptibilility of asymmetric coupled quantum well structures*, Appl. Phys. Lett., vol. **51**, pp. 2100-2102, 1987

[24] J. Khurgin, *Second-order nonlinear effects in asymmetric quantum-well structures*, Phys. Rev. B, vol. **38**, pp. 4056-4066, 1988

[25] L. Tsang, S-L Chuang and S.M. Lee, *Second-order nonlinear optical susceptibility of a quantum well with an applied electric field*, Phys. Rev. B, vol. **41**, pp. 5942-5951, 1990

[26] P.J. Harshman and S. Wang, *Asymmetric AlGaAs quantum wells for second-harmonic generation and quasiphase matching of visible light in surface emitting waveguides*, App. Phys. Lett., vol. **60**, pp. 1277-1279, 1992

[27] J.H. Marsh, *Quantum well intermixing*, Semicond. Sci. Technol., vol. **8**, pp.1136-1155, 1993

[28] M.J. Angell, R.M. Emerson, J.L. Hoyt, J.F. Gibbons, M.L. Bortz, L.A. Eyres, and M.M. Fejer, *Orientation patterning of II-VI semiconductor films for quasi-phasematched nonlinear devices*, in *Digest of Conference on Integrated Photonics Research* (Optical Society of America, 1993), paper IWC5

[29] E.O. Kane, *Band structure of indium antimonide*, J. Phys. Chem. Solids, vol. **1**, pp. 249-261, 1957

6 Conclusions and Future Work

In this thesis a theoretical model for calculating the optical properties of semiconductor quantum well structures in the vicinity of the Γ_6-Γ_8 band gap was presented. The method used for calculating the band-structure of semiconductor quantum wells was the envelope function approximation, based on the theory of Luttinger-Kohn. The numerical method employed for the calculations of the conduction subbands and the heavy hole and light hole valence subbands was the finite difference method. One of the most important predictions obtained from this approximation is the significant valence band mixing for in-plane wave vectors away from the zone centre $\mathbf{k}_{||}=0$. Other important effects analysed by the envelope function approximation were the band-warping and the lifting of the two-fold Kramers degeneracy for the cases where the quantum well structures inversion symmetry is broken.

Expressions for the optical susceptibilities of semiconductor quantum wells were obtained using the density matrix formalism with intraband relaxation taken into account. With the inclusion of the intraband relaxation term, the broadening of the gain spectrum results naturally. Based on this method the linear optical coefficients, the absorption α and the refractive index change Δn, and the second-order nonlinear optical coefficients were estimated. This method is also more convenient for the calculation of the refractive index

change than the one using the Kramers-Krönig relation, since the need for the additional integration over photon energy is eliminated.

Different quantum well structures were investigated, square, disordered and asymmetric two-step wells. For these structures the calculated absorption (or gain) was compared with the conventional method of the parabolic valence band. Notable differences in both spectral shape and peak amplitude were observed. The parabolic band model predicted higher absorption and refractive index change than the valence band mixing model. The study of the effect of changing the carrier density on the absorption showed that by increasing the carrier density the absorption coefficient from negative becomes positive resulting in gain. The effect of an external applied electric field, perpendicular to the quantum well interface, was also considered. By increasing the magnitude of the field a combination of a shift to lower energy regions (red shift) and a reduction of the magnitude of the peak gain (or absorption) was observed.

For the disordered quantum well case the potential profile required for the calculation of the linear optical properties was described by a sum of error functions. This sum was obtained from Fick's law of diffusion, assuming a constant diffusion coefficient D. The error function potential profile was also approximated by a hyperbolic secant potential profile. This approximated profile, when used in the effective mass equation, has the advantage of giving analytic solutions for the energy subbands and wavefunctions. It was found to be valid only for long diffusion times (large Dt) for the calculation of the photoluminescence peak $E_{c1\text{-}hh1}$ and for the calculation of the absorption coefficient close to the absorption edge and invalid for short diffusion times and for the calculation of the refractive index change. The absorption coefficient and the refractive index change of disordered quantum wells when compared with those of the square quantum well, showed a substantial blue shift which makes disordered quantum wells suitable for photonic integrated devices.

An asymmetric two-step GaAlAs quantum well, appropriate for applications that employ the cascading second-order nonlinear effect requiring a $\chi_{zzz}^{(2)}$ (d_{33}) second-order susceptibility tensor was proposed. It was shown that a $\chi_{zzz}^{(2)}$ (d_{33}) second-order susceptibility tensor is possible, based on transitions between the light hole and light hole-like valence band and the conduction band at a wavelength of 1.55μm. The magnitude of the $\chi_{zzz}^{(2)}$ was estimated to be of the same order of magnitude to $\chi_{xzx}^{(2)}$ and that of the bulk GaAs material.

In all the different quantum well structure calculations only interband transitions were considered. The electron-hole Coulomb interaction was neglected and this omission may introduce an inaccuracy at the band edge in certain quantum well cases. Therefore the present formulation illustrates somewhat simplified optical properties without the exciton resonance at the absorption edge. The correct description of optical processes should account for both excitonic and confinement effects [1]. This is a very difficult task, which has not yet been completed since the exact description of excitons in confined structures is complicated. The approaches available to date make a number of simplifications in order to obtain a somewhat realisable model. In these approaches the excitonic effects are considered in the ideal limit of a pure two-dimensional motion of electrons and holes with a 1/r Coulomb interaction [2]-[4]. There is a lot of scope in further researching the problem of exciton effects on the optical properties of quantum wells.

Further improvements in the band structure calculations are possible. A more accurate description for the conduction band valence subbands and dispersion relations may be obtained from the Braun and Rössler model. This model is an expansion of the $\mathbf{k}\cdot\mathbf{p}$ perturbation theory to the fourth order in $\mathbf{k}$. Results that were obtained using this model showed slightly different subband confinement energies when compared with the simple parabolic model [5]. In the calculations presented in this thesis all the bound states were

taken into consideration. Moreover it has to be mentioned that by including a number of the states that extend in the continuum one may obtain a better approximation .

Free-carrier screening may also affect the dispersion relations and the optical properties of a quantum well with an applied electric field resulting in a reduction of the peak gain. This effect may be included in the calculations by solving the effective mass equation simultaneously with the Poisson equation [6].

The comparison of the theoretical calculations for disordered quantum wells with published experimental data showed that the assumption of a constant diffusion coefficient D was inadequate in some of the disordering processes. For these cases an improvement in the calculations may be obtained by substituting the assumption of a constant D with that of a concentration-dependant D(C). For the case of the asymmetric step quantum wells only the resonant terms were taken into account when calculating of the second-order nonlinear susceptibility. The effect of the nonresonant terms may be the subject of further research work in order to estimate the significance of this approximation.

References

[1] D.-P. Xue, *Current contribution to electroabsorption of zinc-blende semiconductor quantum wells*, Appl. Phys. Lett., vol. **64**, pp. 963-965, 1994

[2] S. Schmitt-Rink, D.S. Chemla and D.A.B. Miller, *Linear and nonlinear optical properties of semiconductor quantum wells*, Advances in Physics, vol. **38**, pp. 89-188, 1989

[3] C.-H. Lin, J.M. Meese, Y.-C. Chang, *Optical properties of GaAs/$Al_xGa_{1-x}As$ multiple quantum wells versus electric field including exciton transition broadening effects in optical modulators*, J. Appl. Phys., vol. **75**, pp. 2618-2627, 1994

[4] E.H. Li, B.L. Weiss, K.S. Chan and J. Micallef, *Polarisation dependent refractive index of an interdiffusion induced AlGaAs/GaAs quantum well*, Appl. Phys. Lett., vol. **62**, pp. 550-552, 1993

[5] A.T. Meney, *Theory of the optical properties of III-V semiconductor quantum wells*, PhD Thesis, 1992

[6] D. Ahn and S.L. Chuang, *Model of the field-effect quantum well laser with free-carrier screening and valence band mixing*, J. Appl. Phys., vol. **64**, pp. 6143-6149, 1988

Appendix A

Density matrix formulation for 2nd-order nonlinear susceptibilities

Equation (3.11a) for the second-order density operator $\rho^{(2)}$ is reduced to,

$$i\hbar\frac{d\rho_{ab}^{(2)}(t)}{dt} = (E_a - E_b)\rho_{ab}^{(2)} - i\hbar\gamma_{ab}\rho_{ab}^{(2)} - \sum_c\left\{E_j^\beta(t)M_{ac}^\beta\rho_{cb}^{(1)} - \rho_{ac}^{(1)}M_{cb}^\beta E_j^\beta(t)\right\} \tag{A.1}$$

This equation can be solved by removing the rapid time variation, expressing the second-order density operator $\rho^{(2)}$ as a sum of different terms proportional to $\exp[\pm i(\omega_1\pm\omega_2)]$, similarly to equation (3.16),

$$\rho^{(2)} = \tilde{\rho}(\omega_1+\omega_2)e^{-i(\omega_i+\omega_2)t} + \tilde{\rho}(\omega_1-\omega_2)e^{-i(\omega_i-\omega_2)t} + \\ +\tilde{\rho}^{(2)}(-\omega_1+\omega_2)e^{-i(-\omega_i+\omega_2)t} + \tilde{\rho}^{(2)}(-\omega_1-\omega_2)e^{i(\omega_i+\omega_2)t} \tag{A.2}$$

By replacing $\rho^{(2)}$ from (A.2) and $\rho^{(1)}$ from (3.19) into (A.1) we obtain the following equation,

$$\hbar(\omega_1+\omega_2)\tilde{\rho}^{(2)}_{ab}(\omega_1+\omega_2) = (E_a - E_b)\tilde{\rho}^{(2)}_{ab}(\omega_1+\omega_2) - i\hbar\gamma_{ab}\tilde{\rho}^{(2)}_{ab}(\omega_1+\omega_2) -$$
$$-\sum_c \left\{ \frac{M^{\beta}_{ac}(\rho^{(0)}_{bb}-\rho^{(0)}_{cc})M^{\alpha}_{cb}\tilde{E}^{\alpha}_i\tilde{E}^{\beta}_j}{\{\hbar\omega_{cb}-\hbar\omega_1-i\hbar\gamma_{cb}\}} - \frac{M^{\beta}_{cb}(\rho^{(0)}_{cc}-\rho^{(0)}_{aa})M^{\alpha}_{ac}\tilde{E}^{\alpha}_i\tilde{E}^{\beta}_{j_i}}{\{\hbar\omega_{ac}-\hbar\omega_2-i\hbar\gamma_{ac}\}} \right\}$$

(A.3)

which can be solved for $\tilde{\rho}^{(2)}_{ab}$,

$$\tilde{\rho}^{(2)}_{ab}(\omega_1+\omega_2) = \sum_c \left\{ \frac{M^{\beta}_{ac}(\rho^{(0)}_{bb}-\rho^{(0)}_{cc})M^{\alpha}_{cb}\tilde{E}^{\alpha}_i\tilde{E}^{\beta}_j}{\{\hbar\omega_{ba}-\hbar(\omega_1+\omega_2)-i\hbar\gamma_{ab}\}\{\hbar\omega_{cb}-\hbar\omega_1-i\hbar\gamma_{cb}\}} \right.$$
$$\left. - \frac{M^{\alpha}_{ac}(\rho^{(0)}_{cc}-\rho^{(0)}_{aa})M^{\beta}_{cb}\tilde{E}^{\alpha}_i\tilde{E}^{\beta}_j}{\{\hbar\omega_{ba}-\hbar(\omega_1+\omega_2)-i\hbar\gamma_{ab}\}\{\hbar\omega_{ac}-\hbar\omega_2-i\hbar\gamma_{ac}\}} \right\}$$

(A.4)

Appendix B

Dipole operators

The optical dipole operator for the transition between two states i and j, is given by the expression (3.46),

$$\langle \psi_i | e\mathbf{r} | \psi_j \rangle = e \int_V [\phi_i(\mathbf{r}) u_{i0}(\mathbf{r})]^* \mathbf{r}\, \phi_j(\mathbf{r})\, u_{j0}(\mathbf{r}) dV \tag{B.1}$$

This expression can be simplified assuming that the envelope functions ϕ_i and ϕ_j are slowly varying compared with the cell periodic functions u_{i0} and u_{j0} [1]. The matrix element can be written approximately as,

$$\begin{aligned}
\langle \psi_a | e\mathbf{r} | \psi_j \rangle \approx e \frac{1}{V} \Bigg\{ & \int_V \phi_i^*(\mathbf{r})\, \phi_j(\mathbf{r})\, dV \int_V u_{i0}^*(\mathbf{r})\, \mathbf{r}\, u_{j0}(\mathbf{r})\, dV + \\
& + \int_V \phi_i^*(\mathbf{r})\, \mathbf{r}\, \phi_j(\mathbf{r})\, dV \int_V u_{i0}^*(\mathbf{r})\, u_{j0}(\mathbf{r})\, dV \Bigg\} = \\
= e \langle u_{i0} | \mathbf{r} | u_{j0} \rangle & \int_V \phi_i^*(\mathbf{r})\, \phi_j(\mathbf{r})\, dV + e\delta_{ij} \int_V \phi_i^*(\mathbf{r})\, \mathbf{r}\, \phi_j(\mathbf{r})\, dV = \\
= e \langle u_{i0} | \mathbf{r} | u_{j0} \rangle & \langle \phi_i^* | \phi_j \rangle + e\delta_{ij} \langle \phi_i^* | \mathbf{r} | \phi_j \rangle
\end{aligned} \tag{B.2}$$

where $\langle u_{i0} | \mathbf{r} | u_{j0} \rangle$ is equal to,

$$\langle u_{i0}|\mathbf{r}|u_{j0}\rangle = \frac{1}{V}\int_{V} u_{i0}^{*}(\mathbf{r})\,\mathbf{r}\,u_{j0}(\mathbf{r})\,dV = \frac{1}{V_0}\int_{V_0} u_{i0}^{*}(\mathbf{r})\,\mathbf{r}\,u_{j0}(\mathbf{r})\,dV$$

(B.3)

V_0 is the volume of an elementary cell. δ_{ij} is equal to,

$$\delta_{ij} = \frac{1}{V}\int_{V} u_{i0}^{*}(\mathbf{r})\,u_{j0}(\mathbf{r})\,dV = \frac{1}{V_0}\int_{V_0} u_{i0}^{*}(\mathbf{r})\,u_{j0}(\mathbf{r})\,dV$$

(B.4)

The allowed optical transitions can be split into two categories, the *intraband* and the *interband* transitions. Because of selection rules expression (B.2) can be reduced to a simpler form, depending on the type of the transition. For the two different cases the dipole moment matrix element can be approximated by the following expressions;

(i) For intraband transitions the first term of expression (B.2) is equal to 0 [2]-[3] and so,

$$\langle \psi_i|e\mathbf{r}|\psi_j\rangle \approx e\delta_{ij}\langle \phi_i^{*}|\mathbf{r}|\phi_j\rangle = \delta_{\mathbf{k}',\mathbf{k}}\int_{-\infty}^{+\infty}\phi_i^{*}(z)\,z\,\phi_j\,dz$$

(B.5)

(ii) For interband transitions the second term of expression (B.2) is equal to 0, so

$$\langle \psi_i|e\mathbf{r}|\psi_j\rangle \approx e\langle u_{i0}|\mathbf{r}|u_{j0}\rangle\langle \phi_i^{*}|\phi_j\rangle$$

(B.6)

where,

$$\langle \phi_i^{*}|\phi_j\rangle = \frac{1}{S}\int d^2r_{\|}\,\exp\left[i(\mathbf{k}_{\|}' - \mathbf{k}_{\|})\cdot\mathbf{r}_{\|}\right]\int_{-\infty}^{+\infty}\phi_i^{*}(z)\,\phi_j(z)\,dz$$

(B.7)

For $\mathbf{k}_{\|}=\mathbf{k}_{\|}'$, (B.7) can be simplified to,

$$\left\langle \phi_i^* \middle| \phi_j \right\rangle = \int_{-\infty}^{+\infty} \phi_i^*(z)\, \phi_j \, dz \tag{B.8}$$

References

[1] G. Bastard,*Wave mechanics applied to semiconductor heterostructures*, (Lés Édition de Physique, Halsted Press, 1988), Chapter 2, pp.54-56

[2] D.D. Coon and R.P.G. Karunasiri, *New mode of IR detection using quantum wells*, Appl. Phys. Lett., vol. **45**, pp. 649-651, 1984

[3] E.J. Roan and S.L. Chuang, *Linear and nonlinear electroabsorption in a modulation doped quantum well*, J. Appl. Phys., vol. **69**, pp.3249-3260, 1991

Appendix C

Analytic solution for the hyperbolic secant potential profile

The effective mass equation (2.28) has an analytic solution when the potential profile V(z) is the hyperbolic secant potential profile given in expression (4.6). This can be obtained by transforming (2.28) into,

$$\frac{\partial^2}{\partial w^2}\phi_n(w) + Q\,\mathrm{sech}^2(\beta z)\phi_n(w) = \lambda_n\phi_n(w) \tag{C.1}$$

where $w=\beta z$, $Q = \frac{2m^* V_0}{\hbar^2\beta^2}$ and $\lambda_n = \frac{2m^* E_n}{\hbar^2\beta^2}$. Equation (C.1) can be further transformed by setting $\zeta = \frac{1}{2}(1+\tanh w)$, $\lambda_n=-K^2$ and $\phi_n=\cosh^{-K} w\, F(\zeta)$,

$$\zeta(\zeta-1)\frac{d^2F}{d\zeta^2} + (K+1)(2\zeta-1)\frac{dF}{d\zeta} + [K(K+1)-Q]F = 0 \tag{C.2}$$

This equation has as solution the hypergeometric functions $F(K+\frac{1}{2}+P, K+\frac{1}{2}-P|K+1|\zeta)$ where $P = \sqrt{Q+\frac{1}{4}}$. This function becomes infinite at $\zeta=1$, unless $K_n = \sqrt{Q+\frac{1}{4}} - \frac{1}{2} - n$, where n can be zero or any positive integer less than $\sqrt{Q+\frac{1}{4}} - \frac{1}{2}$. Therefore the envelope function is equal to,

$$\phi_n = \cosh^{-K_n} w \, F(K_n + \tfrac{1}{2} + P, K_n + \tfrac{1}{2} - P \,|\, K_n + 1 \,|\, \zeta)$$

(C.3)

The discrete eigenvalue λ_n is equal to,

$$\lambda_n = -\left[(n + \tfrac{1}{2}) - \sqrt{Q + \tfrac{1}{4}}\right]^2, \quad n = 0,1,\ldots,n < \sqrt{Q + \tfrac{1}{4}} - \tfrac{1}{2}$$

(C.4)

Publications

C. Kelaidis, J.M. Arnold

Comparison of impurity induced disordering potential profiles

IEE Electronics Division Colloquim in 'Applications of quantum well technologies'

London, England, 5 March 1993

C. Kelaidis, D.C. Hutchings, J.M. Arnold

Assymmetric two-step GaAlAs quantum well for cascaded second-order processes

Conference on Lasers and Electro-optics (CLEO)

Amsterdam, The Netherlands, 28 August - 2 September 1994

C. Kelaidis, D.C. Hutchings, J.M. Arnold

Assymmetric two-step GaAlAs quantum well for cascaded second-order processes

to be published in IEEE Journal of Quantum Electronics